Dissertation

submitted to the

Combined Faculties of the Natural Sciences and Mathematics

of the Ruperto-Carola-University of Heidelberg, Germany

for the degree of

Doctor of Natural Sciences

Put forward by

Oleksiy, Kovtun

born in: Kharkiv (Ukraine)

Oral examination: December 16th 2015

Precision gamma-ray polarimetry applied to studies of bremsstrahlung produced by polarized electrons

Referees: Priv.-Doz. Dr. Stanislav Tashenov

Prof. Dr. Norbert Herrmann

Zusammenfassung

In der vorliegenden Arbeit wurde die lineare Polarisation der Bremsstrahlung untersucht, die in Stößen von transversal und longitudinal polarisierten Elektronen mit Goldatomen entsteht. Das Experiment wurde am Mainzer Microtron MAMI im Institut für Kernphysik der Johannes Gutenberg-Universität Mainz durchgeführt. Spinpolarisierte Elektronen mit einer kinetischen Energie von 2.15 MeV kollidierten mit einem dnnen Goldtarget und produzierten Bremsstrahlung. Die lineare Polarisation der emittierten Photonen wurde mithilfe der Compton-Polarimetrie, angewandt auf einen segmentierten HP-Germanium-Detektor, gemessen. Experimentelle Ergebnisse zeigen eine starke Korrelation zwischen der Elektron-Spin-Orientierung und der linearen Polarisation der Bremsstrahlung. Dies deutet auf eine dominante Rolle des Elektronenspins in Elektron-Kern-Bremsstrahlung und Coulomb-Streuung.

Abstract

The thesis reports on the measurement of bremsstrahlung linear polarization produced in collisions of longitudinally and transversely polarized electrons with gold atoms. The experiment was performed at the Mainzer Microtron MAMI in the Institut für Kernphysik of Johannes Gutenberg-Universität Mainz, Germany. Spin-oriented electrons with 2.15 MeV kinetic energy collided with a thin golden target and produced bremsstrahlung. Linear polarization of the emitted photons was measured by means of Compton polarimetry applied to a segmented high-purity germanium detector. Experimental results reveal a strong correlation between the electron spin orientation and bremsstrahlung linear polarization. This indicates a dominant role of the electron spin in atomic-field bremsstrahlung and Coulomb scattering.

Contents

Chapter 1

Introduction

Atomic-field bremsstrahlung, which is the emission of a photon during the electron scattering on a nucleus, is a dominant process in relativistic electron-atom collisions. For the first time it was observed by Röntgen in 1895 when he discovered x rays and the bremsstrahlung spectrum was first interpreted by Sommerfeld back in 1913 [1]. Over the last hundred years bremsstrahlung has been actively studied both theoretically and experimentally. Its cross section, angular distribution and polarization were measured. Bremsstrahlung is an important tool in many areas of experimental research, as astrophysics [2] and plasma physics [3, 4] and many technical fields. It is commonly used as a source of radiation for the industrial and medical purposes. Apart from the interest in the process itself, there is a number of reasons why bremsstrahlung plays an important role in modern physics. Of particular interest is a hard-photon end of the bremsstrahlung spectrum. Here, the decelerating electron transfers all of its kinetic energy to the emitted photon. This part of the spectrum is known as the short wavelength limit, as the photon energy $E = \hbar\omega = hc/\lambda$ is maximum. At the tip of the spectrum bremsstrahlung can be considered as a time-reversal of photoeffect [5, 6], and additionally is closely related to the process of radiative recombination of a continuum electron into an unoccupied bound state [7, 8]. Therefore studies of bremsstrahlung also help to better understand these fundamental physical processes. Fig. 1.1 shows

the similarity between the upper-mentioned processes.

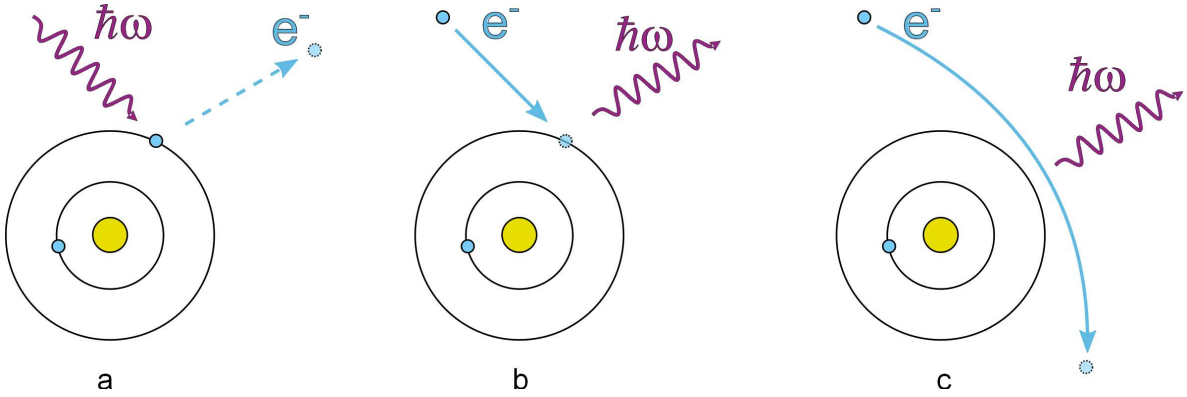

Figure 1.1: Correlation between photoeffect (a), radiative recombination (b) and bremsstrahlung in Coulomb scattering (c).

Bremsstrahlung arises due to the decelerated motion of the electron in the Coulomb field of the atomic nucleus. Emitted x rays contain important information about the dynamics of an electron scattering. Of particular interest is the photon linear polarization, as it is defined by the scattering plane, i.e., by the electron acceleration direction [9]. Moreover it was already predicted in 1960s that the polarization of bremsstrahlung is affected by the initial electron spin orientation [10, 11]. Hence, accurate studies of polarization of photons emitted in electron-atom collisions should lead to better understanding of the electron motion in the strong Coulomb field of the nucleus.

The influence of the spin on the electron scattering dynamics becomes quite significant at relativistic energies. It occurs due to the extremely strong fields experienced by the electron. In particular, the magnetic field induced by the upcoming nucleus in the electron rest frame becomes strong enough to interact with the electron spin. The spin-orbit interaction results in Mott scattering asymmetry when the electrons are polarized perpendicularly to the scattering plane [12, 13]. Analogous to the Mott scattering, the left-right asymmetry in bremsstrahlung emitted by transversely polarized electrons was studied theoretically [14, 15] and observed experimentally [16, 17]. However, experi-

mental investigations of the influence of spin-orbit interaction on the bremsstrahlung polarization have been performed only recently.

Theoretical calculations of polarization correlations between incident electron and the emitted photon were performed by Tseng and Pratt already in 1970s [18, 19]. The experimental studies were stalled for a long time due to the complexity and high requirements to the measurement resolution. Due to the recent progress in manufacturing the novel positional and energy sensitive solid state detectors the effective studies of photon linear polarization become possible. Within last 8 years two bremsstrahlung experiments with 100 keV electrons have been performed [20, 21]. Moreover, for the first time both photon and electron polarization were controlled at the same time. These measurements unambiguously indicated the rotation of bremsstrahlung linear polarization as a result of the spin-orbit interaction. In this work we extended the upper-mentioned experimental studies and measured the linear polarization of bremsstrahlung emitted by 2 MeV electrons. At higher electron energies this effect is predicted to decrease [22, 23]. Therefore our experiment indicates an important benchmark for bremsstrahlung theories providing the measurement of polarization correlation in the energy range where it reaches its maximum.

Theoretical approach of Tseng and Pratt, which is based on the relativistic partial-wave representation of the electron motion in a static (screened) potential of a target atom, requires high computational resources. With the increase of electron energy large number of partial waves have to be utilized in order to achieve convergence. So far such calculations have been extended up to 2 MeV by Yerokhin and Surzhykov [24]. For higher energies D. Jakubassa-Amundsen presented the series of calculations within the Sommerfeld-Maue approximation [22]. Private communication with the upper-mentioned authors indicated that none of the theories was able to give reliable predictions for the electron energies between 2 and 5 MeV.

This work concentrates on two major tasks. First: experimental study of the corre-

lation between the electron spin orientation and the bremsstrahlung linear polarization for the x-ray energies of about 2 MeV and testing the relativistic partial-wave predictions at their energy limit. Second: description of the Compton polarimetry technique applied to the positional sensitive segmented germanium detector as well as the presentation of the novel method of background suppression by means of Compton imaging.

The thesis is organized in a following way. Chapter 2 contains the introduction into the x-ray polarimetry including the information about the main ways of interaction of photons with matter, required for understanding the principles of operation of solid state detectors. In this chapter we characterize different types of x-ray detectors and techniques allowing to increase the measurement resolution. In Chapter 3 theoretical and experimental studies of electron - nucleus (or ordinary) bremsstrahlung are discussed in detail along with a brief information about other types of bremsstrahlung. There we define all the necessary terms for the further discussion of our experimental work. In Chapter 4 we present our measurement of the bremsstrahlung polarization correlations and describe the facility where the experiment was performed. In Chapter 5 the detailed description of the data analysis is presented including the novel algorithm of the background suppression by means of Compton imaging. Chapter 6 contains the obtained results, their interpretation and comparison with the theory and in Chapter 7 we give a summary of the performed work.

Chapter 2

X-Ray and γ-Ray polarimetry

In this chapter we overview the experimental investigation of the photon polarization. We will consider and compare different types of γ-ray detectors and discuss the techniques of Compton imaging and the pulse shape analysis which allow to significantly improve the polarimetry precision.

Depending on the initial photon energy different techniques are applied for polarization studies. For the low-energy regime from around 1 to 10 keV Bragg-, Thomson-, or Rayleigh scattering can be used [25–27]. The latter is efficient up to $\sim$100 keV. For hard x rays from 10 keV up to several MeV Compton polarimetry is employed. We will consider this technique in more details since we used it in our experiment. Investigations of photon polarization in the energy range of GeV require polarimeters based on the pair production process [28].

2.1 Interaction of x rays with matter

A photon passing through matter doesn't loose its energy continuously. The energy depositions occur in discrete interaction points. Unlike charged particles, electrically neutral photons are not affected by Coulomb fields of electron's nuclei. Depending on its energy the photon can interact with matter through the following processes:

1. Photoelectric absorption
2. Compton scattering
3. Rayleigh scattering
4. Pair production.

Fig. 2.1 shows the cross sections of the upper-mentioned processes as a function of the photon energy in the case of germanium atoms. Within the interval between 100 keV and up to several MeV Compton scattering and photoabsorption are dominant. This is a typical energy range for Compton polarimetry. We will discuss this technique in details in Section 2.8.

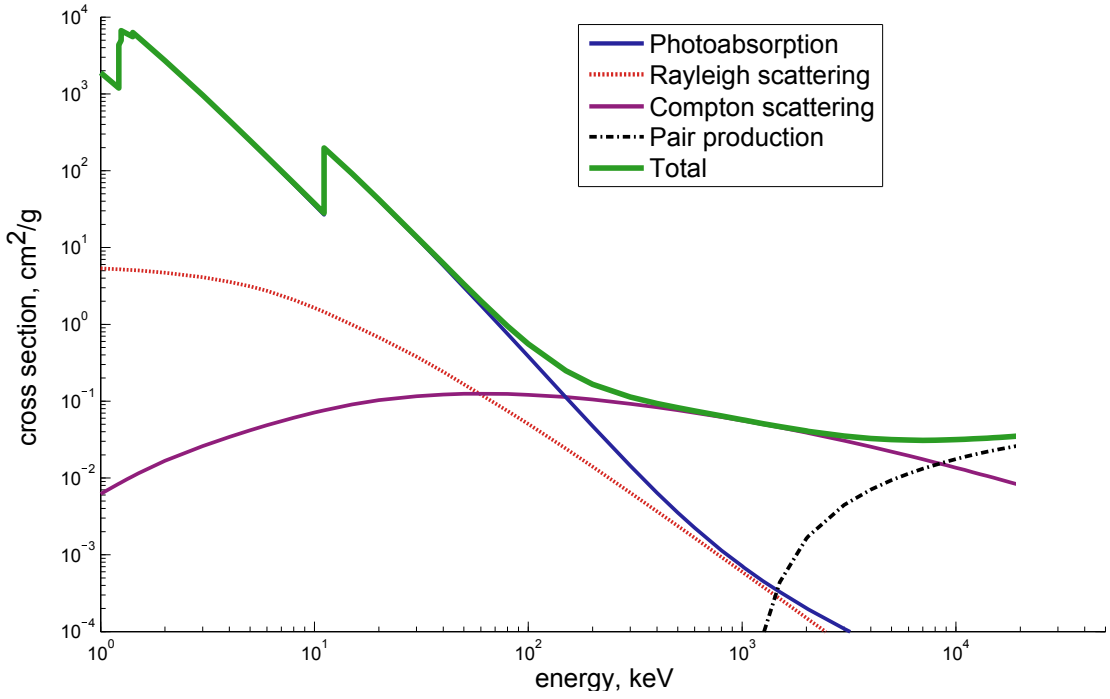

Figure 2.1: Different ways of photon-matter interaction. Data taken for germanium atoms [29].

2.1.1 Photoelectric absorption

A photon may get fully absorbed by an atom. In this case the excited electron is ejected from its bound shell. The kinetic energy of the emitted electron is given by:

$$E = \hbar\omega - E_{bind}, \tag{2.1}$$

where $\hbar\omega$ is the photon energy and E_{bind} is the binding energy of the electron. Significant increases in the photoabsorbtion cross section (see Fig. 2.1) correspond to binding energies of different atomic shells. As the photon energy exceeds a binding energy of a certain shell, more electrons become accessible.

The cross section of the phototoelectric absorption is given by:

$$\sigma \sim Z^n/(\hbar\omega)^{\frac{7}{2}}, \tag{2.2}$$

where Z is the atomic number and exponent n varies between 3 and 5 over the γ-ray energy region. High dependence on Z explains the usage of heavy materials (for example lead, Z = 82) for x-rays shielding.

2.1.2 Compton and Rayleigh scattering

An inelastic scattering of a photon on a free or quasi-free electron is called Compton scattering. Unlike the photoelectric absorption, here a photon transfers only part of its energy to an electron and retains a certain momentum after the interaction. The geometry of Compton scattering is shown in Fig. 2.2. Due to the momentum and parity conservations the trajectories of the incoming and scattered photons as well as the propagation direction of the recoiled electron lie within one plane.

The process of Compton scattering is described by the following expression combining the initial and the scattered photon energies $\hbar\omega$ and $\hbar\omega'$:

$$\hbar\omega' = \frac{\hbar\omega}{1 + \hbar\omega/mc^2(1 - \cos\theta)}, \tag{2.3}$$

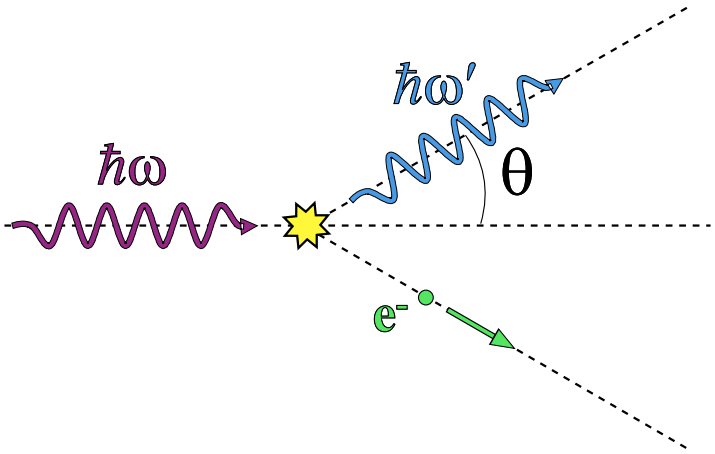

Figure 2.2: Schematic of Compton scattering. $\hbar\omega$ and $\hbar\omega'$ are the energies of the photon before and after the collision respectively. e^- denotes the recoiled electron. θ is the photon scattering angle.

The energy of the outgoing photon is defined by the scattering angle θ. The recoiled electron obtains the energy $E_e = \hbar\omega - \hbar\omega'$. Inserting this expression in Eq. 2.3 we get a dependence of the electron recoil energy on the scattering angle:

$$E_e = \frac{\frac{(\hbar\omega)^2}{mc^2}(1-\cos\theta)}{1+\frac{\hbar\omega}{mc^2}(1-\cos\theta)}. \tag{2.4}$$

We assume that the initial electron kinetic energy is zero. In reality electrons are bound to atoms, so that the "free electron" approximation is valid only when the energy of the incoming photon is much higher than the electron binding energy.

The angular dependence of energy loss of a 2 MeV photon is shown in Fig. 2.3. The energy of the scattered photon is larger than the energy of the recoil electron only at forward angles. The energy E_e transferred to the electron increases together with the scattering angle θ and reaches its maximum at $\theta = 180°$.

At the low energy limit, when $\hbar\omega << mc^2$, the energy transferred to a recoil electron decreases and Compton scattering reduces to Thomson scattering. The cross section of Thomson scattering doesn't depend on the photon energy and frequency and is defined

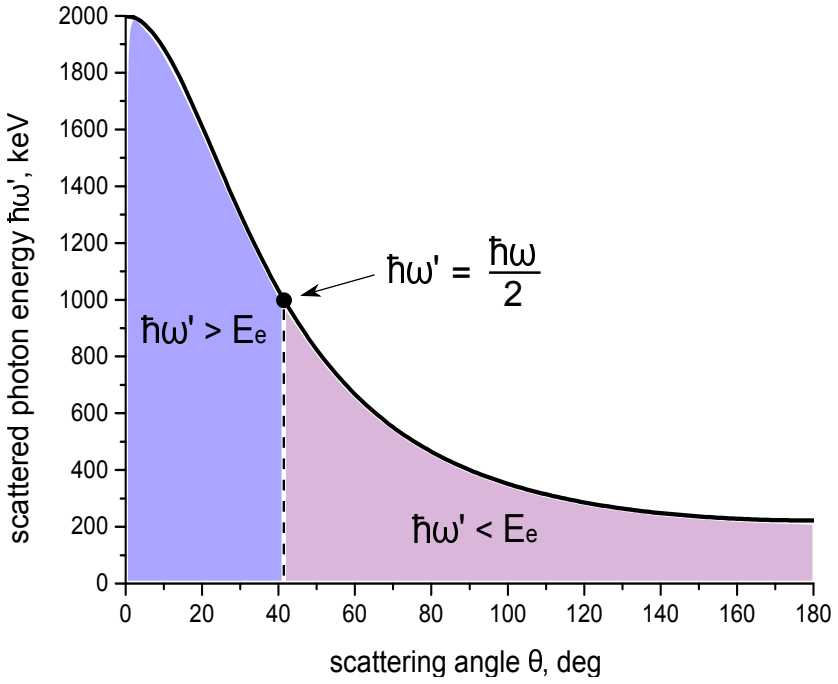

Figure 2.3: The energy of the outgoing photon $\hbar\omega$ as a function of the scattering angle θ. At $\theta > 42°$ the photon transfers most of its energy to the recoil electron.

by:

$$\sigma = \frac{8\pi}{3} r_e^2 = 6.652 \times 10^{-25} cm^2, \tag{2.5}$$

where $r_e = \frac{e^2}{m_e c^2} = 2.8 \times 10^{-13} cm$ is the classical electron radius, i.e., the radius of a hollow sphere which surface contains uniformly distributed electron charge e and whose electrostatic energy is equivalent to the electron rest energy.

Compton scattering is sensitive to the linear polarization of the incoming x rays. Photons scatter predominantly perpendicular to the polarization plane forming a dipole-like distribution, as shown in Fig. 2.4 [30].

The differential cross section of Compton scattering, which includes photon polarization and explains the angular distribution shown in Fig. 2.4, is given by the

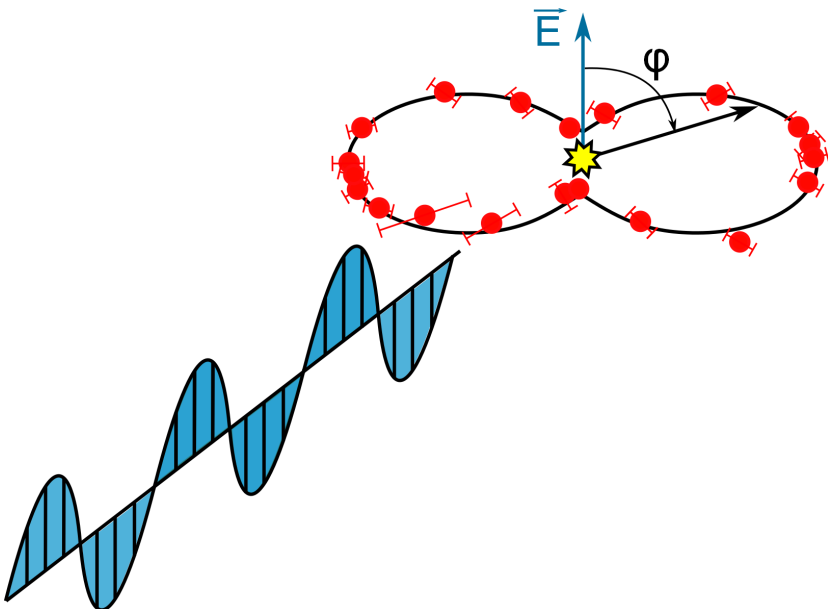

Figure 2.4: Angular distribution of Compton scattered photons with initial vertical polarization $\vec{E}$. φ is the azimuthal scattering angle.

Klein-Nishina formula [9, 31, 32]:

$$\frac{d\sigma}{d\Omega} = \frac{r_0^2}{2}\frac{\hbar\omega'^2}{\hbar\omega^2}\left(\frac{\hbar\omega'}{\hbar\omega} + \frac{\hbar\omega}{\hbar\omega'} - 2\sin^2\theta\cos^2\varphi\right), \tag{2.6}$$

where $d\Omega$ is a solid angle element, θ is the polar scattering angle as in Fig. 2.2 and φ is the azimuthal scattering angle (see Fig. 2.4). The sensitivity of Compton scattering to photon polarization is exploited in the Compton polarimetry technique. By measuring the angular distribution of scattered photons one can study the polarization properties of the photon beam. In germanium Compton scattering dominates in the energy interval between 100 keV and 10 MeV. Due to this fact germanium detectors are ideal for hard x-ray polarimetry as they provide excellent position and energy resolution required for polarization studies.

Photon scattering on the electron which then remains bound is called Rayleigh scattering. Unlike Thomson scattering it depends on the atomic number of the target, the

incoming photon energy and takes into account interaction between multiple electrons. Coherent contribution from many bound electrons significantly increases the Rayleigh scattering cross section. The energy deposition for Rayleigh scattering can be estimated by replacing m_e in Eq. 2.4 with a mass of an atom. For a 60 keV photon scattering at 180° in lead we get $E_e \sim 37$ meV. The negligible energy deposition during scattering is exploited in the newly developed technique of Rayleigh polarimetry [27]. Photons get scattered in a lead foil and their angular distribution is measured with a position sensitive detector.

2.1.3 Pair production

Pair production is the creation of an electron and a positron as a result of interaction of a photon with a nucleus (pair production in the field of an electron is also possible but far less likely). The photon must have enough energy to create the mass of the electron and the positron, therefore the energy threshold for pair production is $E_{min} = 2m_e c^2 = 1022$ keV. The kinetic energy of two particles will then be the difference between the initial photon energy and the energy required to create the pair:

$$E_{e^+} + E_{e^-} = \hbar\omega - 2m_e c^2. \tag{2.7}$$

The produced positron annihilates with an electron in the target material in the vicinity of the initial interaction an produces two 511 keV photons. In germanium pair production dominates at energies higher than 10 MeV (see Fig. 2.1).

2.1.4 Photon attenuation

When a photon beam traverses matter, part of it gets deflected or absorbed. However, some photons pass through without any interaction. The number of passed photons depends on several factors as the density and thickness of the material, the intensity of the photon beam as well as its initial energy.

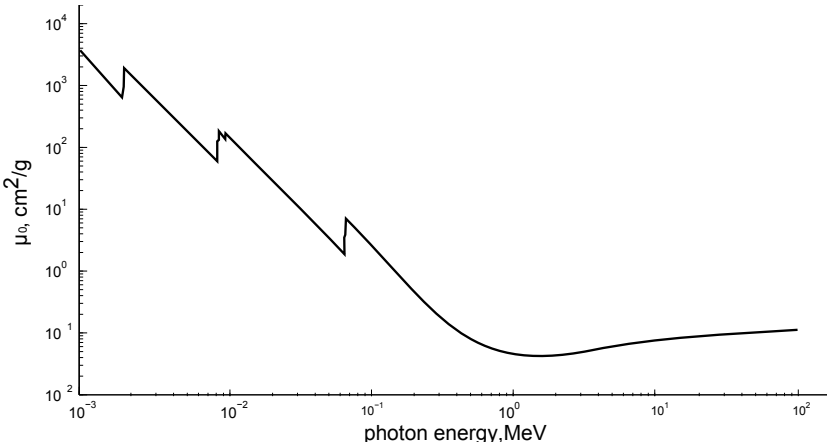

Figure 2.5: Dependence of the mass attenuation coefficient μ_0 on photon energy in lead, Z = 82. [33]

The attenuation of photon beam of initial intensity I_0 by a layer of material with density ρ is given by:

$$\frac{I}{I_0} = e^{-\mu_0 \rho x}, \tag{2.8}$$

where I is the intensity of the outgoing beam, μ_0 is the mass attenuation coefficient and x is the material thickness. The values of μ_0 are now calculated in the wide range of photon energies for different elements and published in the form of tables [33]. In Fig. 2.5 the stopping power of lead is shown as a function of photon energy.

2.2 Scintillators

In a scintillator detector, a charged particle or a γ ray is converted into optical photons. When combined to an amplifying device such as a photomultiplier or an avalanche photo diode, these photons can be converted into electronic signals. Generally scintillators can be divided into organic and inorganic. The most common organic scintillators are trans-stilbene ($C_{14}H_{12}$), naphthalene ($C_{10}H_8$) and plastic polystyrene. They have the extremely short time response of the order of a few nanoseconds. Due to this

reason they are typically used for a fast detection of charged particles. On the other hand organic scintillators are characterized by a relatively low energy resolution. The inorganic scintillators are usually the alkali halide crystals with some activator impurity, for example NaI(Tl) and CsI(Tl). Due to a better energy resolution than organic scintillators these detectors can be used for a γ-ray spectroscopy. Among the non-alkali materials are lutetium orthosilicate (LSO) and bismuth germanate (BGO). The time resolution of inorganic scintillators is generally 2-3 orders of magnitude lower than of organic ones ($\sim$ 500 ns). The exception is CsF and BaF_2 with decay times of $\sim$ 5 ns and $\sim$ 500 ps respectively. However, their use is limited by lower energy resolution.

2.3 Principles of operation of semiconductor detectors

In a pure intrinsic (undoped) semiconductor the electron density n and hole density p are equal. Typically in a room temperature in a 1 cm $\times$ 1 cm $\times$ 300 μm germanium plate there are $\sim 3 \times 10^{15}$ free charge carriers. A 10 keV photon generates only 3.4×10^3 e-h pairs, which would be impossible to resolve. Therefore, in order to obtain a signal, the amount of free charges has to be reduced, i.e., detector has to be depleted. All present-day germanium detectors are based on a semiconductor junctions (see Fig. 2.6). Combining p- and n-type semiconductors causes the drift of electrons from n- to p-region, while holes drift from p- to n-region. As a consequence, extra electrons fill up holes in p-part and in n-region electrons get recombined by diffused holes. This processes alter the initial charge distribution in the zone around the interface between two materials and both p- and n-regions obtain different potentials. This creates the electric field which gets stronger as more electrons and holes get recombined in different parts of the junction. As the electric field increases a region with no free charges is formed. This region is known as the depletion zone. It is radiation sensitive. A photon

passing through the depletion zone liberates electrons and holes, which are then swept by the electric field towards the p- or n-region. Placing an electric contact on the either side of the pn-junction allows to measure the induced charges, which are proportional to the energy deposited by the photon.

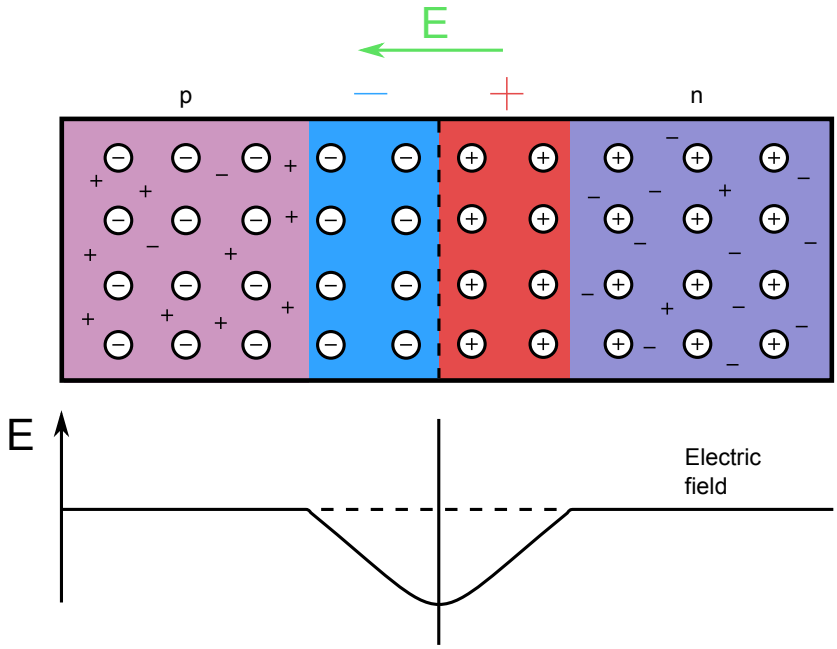

Figure 2.6: Schematic of an pn-junction. The intrinsic electric field is the strongest around the interface between p- and n-type materials.

In general, depletion zone is rather thin and the intrinsic electric field is not strong enough to provide the effective charge collection. The depletion zone of a pn-junction can be extended by applying the external reversed bias voltage, i.e., negative voltage to the p-side. The external electric field also provides a better charge mobility and thus increases the time and energy resolution of the detector [34, 35].

Compared to scintillators germanium detectors provide much better combination of energy and time resolution in the energy interval between a few keV and $\sim$ 10 MeV. Fig. 2.7 compares the spectra of ^{60}Co measured with NaI and High Purity Germanium (HPGe) detectors.

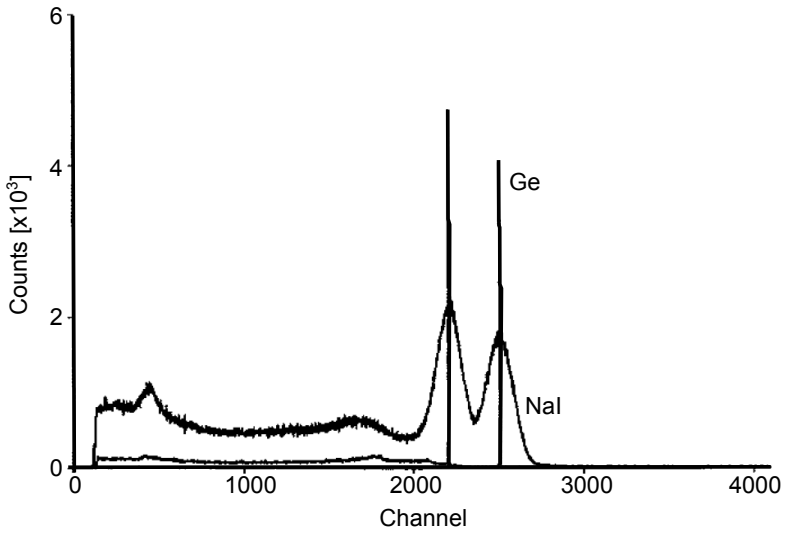

Figure 2.7: ^{60}Co spectra taken with HPGe and NaI detectors [36].

The significant difference in energy resolution is clearly visible. Moreover, due to higher photoabsorption cross section germanium detectors have greater peak-to-Compton ratio.

2.4 Silicon detectors

Silicon detectors have a slightly worser energy resolution as compared to germanium (see Fig. 2.8). One of the reasons is the higher energy required for a pair creation (3.62 eV against 2.98 eV in germanium). Additionally currently it is technically impossible to obtain a high purity silicon. Impurities generate leakage current that increases the detector's noise. However, Si detectors have one big advantage - they don't have to be operated at LN_2 temperatures (except from the old lithium-drifted silicon diodes, Si(Li), that have to be kept at cryogenic temperature in order to maintain the lithium-drifted compensation). The combination of a good energy resolution, ability to operate at room temperatures and relatively low prices make Si detectors one of the most widely

used not only in physics experiments but also in medicine.

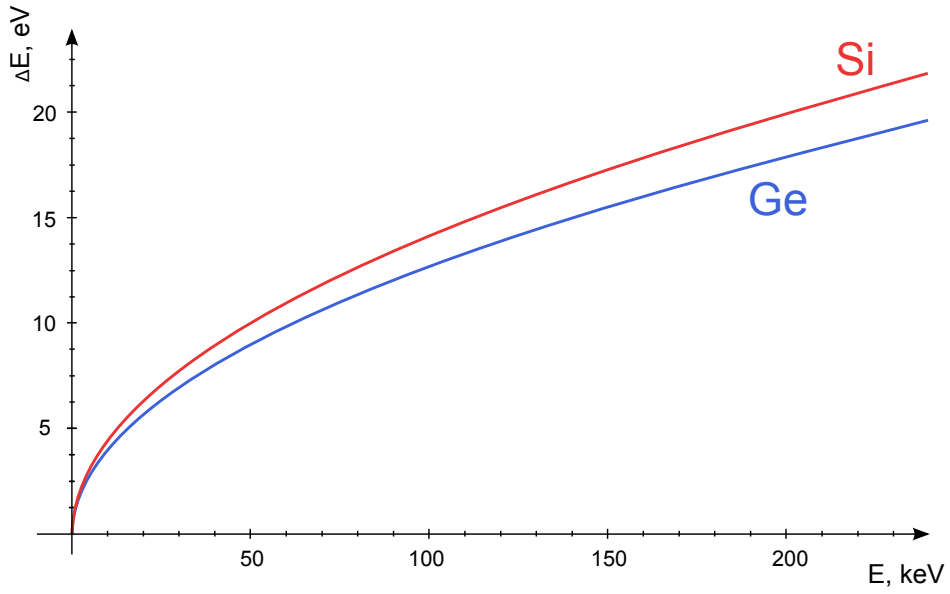

Figure 2.8: Energy resolution of Si and Ge detectors based on statistics of charge carriers.

2.4.1 Silicon diode detectors

Silicon diode detectors, or PIN diodes, are composed of three differently doped layers of silicon (see Fig. 2.9). Compared to a pn-junction, a PIN diode has a thicker depletion zone, which allows for a more efficient collection of photons and lowers the capacitance. Thus a PIN diode provides a better signal-to-noise ratio and a higher detection energy bandwidth. Most of the photons are absorbed in the intrinsic region. The generated electrons and holes are separated by the electric field and drift towards the corresponding electrodes.

The voltage V_d necessary to fully deplete the diode with depth d and resistivity ρ can be estimated with the following equation [37]:

$$V_d = 4 \left[\frac{\Omega \ cm}{(\mu m)^2} \right] \frac{d^2}{\rho} - 0.5V \tag{2.9}$$

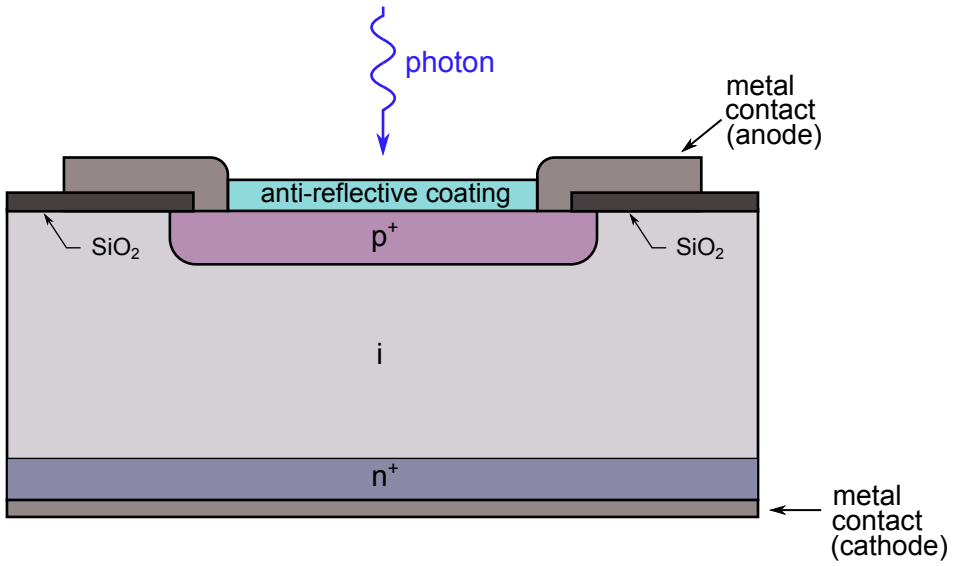

Figure 2.9: A schematic of a PIN diode. An anode has a geometry of a ring and is shown in cross section. SiO_2 layer is used for electric insulation of anode from intrinsic material.

The usual working voltage for the PIN diodes is in the order of 50 - 80 V. Higher voltages can lead to a breakdown and destroy the detector.

2.4.2 Double sided silicon strip detectors

Similarly to their germanium analogues, silicon detectors can also be made positional sensitive. Planar detectors are most commonly segmented into strips either from one or both sides. In Fig. 2.10a the geometry of a double sided silicon strip detector (DSSSD) is shown. Opposite electrodes are divided into system of strips providing x and y coordinates of the interaction. Since the incoming photon generates equal numbers of electrons and holes, the signals on both sides of the detector should be identical while the pulse height varies for different energies. In case of multiple detection this helps correlating the measured x and y coordinates.

Positive charges present in SiO_2 attract electrons from Si layer. Those electrons accumulate under the Si-SiO_2 surface and cannot be removed due to the bias voltage.

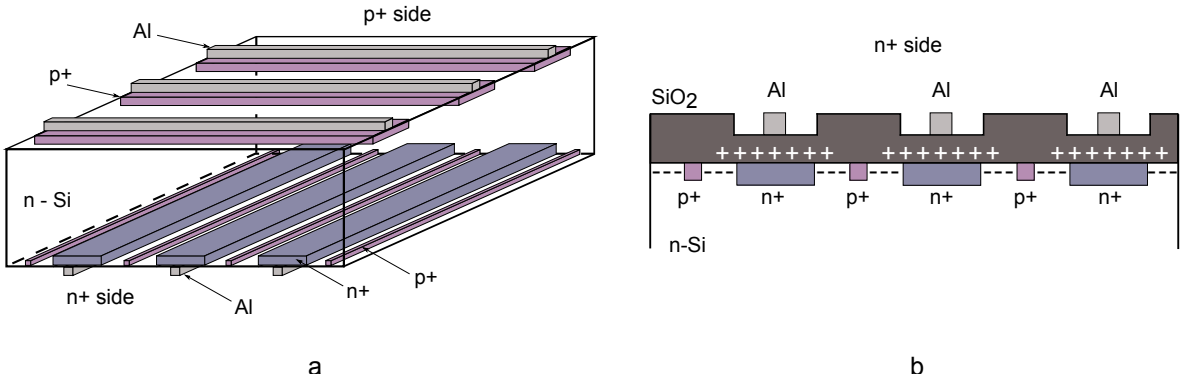

Figure 2.10: Design of a DSSSD. Every strip is equipped with an Al contact. On the n^+ side (b) n^+ strips are separated by p^+ strips to avoid the attraction of electrons from n-layer by a positive space charge. The SiO_2 insulating layer is shown only at the right part of the figure.

To avoid the short circuit, n^+ stripes are electrically separated by blocking p^+ stripes (see Fig. 2.10b).

2.5 Germanium detectors

HPGe detector can be produced both from the n- and p-type germanium with a net impurity concentration of $\sim 10^{10}$ atoms/cm^{-3}. The electric contacts of a detector are made by boron implantation on one side and by lithium drift on the other side. Depending on a conducting type the bulk crystal forms the pn-junction either with the Li-drifted (p-type) or with the boron implanted (n-type) contact.

Germanium detectors can have planar (electric contacts are placed symmetrically on the opposite sides of the crystal) and coaxial (normally cylindrical crystal with one contact on the outer surface and second contact on the cylinder's axis) geometry. In a coaxial detector due to its geometry the electric field is stronger around the inner contact. In such detectors the depletion starts from the outer contact. Therefore, in a p-type germanium the outer contact has to be lithium-drifted and in a n-type it should be boron-implanted. Since the thick Li-drifted contact provides a certain x-ray

shielding, n-type coaxial detectors are preferred for low energies. In a planar detector contacts are symmetric and the electric field is more homogeneous. Therefore, planar detectors are usually produced from a p-type germanium, since it is technically easier to obtain.

Due to the low band gap germanium detectors have to be operated at cryogenic temperatures in order to reduce the thermal creation of e-h pairs. Generation of the free charge carriers within the depleted zone increases the noise and reduces the energy resolution. Normally germanium detectors are placed in vacuum chamber which is attached to a LN_2 dewar (T = 77 K).

In past HPGe detectors could not be produced. Therefore lithium drifted germanium detectors were exploited. In order to preserve the necessary lithium concentration such detectors had to be constantly kept at cryogenic temperatures. The detailed description of Ge(Li) detectors can be found in Ref. [38, 39]. We will not discuss them here as the Ge(Li) detectors are now out of date and get replaced by HPGe detectors.

2.5.1 Segmented germanium detectors and γ-ray arrays

Detectors with segmented electric contacts can provide information about the location of the x-ray interaction points. For this, each segment should be equipped with an individual preamplifier that converts the collected charge into voltage. Type of segmentation depends on a detector's geometry (see Fig. 2.11). The positional resolution is limited only by the geometrical size of the segments and can reach a few tens of μm [40]. Normally such detectors provide only 2D positional sensitivity. The interaction depth can be obtained from the charge drift times or by applying the pulse shape analysis (PSA) that has been actively developed for the different detector types in the last decade. Both energy and position resolving detectors open new possibilities in high precision γ-ray spectroscopy. For example in experiments where photons are emitted from the fast ion beams, segmented detectors allow for improved determination

of the emission angle with respect to the ion beam an thus Doppler correction of photon energies can be performed event by event.

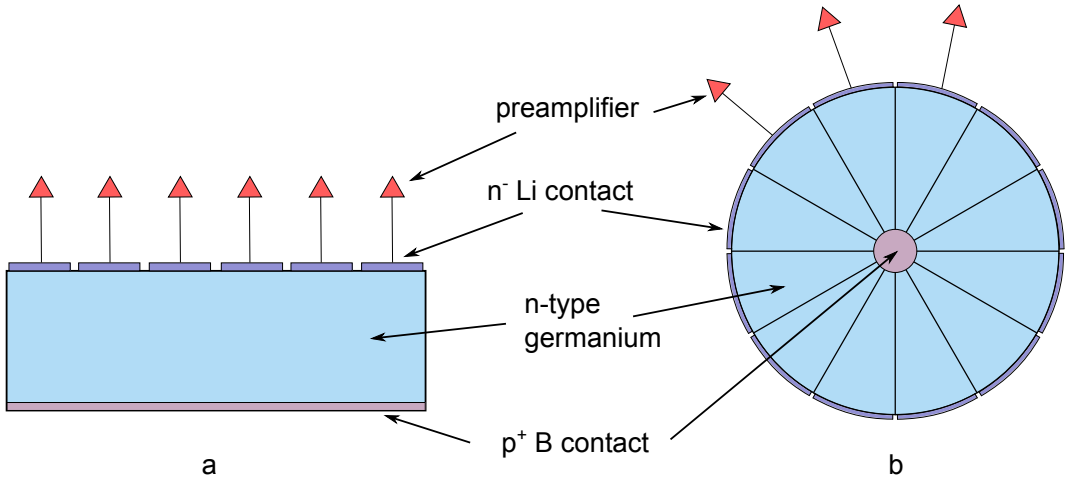

Figure 2.11: Schematic of planar (a) and coaxial (b) segmented detectors.

In order to obtain a larger space coverage, single germanium detectors can be combined into arrays. Nowadays a number of such γ-ray spectrometers is used for nuclear physics experiments. MINIBALL at CERN [41] and TIGRESS at TRIUMPH [42] contain 24 and 12 highly segmented coaxial HPGe detectors respectively. Despite the large size of the germanium crystals, these arrays provide relatively poor peak-to-total ratio, since large number of photons escape before being fully absorbed. In order to resolve and filter out such events and thus to suppress the Compton background, germanium detectors are surrounded by a BGO scintillators that detect the escaped photons. Although the BGO shield significantly improves the peak-to-total ratio, it also covers a large solid angle and thus reduces the total efficiency of the detector array. This limitation can be overcome by removing the scintillator shielding and exploiting a larger number of closely-packed germanium detectors instead. In this case the photon that escapes one detector has a probability to get absorbed in another one. Several novel 4π detector arrays are currently being constructed: AGATA [43] and DESPEC [44] in

Europe and GRETA [45] in the USA. Schematic design of AGATA array is shown in Fig. 2.12. It contains 180 hexagons formed by highly segmented coaxial HPGe detectors.

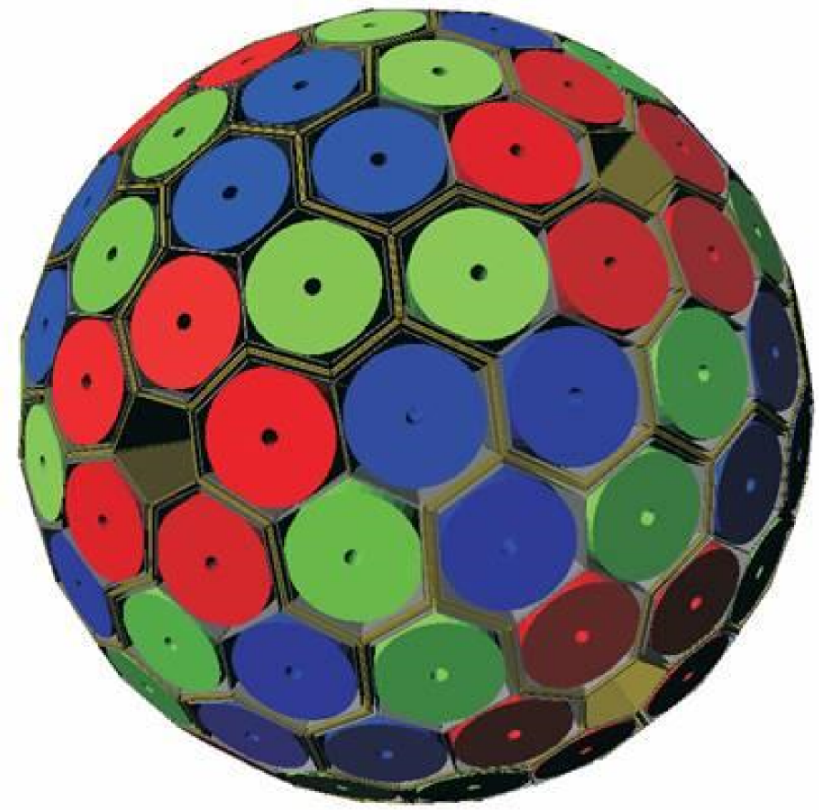

Figure 2.12: Geometry of AGATA. Empty pentagons can be used to deliver the beam inside the array.

Due to the close-packing detector geometry the efficiency for the photon full absorption is considerably higher than in last generation γ-ray spectrometers, as a large fraction of photons that Compton scatter between the detectors eventually deposit all of their energy in the detector's active volume. At high rates γ-ray tracking algorithm is applied to distinguish between the events where two photons hit the adjacent segments and where the single photon scattered from one segment to another. Pulse shape analysis is used to determine the 3D coordinates of interaction within the single seg-

ment, which makes the tracking much more efficient. We will consider PSA and γ-ray tracking in more details in the next sections of this chapter.

2.6 Pulse shape analysis

Position resolution of segmented detectors is determined by the granularity. The past few decades have established the increasing demand of high positional sensitivity. In principal this can be achieved by increasing the number of segments which is rather complicated technically and therefore boosts the detector's price. As an alternative at the beginning of $2000s$ the concept of pulse shape analysis (PSA) has been introduced. It allowed to determine the location of the photon interaction with about ten times higher precision that is given by the physical segmentation of a detector [46].

When entering the detector an ionizing particle induces a cloud of electrons and holes. Under the influence of the bias electric field they drift towards the detector's electrodes. The motion of charge carriers induces a so-called net charge signal in the segment where the interaction took place and transient signals in the neighboring segments. The combination of these pulses gives an unique indication of the interaction location. The closer the segment to the energy deposition point the higher is the amplitude of the transient signal. Moreover, the shape and the polarity of the transient pulse vary with the depth of interaction. The dependence of the charge collection and transient pulses on lateral and depth position of interaction is presented in Fig. 2.13.

Within our experiment we applied PSA based on the matrix method, developed by A.Khaplanov [48]. Signals from all the 25 detector pixels were combined into one vector $\vec{S}$, which is then decomposed into the linear combination of basis pulses for a set of grid points throughout the detector. A database of basis pulses is a set of simulated detector's responses to a point-like energy depositions, generated on a 2 mm grid, yielding 250 samples per segment. If $\overline{x_i}$ is the energy deposited to a certain grid point i and $\overline{m_i}$ is the corresponding basis signal, the experimental vector $\vec{S}$ can be

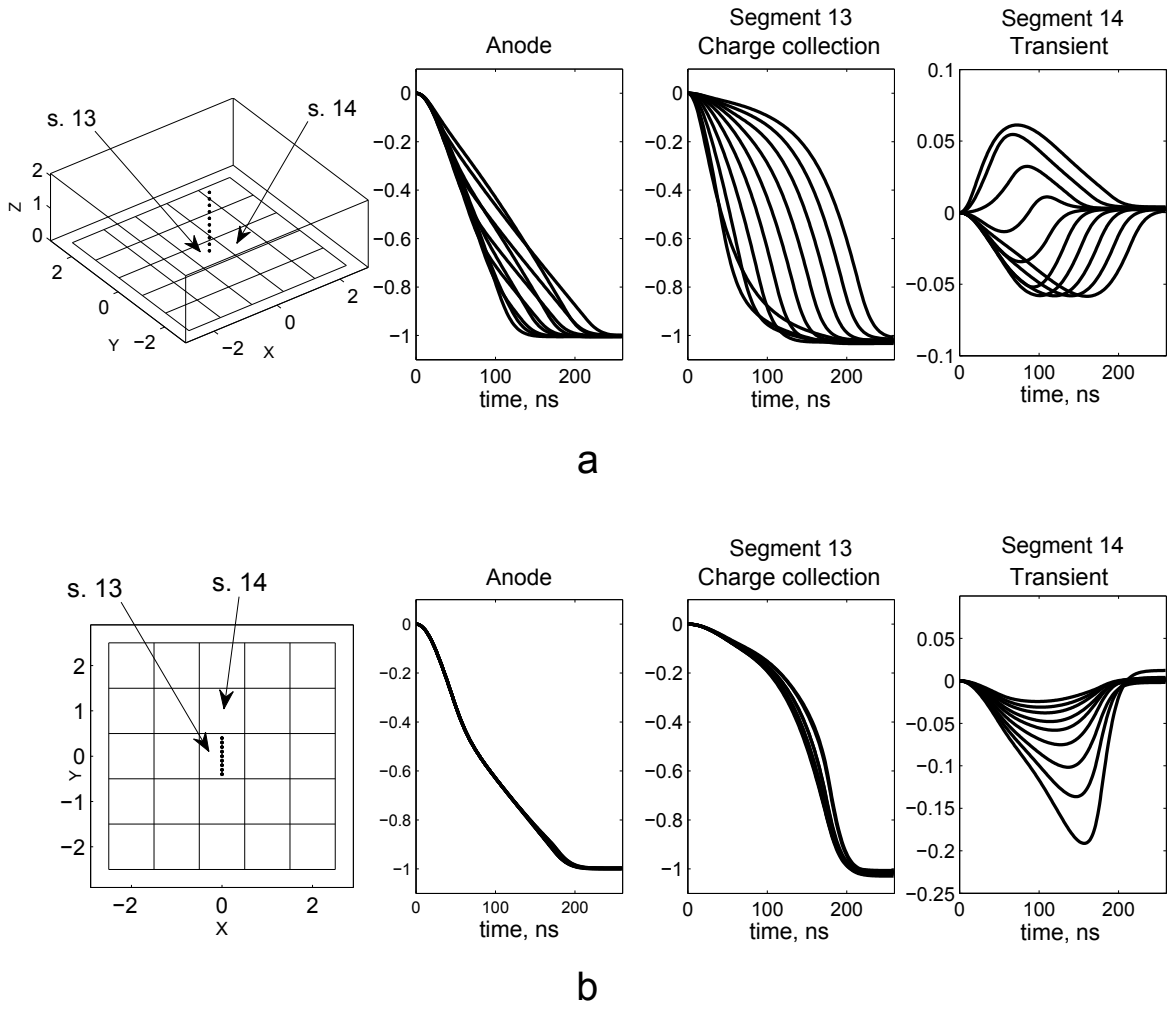

Figure 2.13: Charge signals as a function of depth (a) and lateral position (b) of interaction [47]. (a) - the faster rising signals in segment 13 and the positive transient pulses in segment 14 correspond to interaction points closer to the positive segmented contact. (b) - the transient signals with larger amplitude in correspond to the interactions closer to segment 14.

written as:

$$\vec{S} = \overline{m_1} x_1 + \overline{m_2} x_2 + ... + \overline{m_n} x_n = M\overline{x}. \tag{2.10}$$

where vector $\overline{x}$ consists of energy depositions to every grid point and M is the matrix containing all the basis signals.

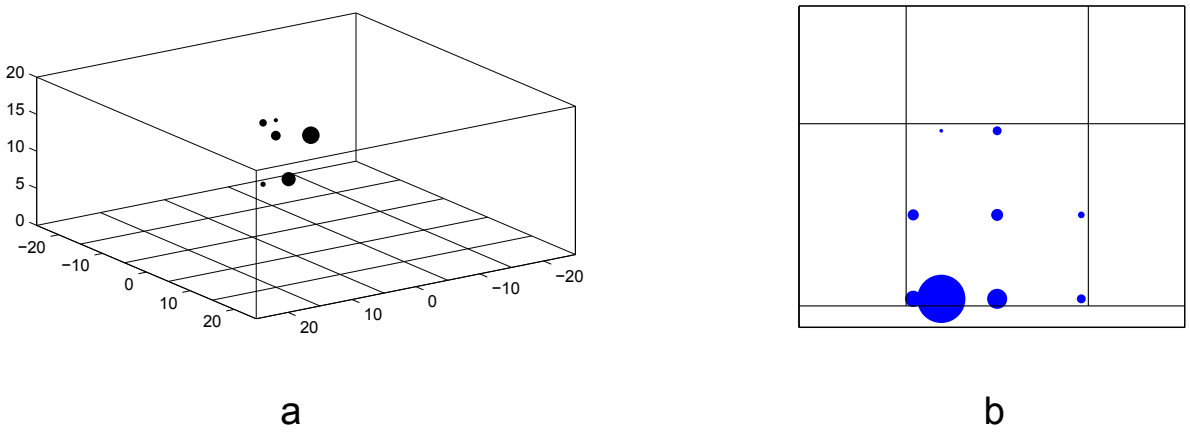

Figure 2.14: Typical result of the fitting 2.10 displayed in detectors volume (a) and in 2D projection (b). Number of the grid points corresponding to a point-like interaction is generally spread over the pixel [47].

Solving Eq. 2.10 yields the number of the grid points with the non-zero energy depositions (see. Fig 2.14). The interaction location is then determined as their superposition considering the deposited energy of the point as its statistical weight.

2.7 Compton imaging

The technique of Compton imaging allows to visualize the source of the detected radiation. It is mostly applied in γ-ray astronomy [49] but in recent years has also been used in laboratory physics experiments.

The concept of Compton imaging is based on the correlation between the energy the electron receives in a Compton scattering to an angle between the incoming and outgoing photon directions (see Eq. 2.4). In Fig. 2.15 the algorithm of Compton imaging is presented. The possible incoming photon directions are limited to the surface of a cone, built on the line connecting two points of interactions E_e and $\hbar\omega'$. The cone angle θ is the polar Compton scattering angle obtained with Eq. 2.3. The cones built for each registered event are projected onto a sphere enclosing the detector. The projections

intersect and form an image.

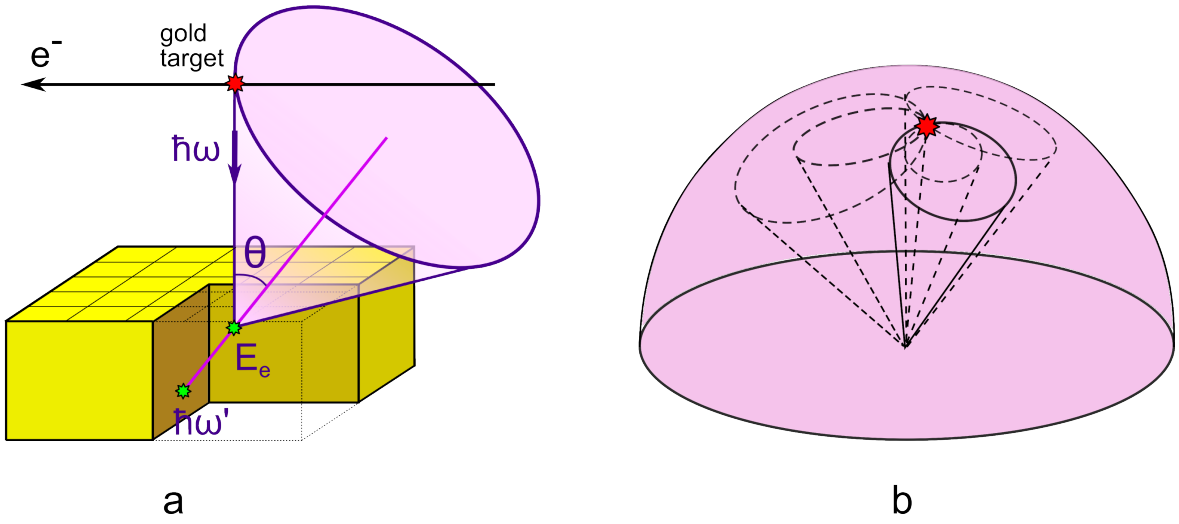

Figure 2.15: The algorithm of Compton imaging. (a) The line between energy depositions $\hbar\omega'$ and E_e defines the cone axis. The angle θ is derived from the Compton scattering formula (2.3). (b) Intersection of the cone projections onto a hemisphere represent the source of the detected x rays.

In Fig. 2.16 a number of cone projections is presented [47]. Note that this figure illustrates only a half of the sphere, therefore several projections are not visible completely. This is caused by the fact that photons scatter predominantly perpendicular to their initial direction and a most of the reconstructed cons are thus very wide and intersect with the complete sphere.

The situation shown in Fig. 2.16 is only achievable in case of the ideal detector. In a real experiment due to the limited position and energy resolutions, there is an uncertainty in determination of the cone axis and the photon scattering angle. When the points of interactions are close together, the cone axis is more sensitive to the position uncertainty which increases the error in determining the x ray source. The dependence of the angular resolution on the distance between the interactions was demonstrated in [50].

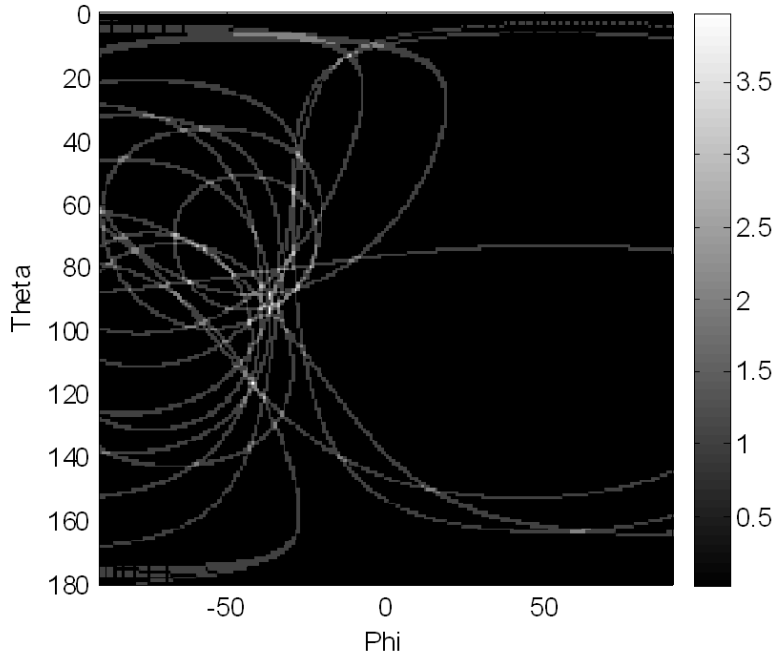

Figure 2.16: Formation of a Compton image by the projections of the reconstructed cons onto a hemisphere. Here a hemisphere is mapped onto a square similarly to a geographical world map [47].

2.8 Compton polarimetry

The principles of Compton polarimetry have been introduced in the middle of the last century [51]. The method is based on the sensitivity of Compton scattering to polarization of incoming photons. Linearly polarized scattered photons form a dipole distribution (see Fig. 2.17), which is described by the Klein-Nishina formula (Eq. 2.6). From fitting the measured angular distribution of scattered photons with the Klein-Nishina equation the polarization properties of the incoming photon beam can be extracted. The anisotropy and the tilt angle of the angular distribution contain information about the degree of polarization P the orientation of polarization vector (see Fig. 2.17). The Stokes parameters P_1 and P_2, described in Section 3.1.3, can be measured by means of Compton polarimetry.

Experimentally Compton polarimetry can be realized in a number of ways [52]. In

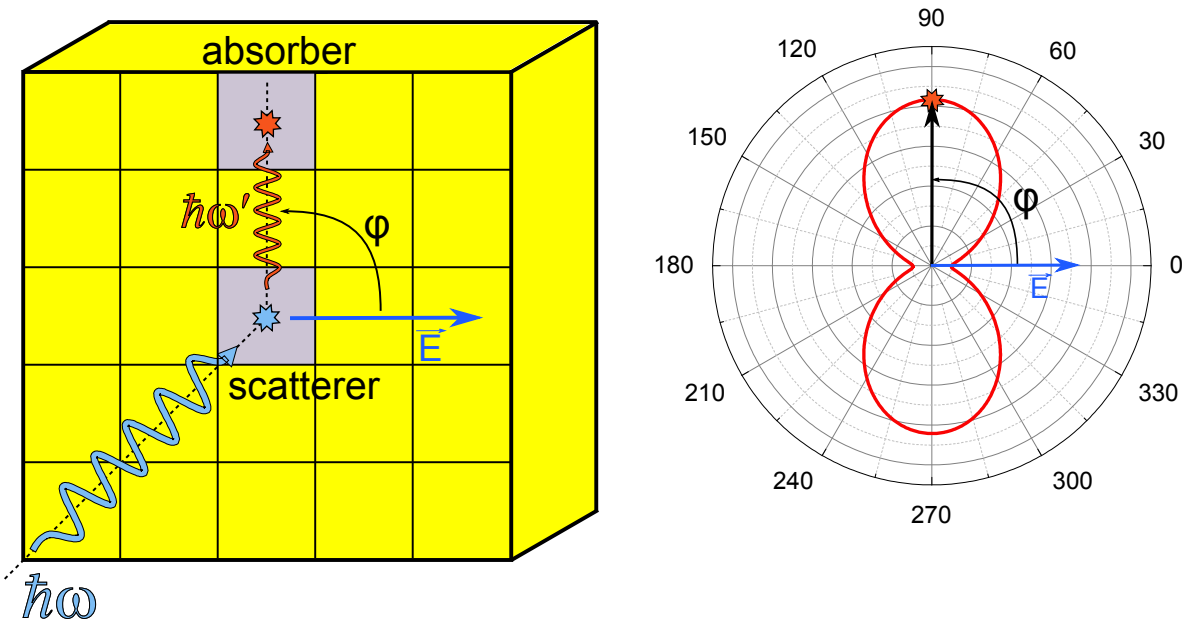

Figure 2.17: Scheme of Compton polarimetry. Modulated distribution of scattered photons contains information about the initial polarization of the photon beam.

the present work we used the method with an active scatterer, i.e., photons scattered and got absorbed within same detector, as shown in Fig. 2.17. Energies of both the recoiled electron and the scattered x ray are measured simultaneously. Alternatively, a piece of material (for example a metal plate) can serve as a passive scatterer and the detector system behind it measures the Klein-Nishina distribution [20]. The conventional method uses two or more detectors, one as a scatterer and others as absorbers, that detect scattered photons. This method allows for an optimization of polarimeter, i.e., by varying the size and material of single detectors one can significantly improve the polarimeter's performance. As was already mentioned, at low energies a Si detector has a larger Compton scattering efficiency relative to photoabsorption, while for a Ge detector the picture is opposite. Therefore, the polarimeter construction, where Si detector is used as a scatterer and a system of Ge detectors measure the scattered photons, is one of the best solutions [53]. Since the information about the initial photon

polarization is lost after the second scattering, the detector system used for Compton Polarimetry should be optimized to detect single Compton events.

The sensitivity of Compton scattering to the polarization of x rays of a certain energy is characterized by a so-called modulation factor M. It is given by the difference in number of photons that were scattered parallel and perpendicularly to the initial polarization vector:

$$M(\theta) = \frac{I_{(90°)} - I_{(0°)}}{I_{(90°)} + I_{(0°)}} = \frac{\sigma_\perp - \sigma_\parallel}{\sigma_\perp + \sigma_\parallel} \tag{2.11}$$

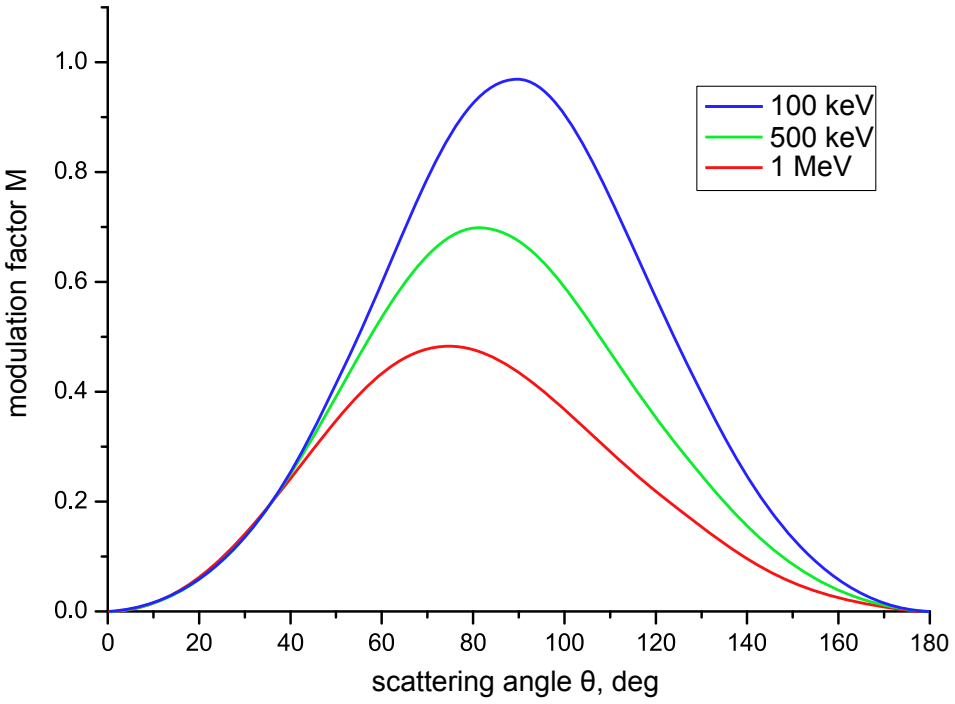

Figure 2.18: Dependence of modulation factor on the polar Compton angle θ for different photon energies.

The dependence of the modulation factor on the photon energy and the polar scattering angle is shown in Fig. 2.18. For 100 keV it reaches maximum at $\sim$90°. For higher photon energies the maximum M moves slightly in the direction of forward scattering angles. In order to improve the efficiency of a polarization measurement, scattered

photons have to be detected at the polar angles that correspond to the maximum of modulation factor.

Chapter 3

Electron - nucleus bremsstrahlung

3.1 Theoretical description

Theoretical description of bremsstrahlung was continuously developed throughout the 20th century along the advancements in experiments.

In earlier studies various semi-classical approaches [1] were utilized that were soon replaced by the quantum-mechanical treatment [54, 55]. By 1970s the full-order relativistic treatment of bremsstrahlung was developed that included linear polarizations of both the incoming electron and the outgoing x ray [18, 19, 56]. While such a theory, based on the Dirac equation, is very accurate, it is computationally extensive. At higher energies large numbers of partial waves need to be taken into account to achieve the convergence. Because of that, in the first calculations reliable results could be obtained in the energy range below 600 keV. This limit was increased to only about 2 MeV at present [24, 57]. At energies higher than that, bremsstrahlung is still treated using approximate theoretical approaches such as the one of Sommerfeld-Maue [22, 23]. However, this approach fails at energies lower than about 5 MeV. So, there appears to be a gap at $2-5$ MeV where bremsstrahlung cannot be at present reliably described. No unifying theory was developed so far.

3.1.1 Cross section

The bremsstrahlung cross section represents the probability of an incoming electron transiting from one to another continuum state with a simultaneous emission of a photon. The classical theory of bremsstrahlung predicts the photon emission in every case of electron interacting with nucleus and changing its velocity. In reality most of the electron-nucleus collisions are elastic, and the probability of the photon emission is about 137 times smaller than the probability of the elastic scattering: $\sigma_{bremsstr} = \alpha\sigma_{elastic}$, ($\alpha \approx 1/137$ is a fine structure constant) [58].

For a single photon in a cubic volume with the side L, bremsstrahlung cross section is given by the transition probability per atom per electron divided by the velocity of the incident electron [55]:

$$d\sigma = \frac{\omega}{(p_0 c/E_0)} \left(\frac{\hbar}{m_0 c}\right)^3 L^3, \tag{3.1}$$

where

$$\omega = (2\pi/\hbar)\rho_f |H_{if}|^2. \tag{3.2}$$

Here ρ_f is the density of the final states and the term H_{if} is the matrix element describing the transformation of the system from an initial to a final state (before and after the emission of a bremsstrahlung photon). The term $|H_{if}|^2$ can be written as:

$$|H_{if}|^2 = \left(\frac{2\pi}{k}\frac{e^2}{\hbar c}\right)(m_0 c^2)^2 \left| \int \psi_f^* (\boldsymbol{u}_\lambda^* \boldsymbol{\alpha}) e^{-i\boldsymbol{kr}} \psi_i \mathrm{d}\tau \right|^2 L^{-9}, \tag{3.3}$$

where $\boldsymbol{u}_\lambda$ is the unit polarization vector of a photon, $\boldsymbol{\alpha}$ is the vector of Dirac matrices, and ψ_i and ψ_f are the Dirac functions describing electron at the initial and final state respectively. The angular and energy differential cross section $d\sigma$ can be

expressed as [55]:

$$d\sigma = \frac{137 r_0^2}{(2\pi)^4} \frac{p_f E_i E_f}{p_i} \left| \int \psi_f^*(\boldsymbol{u}_\lambda^* \boldsymbol{\alpha}) e^{-i\boldsymbol{kr}} \psi_i d\tau \right|^2 k\, dk\, d\Omega_k\, d\Omega_{p_f}. \tag{3.4}$$

In Eq. 3.4 $r_0 = (\hbar/mc)\alpha$ is the classical electron radius, p_i and p_f are the initial and the final electron momenta, E_i and E_f are the initial and final electron energies, $\boldsymbol{k}$ is the momentum of the emitted photon and $d\Omega_k$ and $d\Omega_{p_f}$ are the elements of solid angle in the direction of $\boldsymbol{p_f}$ and $\boldsymbol{k}$ respectively. A number of approximate wave functions have been utilized to obtain the final expression for the bremsstrahlung cross section. Bethe-Heitler formula calculated by the first order Born approximation with free-particle wave functions has a relatively simple form and is applicable for both non-relativistic and relativistic energies. Below we will consider it in more details.

The process of bremsstrahlung consists of two parts: the interaction of an electron with the radiation field causing the emission of a photon and interaction of an electron with the electric field of the nucleus. First can be treated with the help of the perturbation theory, while the interaction with the Coulomb field can be handled precisely. This requires a solution of the Dirac equation for an electron of energy E_i that moves in the Coulomb field [58]:

$$(-i\vec{\alpha} \cdot \nabla + \beta - E_i - \frac{\alpha Z}{r})\psi(\boldsymbol{r}) = 0, \tag{3.5}$$

where $\frac{\alpha Z}{r}$ is a potential term. In order to solve the Eq. 3.5 the wave function $\psi(\boldsymbol{r})$ is represented as a slightly deformed plane wave:

$$\psi(\boldsymbol{r}) = \psi_0(\boldsymbol{r}) + \alpha Z \psi_1(\boldsymbol{r}) + (\alpha Z)^2 \psi_2(\boldsymbol{r}) + ... \tag{3.6}$$

$\psi_0(\boldsymbol{r})$ describes the incoming plane wave and the following terms characterize the minor distortion caused by the interaction with the nuclear potential. Solving the Eq. 3.5 with the first-order approximation the triple-differential cross section describing

the energy and angular distribution of bremsstrahlung is obtained [58, 59]:

$$\begin{aligned}\frac{d^3\sigma}{dk\,d\Omega_k\,d\Omega_{p_f}} = \frac{\alpha Z^2 r_0^2}{4\pi^2}\frac{p_f}{k p_i q^4}\Bigg(& (4E_f^2 - q^2)\frac{p_i^2\,\sin^2\theta_i}{(E_i - p_i\,\cos\theta_i)^2} + \\ & + (4E_i^2 - q^2)\frac{p_f^2\,\sin^2\theta_f}{(E_f - p_f\,\cos\theta_f)^2} - \\ & - (4E_iE_f - q^2 + 2k^2)\frac{2p_ip_f\,\sin\theta_i\,\sin\theta_f\,\cos\varphi}{(E_i - p_i\,\cos\theta_i)(E_f - p_f\,\cos\theta_f)} + \\ & + 2k^2\frac{p_i^2\,\sin^2\theta_i + p_f^2\,\sin^2\theta_f}{(E_i - p_i\,\cos\theta_i)(E_f - p_f\,\cos\theta_f)}\Bigg),\end{aligned} \tag{3.7}$$

where q is the momentum transferred to the nucleus and is given by $\boldsymbol{q} = \boldsymbol{p_i} - \boldsymbol{p_f} - \boldsymbol{k}$. In Eq. 3.7 system of polar coordinates is used with the Z axis in the direction of the emitted photon $\boldsymbol{k}$ and where incoming electron moves in the X-Z plane. Therefore θ_i and θ_f are the angles between the photon momentum and the incoming and outgoing electron directions respectively.

Bethe-Heitler formula only gives correct results if the condition

$$\frac{\alpha Z}{\beta} \ll 1 \tag{3.8}$$

is fulfilled both for incoming and outgoing electrons. It means that the Born approximation becomes less reliable with decreasing of energy of incoming electron, with increasing of the atomic number Z of the target, and with energy of the emitted photon approaching the short-wavelength limit. The cross section (3.7) tends to zero as the energy of the emitted photon increases and does not predict the cutoff at the high-energy end of the bremsstrahlung spectrum, shown in Fig. 3.1. This can be overcome by multiplying the Eq. 3.7 by Elwert factor [60]. Other existing corrections allow to apply Bethe-Heitler formula for a wider energy region and also make the predictions of Born approximation more precise by including the screening effects [55, 59, 61, 62]. However, it was already known in 1950s that at extreme relativistic energies Born approximation cross sections are larger than the ones predicted by more precise theories, while at very low energies

the situation is reversed [55, 63]. Later in this section we will compare predictions from different cross section calculations.

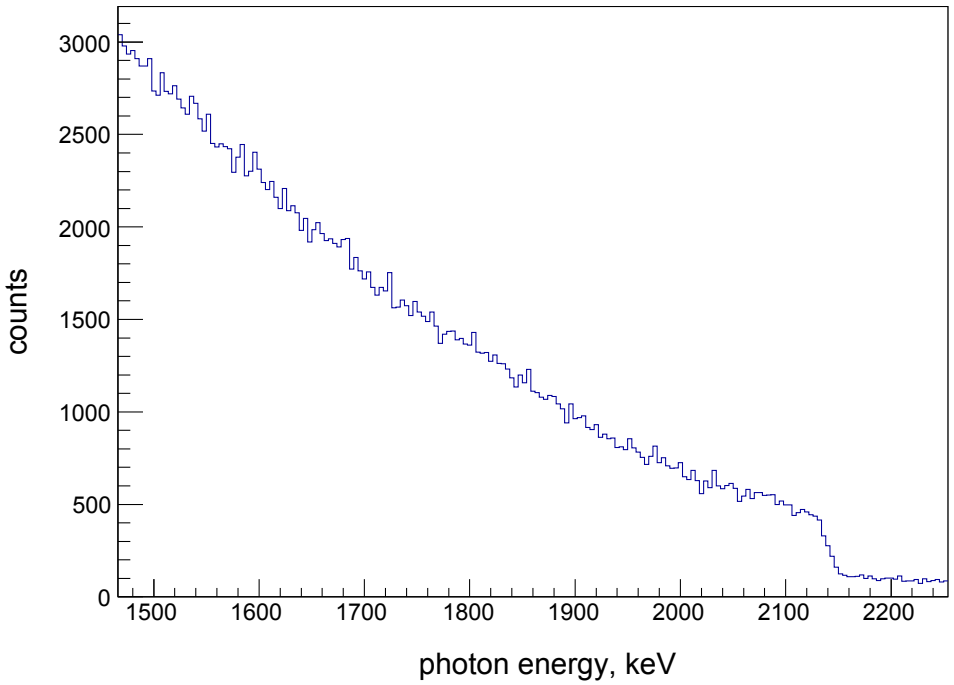

Figure 3.1: Typical bremsstrahlung spectrum measured with a HPGe detector at 90° with respect to the electron beam propagation direction. The electron energy $E_i = 2150\ keV$.

The most accurate way to describe bremsstrahlung is based on the relativistic partial-wave representation of the electron motion in a static (screened) potential of a target atom. This approach is however rather complicated for practical application, as the partial-wave expansion of the initial and final electron states, together with the multipole approximation of the emitted photon, results in large number of expansion terms that have to be summed until convergence is reached. Despite the technical difficulties, the first accurate numerical calculations were performed by Tseng and Pratt already in 1970s [19, 56, 64, 65]. They obtained results for unpolarized single- and double-differential cross sections, i.e., without considering the outgoing electron. Linear polarization of both electron and photon was taken into account in [18] as a part of

detailed studies of bremsstrahlung polarization correlations which will be discussed in next sections. More complex calculations of triple-differential cross section and the corresponding polarization correlations were performed in [66–69]. More recently Yerokhin and Surzhykov found an agreement with calculations of Tseng and Pratt [18] and also extended results up to 2 MeV [24]. In Fig. 3.2 we compare the double-differential cross sections obtained by Tseng and Pratt [64] and Yerokhin and Surzhykov [24] with Born approximation results by Bethe [59].

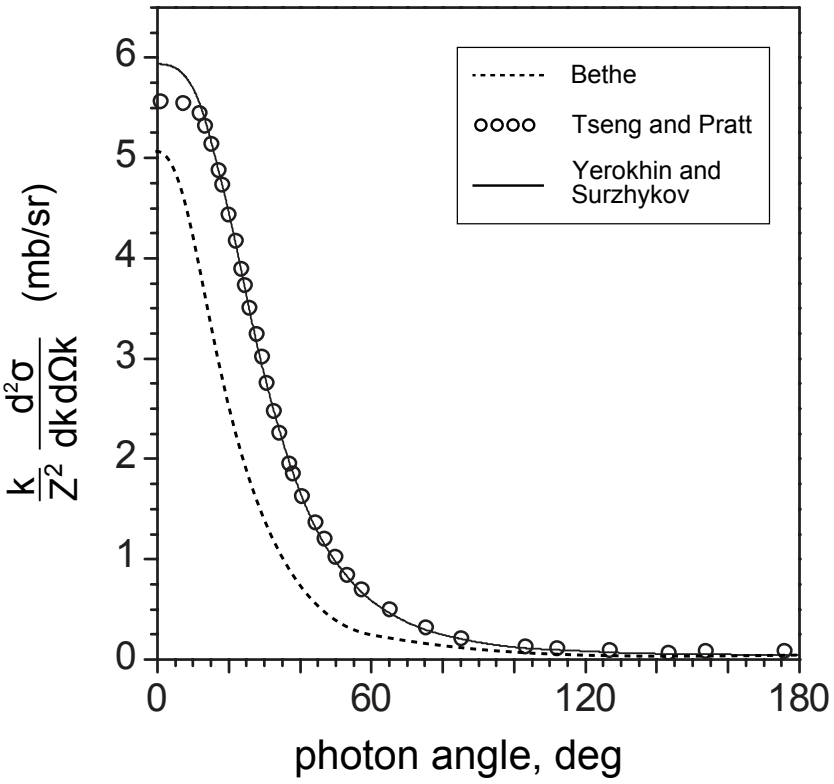

Figure 3.2: Double-differential cross sections obtained by partial-wave expansion and Born approximation. Calculations are performed for the initially unpolarized electrons for Z=79, E_i=500 keV, k=250 keV [24].

3.1.2 Angular distribution

In non-relativistic limit bremsstrahlung can be compared to dipole radiation having the angular distribution $d\sigma/d\Omega \propto sin^2\,\theta$, where θ is the photon emission angle with respect to the dipole axis (see Fig. 3.3a,b). With the increase of the electron energy and entering the relativistic regime photons are emitted predominantly at forward angles, as shown at Fig. 3.3c and d.

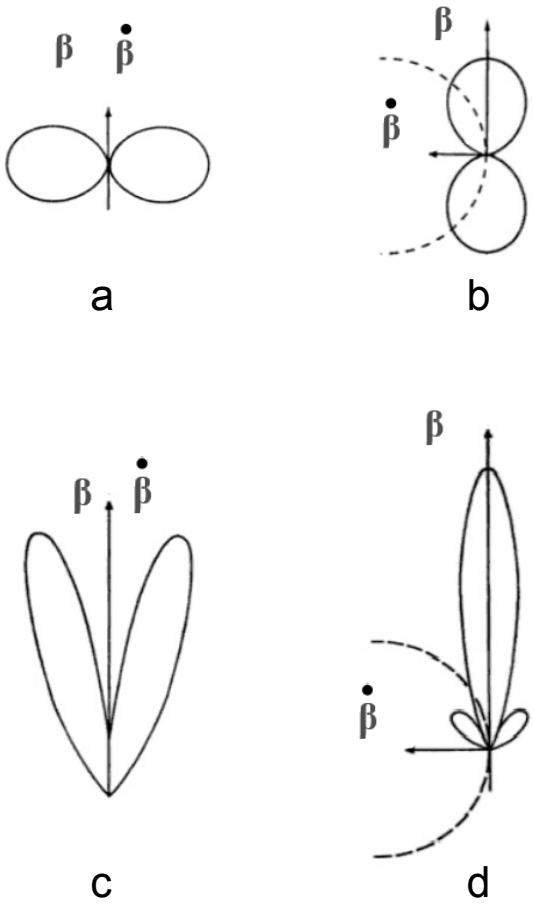

Figure 3.3: Schematic angular distributions typical for non-relativistic (a, b) and relativistic (c, d) regimes with electron acceleration $\dot{\boldsymbol{\beta}}$ parallel and perpendicular to its velocity $\boldsymbol{\beta}$ [58].

Radiation patterns from Fig. 3.3 are summed over all scattering angles of outgoing electrons and have rotational symmetry about the initial electron direction. The picture

changes entirely when considering the bremsstrahlung for fixed trajectory of outgoing electron. Let us take a closer look at the electron motion in the field of a nucleus (see Fig. 3.4a). At the shortest distance to the nucleus the radiation intensity is the highest [58]. Because of the Doppler beaming photons are emitted predominantly in the forward direction. Hence the bremsstrahlung pattern is no longer symmetric but peaked sidewards the outgoing electron trajectory (see Fig. 3.4b).

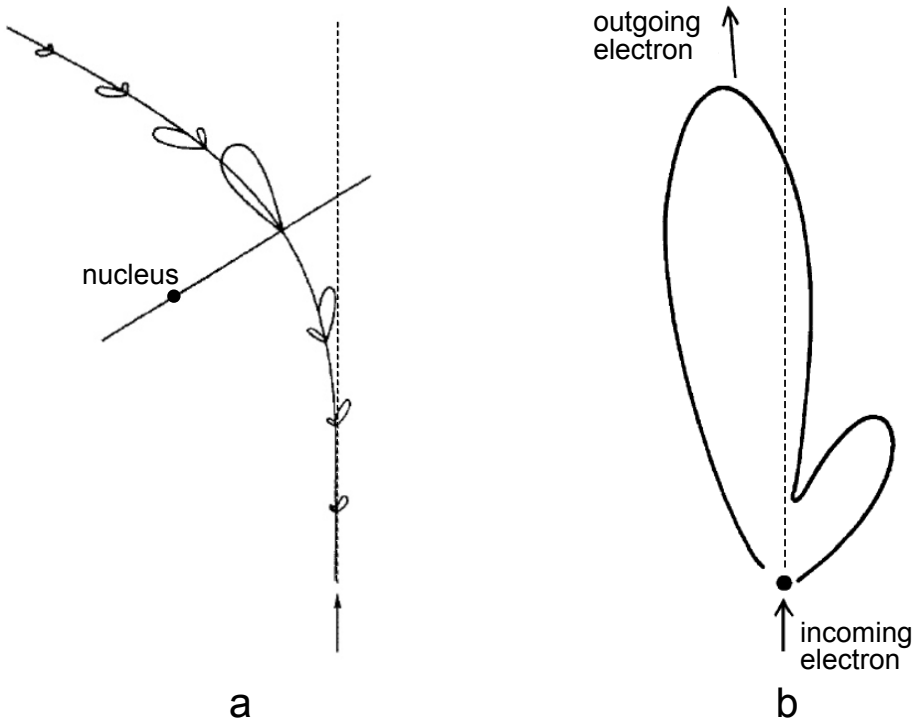

Figure 3.4: a - angular distribution of photon emission during electron motion in the field of a nucleus; b - schematic bremsstrahlung pattern for the fixed direction of outgoing electron [58].

3.1.3 Polarization

One of the first theoretical studies of bremsstrahlung polarization was performed already in 1940s [54]. Gluckstern *et al* [70] included the photon polarization vector $\boldsymbol{e}$ in Bethe-Heitler formula (3.7) and obtained the polarized bremsstrahlung cross section

independent of the initial electron spin state. In 1950s bremsstrahlung was used as an instrument to study polarization properties of electrons in β- and $\mu - e$ decay [71–73]. The first calculations considering the initial electron spin state were made within the Born approximation defining the dependence of circular and linear bremsstrahlung polarization on the photon emission angle, atomic number of the target Z and initial electron energy [10, 72, 74]. More precise calculations of Elwert and Haug by means of Sommerfeld-Maue wave functions [11] included corrections for the scattering of the electrons in the target and a contribution of an electron-electron bremsstrahlung. Nowadays detailed calculations containing the observation of scattered electrons are available for relatively broad energy range [69].

The polarization of a photon beam in a mixed state can be described by the spin-density matrix. Although the photon has a spin $S = 1$, its helicity (i.e., the spin projection on the photon momentum $\boldsymbol{k}$) has only two allowed values: $\lambda = \pm 1$, therefore the spin-density matrix has dimension 2×2 and can be parametrized by three real Stokes parameters [75, 76]:

$$\langle \boldsymbol{k}\lambda \,|\, \rho_\gamma \,|\, \boldsymbol{k}\lambda' \rangle = \frac{1}{2} Tr(\rho_\gamma) \begin{pmatrix} 1 + P_3 & -P_1 + iP_2 \\ -P_1 - iP_2 & 1 - P_3 \end{pmatrix} \tag{3.9}$$

The trace of the density matrix is proportional to the intensity of emitted light. The third parameter P_3 represents the degree of circular polarization, while P_1 and P_2 describe the degree and the angle of linear polarization of the photon in the plane perpendicular to its momentum $\boldsymbol{k}$. Experimentally P_3 is defined by measuring the intensities $I_{\lambda=\pm1}$ of left and right circularly polarized radiation:

$$P_3 = \frac{I_{(+1)} - I_{(-1)}}{I_{(+1)} + I_{(-1)}} \tag{3.10}$$

Parameters P_1 and P_2 are related to the intensity I_χ of the light, linearly polarized

under the different angles χ with respect to the scattering plane (see Fig. 3.5 a,b):

$$P_1 = \frac{I_{0^\circ} - I_{90^\circ}}{I_{0^\circ} + I_{90^\circ}} \tag{3.11}$$

$$P_2 = \frac{I_{45^\circ} - I_{135^\circ}}{I_{45^\circ} + I_{135^\circ}} \tag{3.12}$$

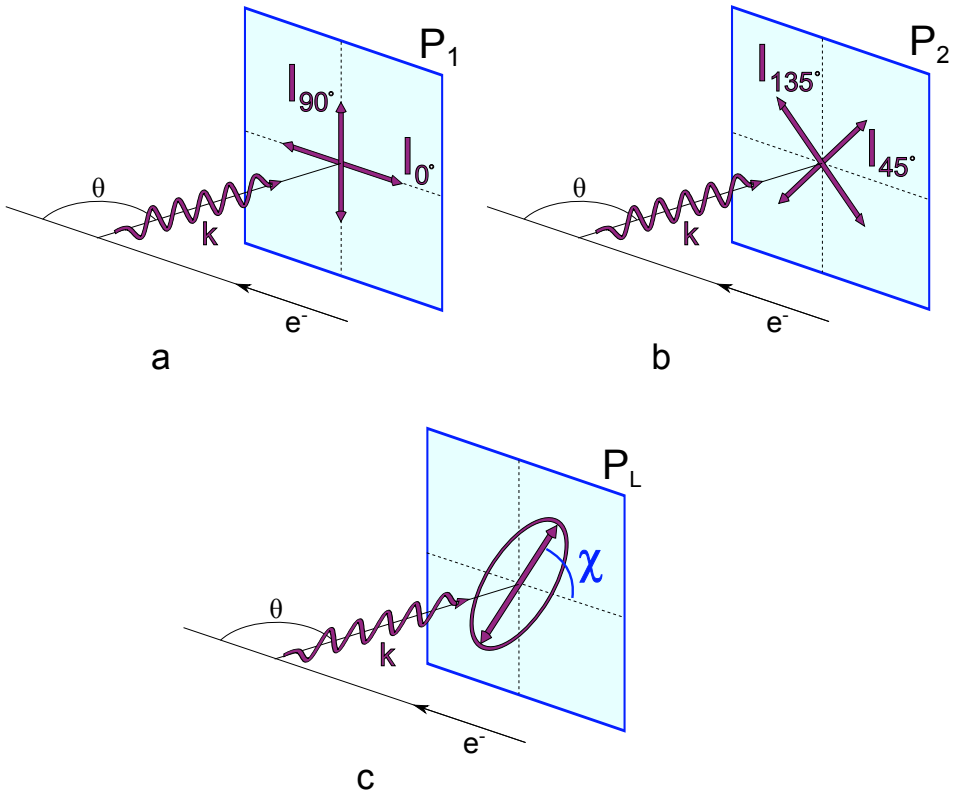

Figure 3.5: Graphical representation of the Stokes Parameters P_1, P_2 and the polarization ellipse. All the angles are defined with respect to the reaction plane given by the initial electron beam propagation direction and the emitted photon momentum.

In case of arbitrary $P_{1,2,3}$ the photon beam is linearly and circularly polarized. The general requirement for Stokes parameters is described by the relation:

$$P_1^2 + P_2^2 + P_3^2 \leq 1 \tag{3.13}$$

For the photons with energies of the order of MeV it is very difficult to measure the circular polarization, therefore within the current work we will discuss only the Stokes parameters P_1 and P_2. In order to analyze different experimental situations, it is more convenient to represent the linear polarization of a photon beam in terms of the polarization ellipse that is defined in the plane, perpendicular to $\boldsymbol{k}$ (see Fig. 3.5c). The relative length of its principal axis represents the degree of linear polarization P_L and the angle χ between the ellipse axis and the scattering plane is referred to as polarization angle. The relation between the Stokes parameters and the degree and angle of linear polarization is given by:

$$P_L = \sqrt{P_1^2 + P_2^2} \tag{3.14}$$

$$\sin 2\chi = \frac{P_2}{P_L}, \quad \cos 2\chi = \frac{P_1}{P_L}, \quad \tan 2\chi = \frac{P_2}{P_1}. \tag{3.15}$$

Due to parity conservation (mirror reflection against the reaction plane for the case of unpolarized electron beam) the photon polarization plane should either coincide with the reaction plane, or be perpendicular to it. Considering the electron spin breaks the mirror symmetry and allows the photon polarization plane to tilt at any angle with respect to the reaction plane. This effect corresponds to nonzero second Stokes parameter P_2 and was studied in the current work.

3.1.4 Bremsstrahlung polarization correlations

First predictions that bremsstrahlung is influenced by electron spin were made by Breit already in 1950s [70]. Tseng and Pratt were the first to study the correlation between all three spin components and both linear and circular polarization of emitted radiation [18]. In principle the spin orientation of the outgoing electron may also affect the bremsstrahlung intensity and polarization. Thus the triple-differential cross section

including all the polarization correlations is given by [58, 77]:

$$\frac{d^3\sigma^{pol}}{dk\,d\Omega_k\,d\Omega_{p_f}} = \frac{d^3\sigma^{unpol}}{dk\,d\Omega_k\,d\Omega_{p_f}} \left[\frac{1}{4}\sum_{l,m,n=0}^{3} C_{lmn}\,\zeta_l\,\xi_m\,\zeta_n\right]. \tag{3.16}$$

Here ζ_l and ζ_m describe the spin states of the incoming and outgoing electron respectively and ξ_m characterize the polarization of the emitted photon. Polarization correlation coefficients C_{lmn} are the real numbers that satisfy the condition $0 \leq C_{lmn} \leq 1$, since the cross sections cannot be negative. The interpretation of indexes l, m, n is presented in Table 3.1. So far only the coefficients C_{lm0} for unpolarized outgoing electrons have been calculated [66–68]. The term $\frac{d^3\sigma^{unpol}}{dk\,d\Omega_k\,d\Omega_{p_f}}$ stands for the triple-differential cross section that is averaged over the photon polarization and doesn't take into account the electron spin.

k, n	Electron	l	Photon
0	unpolarized	0	$d\sigma$, total
1	transversely polarized (within the reaction plane)	1	linearly polarized, P_2
2	vertically polarized (perp. to the reaction plane)	2	circularly polarized, P_3
3	longitudinally polarized	3	linearly polarized, P_1

Table 3.1: Definition of polarization correlation coefficients C_{lmn} by Tseng and Pratt [18].

In the current work we compare our experimental results with calculations of Yerokhin and Surzhykov. They describe polarization correlations using the Stokes parameters $P_{1,2,3}(S_x, S_y, S_z)$ and the differential cross section $d\sigma(S_x, S_y, S_z)$ as a function of the polarization vector of the incident electron $\boldsymbol{S} = (S_x, S_y, S_z)$, atomic number of the target nucleus, electron and photon energies and the observation angle [24]. Here the scattered electron is not observed and thus only the polarization correlations between the incident electron and the emitted photons are considered. The coordinate system in the laboratory frame is used in the description of bremsstrahlung process (see Fig. 3.6).

The z axis is defined along the initial electron momentum $\boldsymbol{p}_i$. The electron propagation direction and the momentum $\boldsymbol{k}$ of emitted photon determine the reaction plane xz.

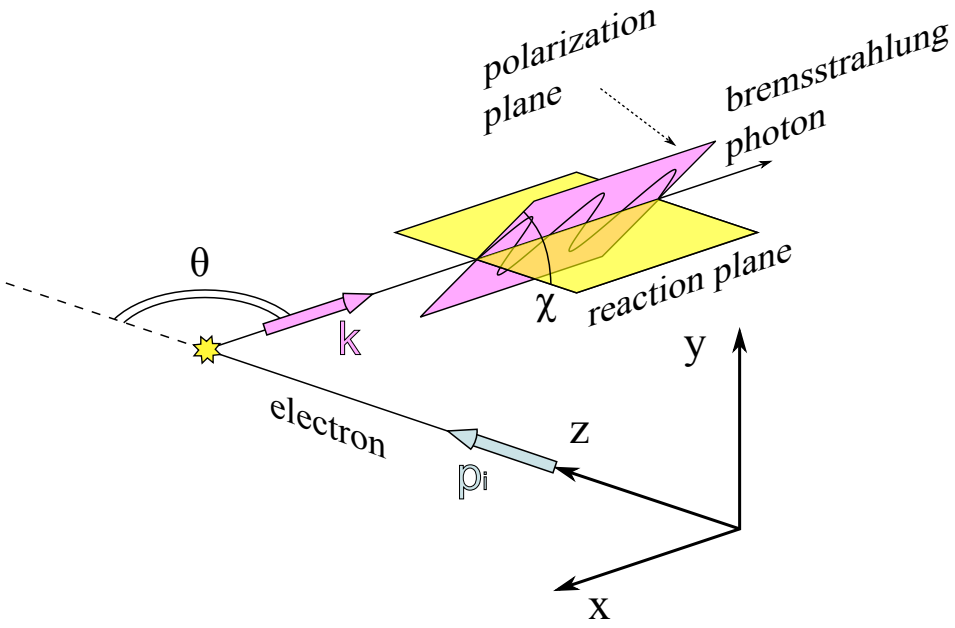

Figure 3.6: The process of bremsstrahlung in a laboratory frame. Emitted photon is linearly polarized at the angle χ with respect to the reaction plane xz. Scattered electron is not observed.

Yerokhin and Surzhykov analyze the bremsstrahlung process using the density matrix theory. The spin-density matrix of the photon beam can be written as:

$$\langle \boldsymbol{k}\lambda \,|\, \rho_\gamma \,|\, \boldsymbol{k}\lambda' \rangle = \sum_{m_i m_i' m_f} \int d\Omega_f \langle \boldsymbol{p}_i\, m_i \,|\, \boldsymbol{\alpha} \boldsymbol{u}_\lambda\, e^{i\boldsymbol{k}\boldsymbol{r}} \,|\, \boldsymbol{p}_f m_f \rangle^* \langle \boldsymbol{p}_i\, m_i' \,|\, \boldsymbol{\alpha} \boldsymbol{u}_{\lambda'}\, e^{i\boldsymbol{k}\boldsymbol{r}} \,|\, \boldsymbol{p}_f m_f \rangle \times \langle \boldsymbol{p}_i\, m_i \,|\, \rho_e \,|\, \boldsymbol{p}_i\, m_i' \rangle, \tag{3.17}$$

where $\boldsymbol{k}$ is the momentum and $\lambda = \pm 1$ is the helicity of the photon, $|\, \boldsymbol{p}_i\, m_i \rangle$ and $|\, \boldsymbol{p}_f m_f \rangle$ denote the initial and the final continuum electron states with asymptotic momenta $\boldsymbol{p}_{i,f}$ and spin projections onto the z axis $m_{i,f} = \pm 1/2$. The photon is described by a plane wave $\boldsymbol{u}_\lambda e^{i\boldsymbol{k}\boldsymbol{r}}$ with the components of the unit polarization vector $\boldsymbol{u}_\lambda$ defined

as $u_1 = (u_x + iu_y)/\sqrt{2}$ and $u_{-1} = (u_x - iu_y)/\sqrt{2}$. The integration is performed over the scattering angle of the outgoing electron Ω_f. The polarization of the initial electron beam is described by the electron density matrix ρ_e, which can be expressed in terms of so-called statistical tensors $\rho^{(i)}_{kq}$ [75]:

$$\langle \boldsymbol{p}_i\, m_i \,|\, \rho_e \,|\, \boldsymbol{p}_i\, m_i' \rangle = \sum_{kq} (-1)^{1/2-m_i'} \langle 1/2\, m_i\, 1/2\, -m_i' | kq \rangle \rho^{(i)}_{kq}. \tag{3.18}$$

For the spin-1/2 particle, such as electron, only the tensors with rank $k, q = 0$ and 1 exist. The relation between the initial electron polarization $\boldsymbol{S} = (S_x, S_y, S_z)$ and the components of $\rho^{(i)}_{kq}$ can be written as:

$$\rho^{(i)}_{00} = \frac{1}{\sqrt{2}}, \qquad \rho^{(i)}_{10} = \frac{1}{\sqrt{2}} S_z, \qquad \rho^{(i)}_{1\mp1} = \mp\frac{1}{2}(S_x \mp iS_y). \tag{3.19}$$

For the further evaluation of polarization correlation coefficients, one needs to decompose both electron (incoming "+" and outgoing "-") and photon wave functions into partial waves [78]:

$$|\, \boldsymbol{p} m \rangle = 4\pi \sum_{k\mu} i^l e^{\pm i\Delta_k} \langle l\, m_l\, 1/2\, m\, | j\mu \rangle\, Y^*_{lm_l}(\boldsymbol{p}) \begin{pmatrix} g_{\varepsilon,k} & \chi_{k\mu}(\boldsymbol{r}) \\ if_{\varepsilon,k} & \chi_{-k\mu}(\boldsymbol{r}) \end{pmatrix} \tag{3.20}$$

$$\boldsymbol{u}_\lambda e^{e\boldsymbol{kr}} = \sqrt{2\pi} \sum_{LM_p} i^L \sqrt{2L+1}\, (i\lambda)^p\, \boldsymbol{a}^{(p)}_{LM}(\boldsymbol{r})\, D^L_{M\lambda}(\boldsymbol{k}), \tag{3.21}$$

with total and orbital angular momenta $j = |\, k\,| - 1/2$ and $l = |\, k + 1/2\,| - 1/2$, Dirac phase $\Delta_k = \sigma_k + \pi/2(l+1)$ dependent on the asymptotic phase σ_k of the Dirac wave function. The term $Y^*_{lm_l}(\boldsymbol{p})$ stands for the spherical harmonics and g and f are the upper and lower radial components and χ_{km} are the spherical spinors. In Eq. (3.21) $D^L_{M\lambda}(\boldsymbol{k})$ is the Wigner's rotation matrix and $\boldsymbol{a}^{(p)}_{LM}(\boldsymbol{r})$ are the electric ($p = 1$) and magnetic ($p = 0$) vectors.

After inserting (3.18), (3.20) and (3.21) into Eq. 3.17 the density matrix of the final state can be written as [24]:

$$\begin{aligned}\langle \boldsymbol{k}\lambda \,|\, \rho_\gamma \,|\, \boldsymbol{k}\lambda' \rangle =& 8(2\pi)^4 \sum_{k_i k_i' k_f} \sum_{LL'kgt} \sum_{\gamma_1\gamma_2} D^g_{\gamma_1\gamma_2}(\boldsymbol{k})\, \rho^{(i)}_{k,-\gamma_1}\, i^{l_i - l_i' - L + L'}\, e^{\Delta_{k_i} - i\Delta_{k_i'}} \\ & \times \{j_i, j_i', l_i, l_i', L, L', g, k\}^{1/2} (-1)^{j_i' - j_f + l_i + g + k} \langle L'\lambda' L - \lambda | g\gamma_2\rangle \\ & \times \langle l_i 0 l_i' 0 | t0\rangle \langle g - \gamma_1 k \gamma_1 | t0\rangle \begin{Bmatrix} L & j_f & j_i \\ j_f' & g & L' \end{Bmatrix} \begin{Bmatrix} 1/2 & 1/2 & k \\ j_i' & j_i & g \\ l_i' & l_i & t \end{Bmatrix} \\ & \times \sum_{pp'} (-i\lambda)^p (i\lambda')^{p'} \langle \varepsilon_i k_i \,||\, \boldsymbol{\alpha}\boldsymbol{\alpha}^{(p)}_L \,||\, \varepsilon_f k_f\rangle^* \langle \varepsilon_i k_i' \,||\, \boldsymbol{\alpha}\boldsymbol{\alpha}^{\prime(p')}_L \,||\, \varepsilon_f k_f\rangle, \end{aligned} \tag{3.22}$$

with the introduced symbol $\{j_1, j_2, ...\} = (2j_1 + 1)(2j_2 + 1)...$.

Four possible spin states of the incoming electron (see Table 3.1) form 16 correlation coefficients with the direction $d\sigma(S_x, S_y, S_z)$ and the polarization $P_{1,2,3}(S_x, S_y, S_z)$ of the emitted photon. However, some of them are dependent on other and some are generally equal to zero. Eq. 3.22 results in following rules:

$$d\sigma(0,0,0) = d\sigma(1,0,0) = d\sigma(0,0,1), \tag{3.23}$$

$$P_1(0,0,0) = P_1(1,0,0) = P_1(0,0,1), \tag{3.24}$$

$$P_2(0,0,0) = P_2(0,1,0) = 0, \tag{3.25}$$

$$P_3(0,0,0) = P_3(0,1,0) = 0, \tag{3.26}$$

As a consequence, only 8 independent non-zero polarization correlations exist:

$$P_1(0,0,0) = C_{03}, \tag{3.27}$$

$$P_2(1,0,0) = -C_{11}, \tag{3.28}$$

$$P_2(0,0,1) = C_{31}, \tag{3.29}$$

$$P_3(1,0,0) = -C_{12}, \tag{3.30}$$

$$P_3(0,0,1) = C_{32}, \tag{3.31}$$

$$P_1(0,0,0) - P_1(0,1,0) = C_{23}, \tag{3.32}$$

$$1 - \frac{d\sigma(0,1,0)}{d\sigma(0,0,0)} = C_{20}, \tag{3.33}$$

where C_{lm} correspond to the polarization correlation coefficients in terminology of Tseng and Pratt [18].

In order to determine the relations for the cross section and Stokes parameters for arbitrary polarized electrons, we express the electron density matrix ρ_e as:

$$\begin{aligned}
\langle \boldsymbol{p}_i\, m_i \,|\, \rho_e \,|\, \boldsymbol{p}_i\, m_i' \rangle = {} & \frac{1}{2}\delta_{m_i m_i'} + \frac{1}{2} S_z\, \delta_{m_i m_i'} (-1)^{1/2-m_i} \\
& + \frac{1}{2} S_x\, \delta_{m_i -m_i'} + \frac{1}{2} i S_y\, \delta_{m_i -m_i'} (-1)^{1/2+m_i} \\
= {} & (1 - S_x - S_y - S_z) \langle \boldsymbol{p}_i\, m_i \,|\, \rho_e(0,0,0) \,|\, \boldsymbol{p}_i\, m_i' \rangle + S_x \langle \boldsymbol{p}_i\, m_i \,|\, \rho_e(1,0,0) \,|\, \boldsymbol{p}_i\, m_i' \rangle \\
& + S_y \langle \boldsymbol{p}_i\, m_i \,|\, \rho_e(0,1,0) \,|\, \boldsymbol{p}_i\, m_i' \rangle + S_z \langle \boldsymbol{p}_i\, m_i \,|\, \rho_e(0,0,1) \,|\, \boldsymbol{p}_i\, m_i' \rangle,
\end{aligned} \tag{3.34}$$

where $\rho_e(0,0,0)$ stands for the initially unpolarized electrons and $\rho_e(1,0,0)$, $\rho_e(0,1,0)$ and $\rho_e(0,0,1)$ correspond to the electron beam completely polarized along x, y and

z axes respectively. Inserting expression (3.34) to the photon density matrix relation (3.17) we get [57]:

$$\begin{aligned}\langle \boldsymbol{k}\lambda \,|\, \rho_\gamma \,|\, \boldsymbol{k}\lambda' \rangle = (1 - S_x - S_y - S_z)\langle \boldsymbol{k}\lambda \,|\, \rho_\gamma(0,0,0) \,|\, \boldsymbol{k}\lambda' \rangle + S_x \langle \boldsymbol{k}\lambda \,|\, \rho_\gamma(1,0,0) \,|\, \boldsymbol{k}\lambda' \rangle \\ + S_y \langle \boldsymbol{k}\lambda \,|\, \rho_\gamma(0,1,0) \,|\, \boldsymbol{k}\lambda' \rangle + S_z \langle \boldsymbol{k}\lambda \,|\, \rho_\gamma(0,0,1) \,|\, \boldsymbol{k}\lambda' \rangle.\end{aligned} \tag{3.35}$$

Based on Eq. 3.35 the formulas for the bremsstrahlung polarization and intensity can be derived. The differential cross section is given by:

$$\begin{aligned}d\sigma = c \cdot \sum_\lambda \langle \boldsymbol{k}\lambda \,|\, \rho_\gamma \,|\, \boldsymbol{k}\lambda \rangle = (1 - S_x - S_y - S_z)\, d\sigma(0,0,0) + S_x\, d\sigma(1,0,0) \\ + S_y\, d\sigma(0,1,0) + S_z\, d\sigma(0,0,1) = (1 - S_y C_{20}) d\sigma(0,0,0).\end{aligned} \tag{3.36}$$

Here, the final expression was obtained by applying the symmetry property of the differential cross section (3.23) and the relation (3.33). Following the Eq. 3.9 the first Stokes parameter can be written as:

$$P_1 = \frac{\langle \boldsymbol{k}+1 \,|\, \rho_\gamma \,|\, \boldsymbol{k}-1 \rangle + \langle \boldsymbol{k}-1 \,|\, \rho_\gamma \,|\, \boldsymbol{k}+1 \rangle}{\sum_\lambda \langle \boldsymbol{k}\lambda \,|\, \rho_\gamma \,|\, \boldsymbol{k}\lambda' \rangle}. \tag{3.37}$$

Using symmetry properties (3.23) and (3.24) and relation (3.33), P_1 we get:

$$P_1 = \frac{P_1(0,0,0)(1 - S_y) + S_y P_1(0,1,0)(1 - C_{20})}{1 - S_y C_{20}}. \tag{3.38}$$

Expression for Stokes parameter P_2 can be obtained in a similar way:

$$P_2 = \frac{S_x P_2(1,0,0) + S_z P_2(0,0,1)}{1 - S_y C_{20}} \tag{3.39}$$

3.2 Experimental studies

First bremsstrahlung measurements concentrated on testing the cross section and angular distribution predictions of non-relativistic theory of Sommerfeld and Born approximation. The simplest setups consisted of an electron scattering target and a detector measuring the radiation intensity at different scattering angles [79, 80]. Along with advances in experimental techniques the coincident experiments became possible allowing measurements of bremsstrahlung angular distribution as well as polarization for fixed directions of outgoing electrons [81, 82]. The progress in development of polarized electron sources enabled more extensive studies including the control of an electron spin. The most differential case studied so far is the linear polarization of bremsstrahlung x rays produced by polarized electrons [20, 21]. The particular interest in such measurements arises from the sensitivity of x ray polarization to the dynamics of the scattering electron at the close distance to the nucleus. There the Coulomb fields reach high values comparable to Schwinger limit of 10^{16} V. The most detailed study of bremsstrahlung process would be a measurement of the triply differential cross section including the control of polarization states of all the particles involved, where the outgoing electron and the emitted photon are detected in coincidence. Due to the high level of complexity such an experiment has never been performed.

3.2.1 Cross section

Measurements of bremsstrahlung cross section (both total and differential in photon energy and angle) were performed in 1940s-1950s. The outgoing electrons were not observed and the photons were registered either by a gas ionization chamber or a scintillator detector. Although the covered energy range was rather wide (from several keV [83, 84] up to hundreds MeV [85–87]), very few experiments provided a satisfactory test of theory. The most extensive measurements were performed by Motz

for incident electron energies of 50 keV [79] and 0.5- and 1 MeV [80]. The experimental setup is shown in Fig. 3.7. Bremsstrahlung photons were produced in collisions of electrostatically accelerated electrons with the thin foil targets of aluminum, beryllium and gold (the list of target thicknesses for both experiments is presented in Table 3.2). The intensities of the emitted x rays were measured at different angles θ with respect to the initial electron beam with the help of a NaI(Tl) detector, mounted in a shielding container. The round opening in the front side of the shielding allowed for the angular resolution of $\Delta\theta < 1^{\circ}$. Measured cross sections are presented in Fig. 3.8 and Fig. 3.9.

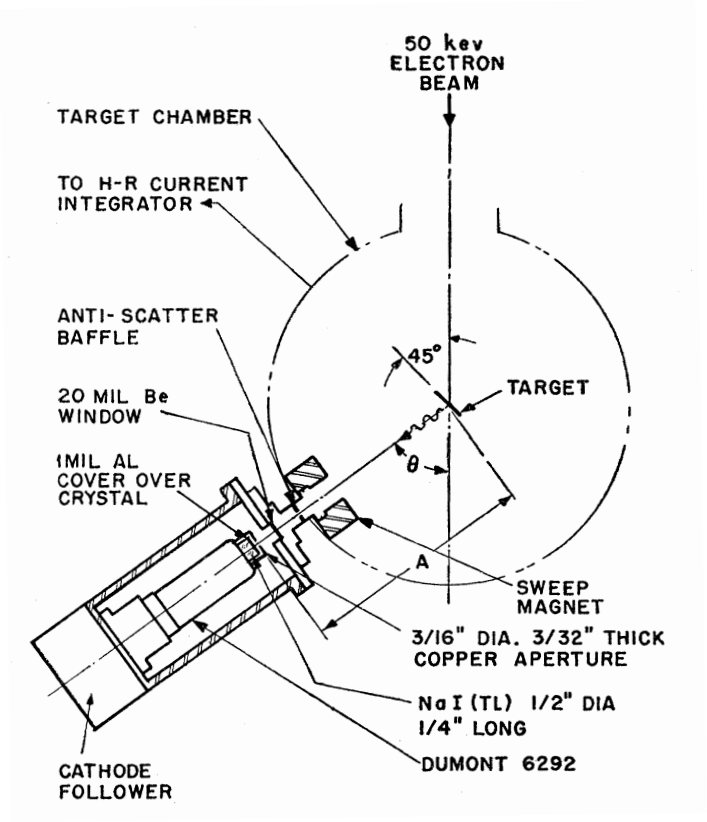

Figure 3.7: Scheme of the experimental setup [79, 80]. Bremsstrahlung intensity was measured at the angles $\theta = 10°, 20°, 30°, 40°, 50°, 60°, 70°, 90°, 110°, 140°$. In the experiment with 50 keV electrons the distance between the target and the detector was $A = 29.2\ cm$ and the collimator diameter was $d = 0.24\ cm$. In the 0.5- and 1 MeV measurement the front side of the detector was shielded from the unwanted x rays with 30 cm of lead with the collimator diameter $d = 0.9\ cm$; the distance A was 78.7 cm.

target material	target thickness, mg/cm^2	
	50 keV	0.5- and 1 MeV
Be	–	4.30
Al	0.017, 0.038	0.63, 1.00
Au	0.010, 0.022	0.22, 0.43

Table 3.2: Targets used in the 50 keV [79] and 0.5- and 1 MeV [80] measurements.

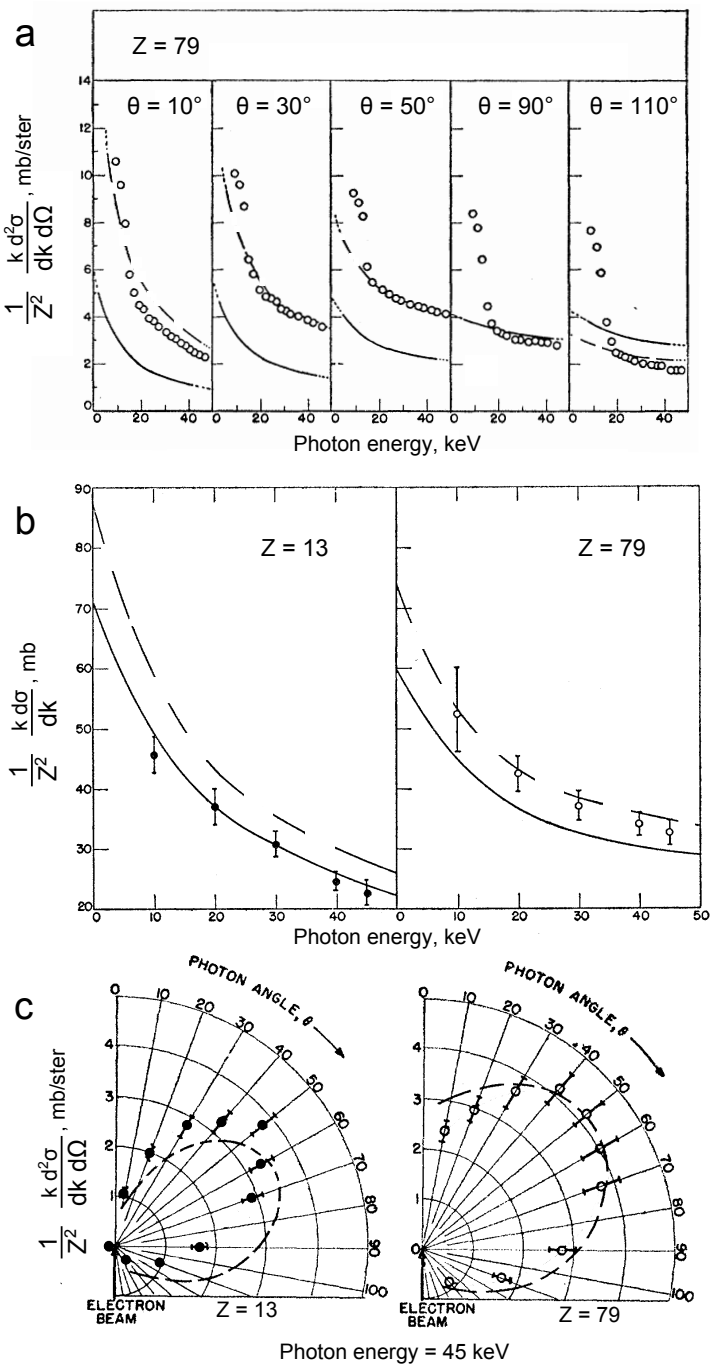

Figure 3.8: (a), (b) Differential cross sections of 50 keV bremsstrahlung for golden and aluminum targets [79]. In Fig. (b) the cross section is integrated over the photon emission angle θ. (c) Angular distribution of 45 keV bremsstrahlung. The solid curves represent the non-relativistic Sommerfeld cross sections [54] and the dashed curves were obtained by multiplying these cross sections by the relativistic correction factor $(1 - \beta_0 cos\,\theta)^{-2}$.

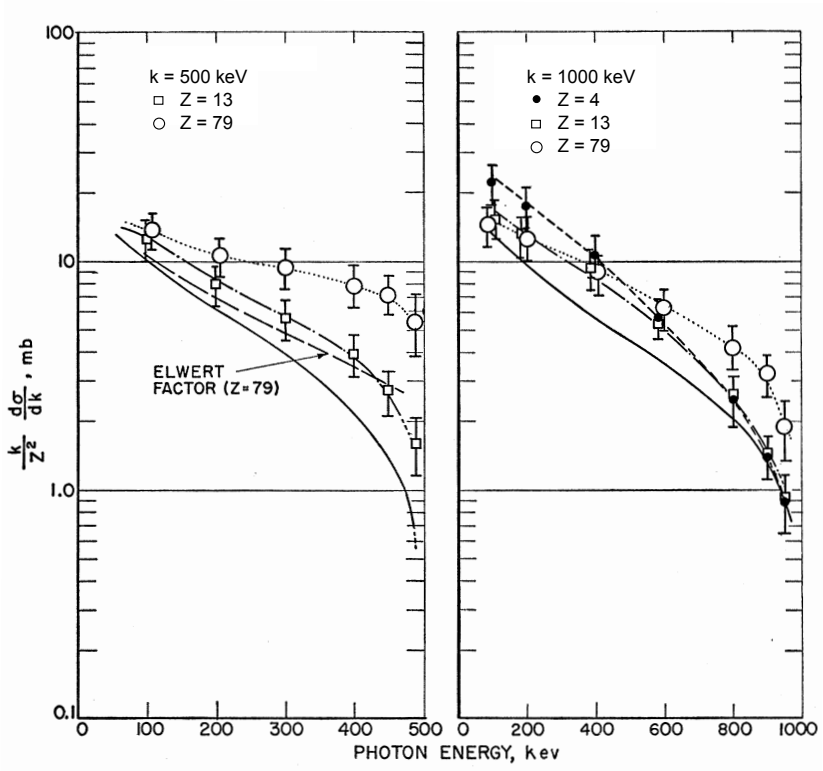

Figure 3.9: Bremsstrahlung cross sections integrated over the photon emission angle θ for the incident electron energies of 0.5- and 1 MeV [80]. Solid lines represent Bethe-Heitler calculations [70]. The dashed line on the left part is obtained by multiplying the Bethe-Heitler cross section by the Elwert factor for Z=79 [60].

Experimental results revealed rather significant disagreement with existing theories especially at the photon energies approaching the short wavelength limit and at the extreme values of 0° and 180° of emission angle θ. Bethe-Heitler theory was confirmed to underestimate the cross sections in the 1 MeV energy range. Kirkpatrick calculations of Sommerfeld cross section showed a reasonable agreement only at emission angles around 50° while after integration over θ non-relativistic predictions turned out to be not precise for the low Z targets. It was clearly demonstrated that in order to accurately describe the process of bremsstrahlung, relativistic and screening effects have to be taken into account.

First experimental studies of triple-differential cross section were performed by Nakel in 1960s [88, 89]. Bremsstrahlung was produced by the 300 keV electron beam hitting the thin golden target. Emitted photons were registered by a NaI(Tl) detector in coincidence with 170 keV outgoing electrons with scattering angles of 0°, 5° and 10°. Experimental results were in good agreement with predictions of Elwert and Haug [90]. Since the measured angular distributions were not absolute, they were normalized at maximum of theoretical calculations (see Fig. 3.10).

The angular distribution of the absolute triple-differential cross section was first measured for silver targets by Aehlig and Scheer [81]. Their experimental results for the incident electron energy of 180 keV and the photon energy of 80 keV were in a good agreement with calculations of Elwert and Haug [90].

Similar to the Mott scattering, spin-orbit interaction causes left-right asymmetry of bremsstrahlung emission in case when the initial electron beam is polarized perpendicularly to the reaction plane (vertical polarization). Experimental studies of this phenomenon without observation of the outgoing electrons were performed in [16, 17, 91, 92]. The first electron-photon coincidence measurement was reported by Mergl *et al.* in 1992 [93]. The scheme of experimental setup is shown in Fig. 3.11a. A 300 keV vertically polarized electron beam collided with the 50 μg/cm^2 thick golden target. The degree of the electron beam polarization was in range of 35% to 40%. A HPGe detector was used to register the emitted photons while the scattered electrons were detected by a plastic scintillator at the angles of 0°, 20° and 45° with respect to the initial electron beam propagation direction. The magnetic spectrometer selected outgoing electrons of 200±5 keV. Bremsstrahlung angular distribution was measured for two opposite electron beam polarization settings. Namely, for the spin orientations *up* and *down* perpendicularly to the reaction plane. All the other experimental conditions were preserved. Polarization of emitted photons as well as one of outgoing electrons was neglected.

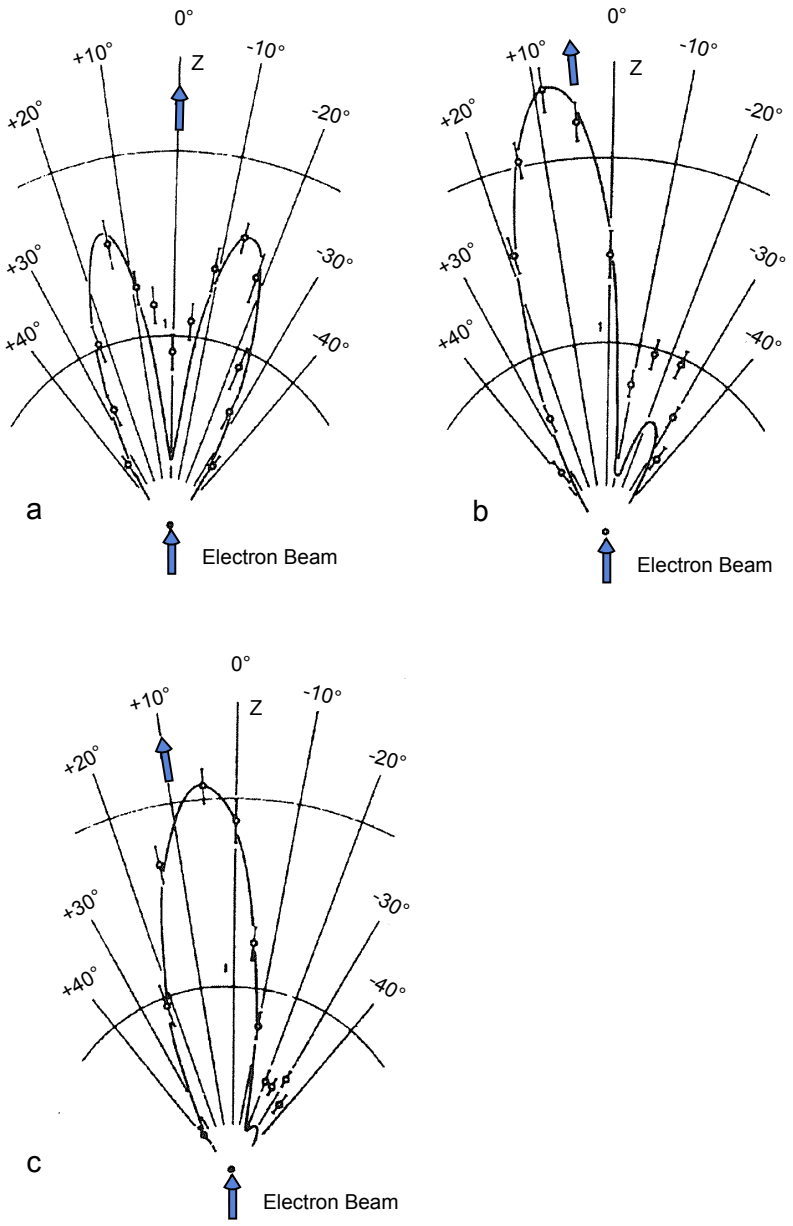

Figure 3.10: Measured angular distribution for the electron scattering angles of 0° (a), 5° (b) and 10°(*c*) [88, 89]. Solid lines represent the calculations of Elwert and Haug [90].

The measured asymmetry corresponds to the coefficient C_{200} in terminology of Tseng

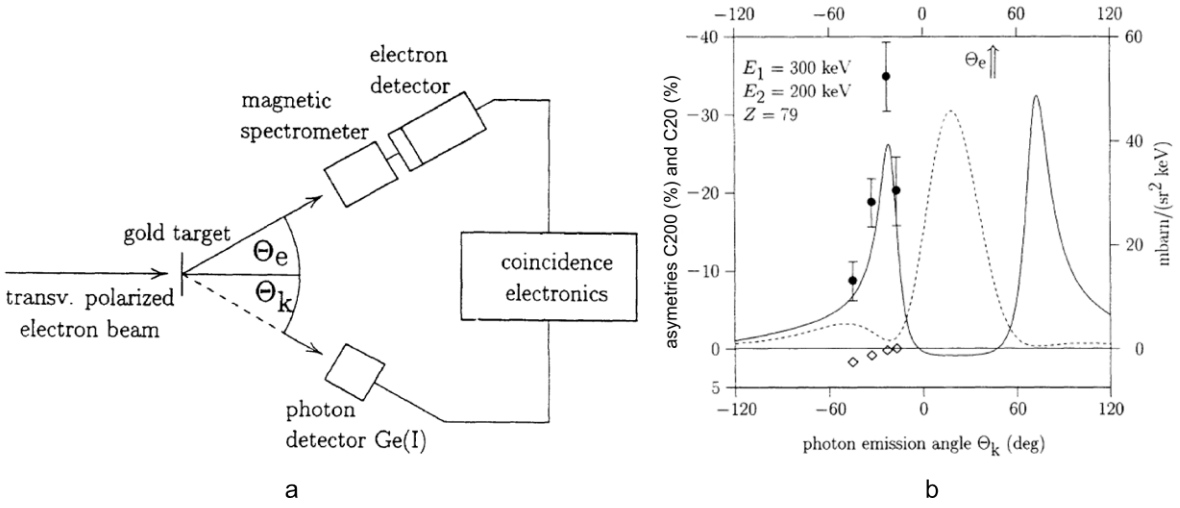

Figure 3.11: (a) Scheme of the experimental arrangement for measuring the bremsstrahlung emission asymmetry [93]. The electron beam was polarized perpendicularly to the reaction plane. (b) Measured asymmetry as a function of the photon emission angle θ for the incident electron beam energy 300 keV and outgoing electrons of energy 200 keV and scattering angle $\theta_e = 45°$. Solid line represents the calculations of Haug [15] and the dashed line denotes the bremsstrahlung cross section for initially unpolarized electron beam [90]. Open diamonds give the non-coincident emission asymmetry C_{20} measured within the same experiment.

and Pratt or $d\sigma(0,1,0)$ in terms of Yerokhin and Surzhykov (see Table 3.1):

$$C_{200} = \frac{I\uparrow - I\downarrow}{I\uparrow + I\downarrow} \cdot \frac{1}{|\boldsymbol{S}|}, \tag{3.40}$$

where $I\uparrow$ ($\downarrow$) denotes the bremsstrahlung intensity for spin-up (down) and $\boldsymbol{S}$ stands for the degree of polarization of the electron beam. The measured C_{200} as a function of the photon emission angle for electron scattering angle of 45° is presented in Fig. 3.11b. Experiment revealed that the highest asymmetry of bremsstrahlung emission corresponded to the region of small cross section (dashed curve). Therefore the detailed studies only possible by means of a coincidence measurement, whereas non-coincidence experiments result in a very low level of anisotropy (open diamonds in Fig. 3.11b). Measured values of C_{200} turned out to be in good agreement with the predictions of

Haug [15]. The relativistic partial wave calculations by Tseng [68] and the recent ones by Müller [69] match the experimental results excellently except one data point.

3.2.2 Linear polarization and polarization correlations

In early studies bremsstrahlung linear polarization was measured for unpolarized electron beam as a function of photon energy, photon emission angle, initial electron energy and the target atomic number [94–97]. The outgoing electrons were not observed. For the unpolarized electron beam the second Stokes parameter P_2 is zero (see Eq. 3.25 in Section 3.1.4) and the photon linear polarization corresponds to the first Stokes parameter $P_L = P_1 = (I_{0^\circ} - I_{90^\circ})/(I_{0^\circ} + I_{90^\circ})$. In a number of experiments the reverse of linear polarization was observed, i.e., low energy photons were polarized perpendicularly to the reaction plane ($P_L < 0$), while high energy photons were polarized parallel to the reaction plane ($P_L > 0$).

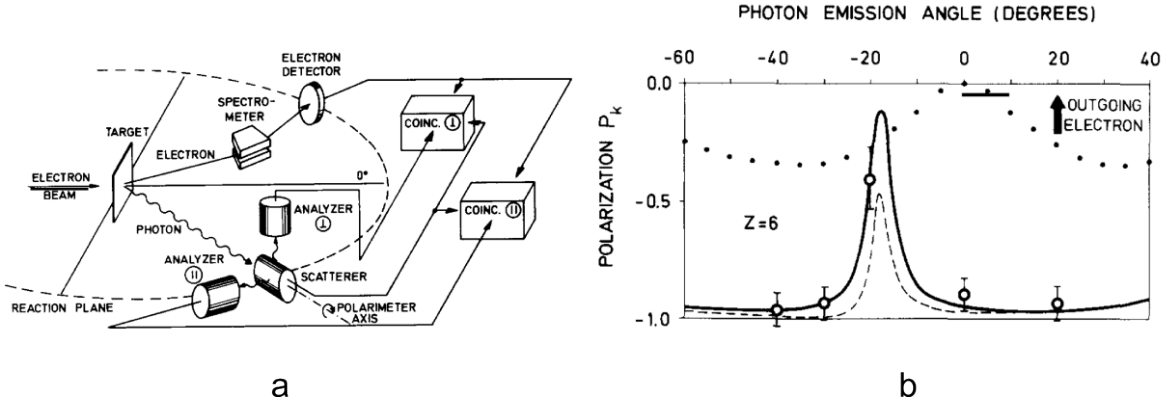

Figure 3.12: (a) Experimental arrangement for the coincidence measurement of bremsstrahlung linear polarization [82, 98]. Only two out of four photon analyzers are shown for simplicity. (b) Measured linear polarization as a function of the photon emission angle for initial electron beam energy of 300 keV, outgoing electron energy 140 keV and the electron scattering angle +20°. The solid line gives the theoretical predictions by Elwert and Haug [11]. The dashed line shows the calculations without corrections for experimental factors. The dotted line represents the polarization integrated over all directions of outgoing electrons [98].

First electron-photon coincidence measurements of bremsstrahlung polarization were reported by Behncke and Nakel [82, 98] and later by Bleier and Nakel [99]. The scheme of the experimental setup from [82] and [98] is shown in Fig. 3.12a. The 300 keV beam of unpolarized electrons impinged on a carbon target. Bremsstrahlung linear polarization was measured at different emission angles by means of Compton polarimetry technique applied to the active photon scatterer (plastic scintillator) and four NaI(Tl) analyzers placed in the plane perpendicular to the photon propagation direction (this method is described in details in Section 2.8). Coincidence events included the detection of an outgoing electron of specific energy and direction and the signal from both the photon scatterer and either of analyzers. The quantity measured was the ratio $I_\perp/I_\parallel$ between the number of photons scattered perpendicularly and parallel to the reaction plane. The linear polarization was then calculated as:

$$P_L = \frac{R+1}{R-1} \cdot \frac{1 - I_\perp/I_\parallel}{1 + I_\perp/I_\parallel}, \tag{3.41}$$

where R is the the asymmetry ratio of Compton polarimeter obtained by a Monte-Carlo simulation. A simple classical model predicts radiation emitted by a moving electron to be completely polarized within the reaction plane. However, experiment revealed the strong dependence of polarization degree on emittance angle (see Fig. 3.12b). This effect can be explained by taking into account the electron spin. The orbital motion of electron and change of spin orientation both contribute significantly to bremsstrahlung process even for the initially unpolarized electron beam [5]. Partial depolarization of the emitted photons is caused by the spin-flip radiation. Figure 3.12b demonstrates that for the selected electron scattering angle of $+20^\circ$ at photon emission angles around -20° the influence of the electron spin is the strongest.

More detailed investigations of spin effects in bremsstrahlung require the control of both the electron and the photon polarization. Due to high complexity such studies were stalled for two decades and only recently became possible. The first measurement

of the correlation between the electron spin direction and bremsstrahlung linear polarization was performed by S. Tashenov *et al.* [20, 57]. It was observed that the photon polarization plane rotates with respect to the reaction plane as a result of interaction of an electron spin with a field induced by the upcoming atomic nucleus, the spin-orbit interaction. The tilt angle was measured with an extremely high precision of 7 mrad. A 100 keV electron beam collided with a gold target and produced bremsstrahlung x rays. Emitted photons were collimated and then scattered by an iron plate (see Fig. 3.13). A high purity segmented germanium detector was placed behind the x-ray shielding so that the outer segments could register only the scattered photons. By measuring the azimuthal angular distribution of scattered photons one can extract both degree and angle of photon linear polarization. Two scintillator detectors were additionally mounted at the setup to measure the up-down asymmetry of bremsstrahlung emission. Outgoing electrons were not observed.

Electron spin was rotated within the reaction plane by means of a Wien filter. Fig. 3.14a shows the measured tilt of bremsstrahlung polarization plane as a function of the angle between the electron spin and momentum. In Fig. 3.14b the up-down photon emission asymmetry is presented. As expected, when the electron spin is oriented along the propagation direction, i.e., beam is polarized longitudinally, the radiation intensities up and down are equal, while the transversal polarization of electron beam shows the highest asymmetry.

The observed rotation of the bremsstrahlung polarization indicated the rotation of the electron scattering plane, since the photon polarization angle is defined by the electron acceleration direction. In other words, within the semi-classical picture the trajectory of an electron in central Coulomb potential is not confined to a single plane. This effect occurs due to spin-orbit interaction and can only be observed when electrons reach the distance close to the nucleus and scatter to a large angle. In present work we extended the measurement described above and performed the similar experiment at

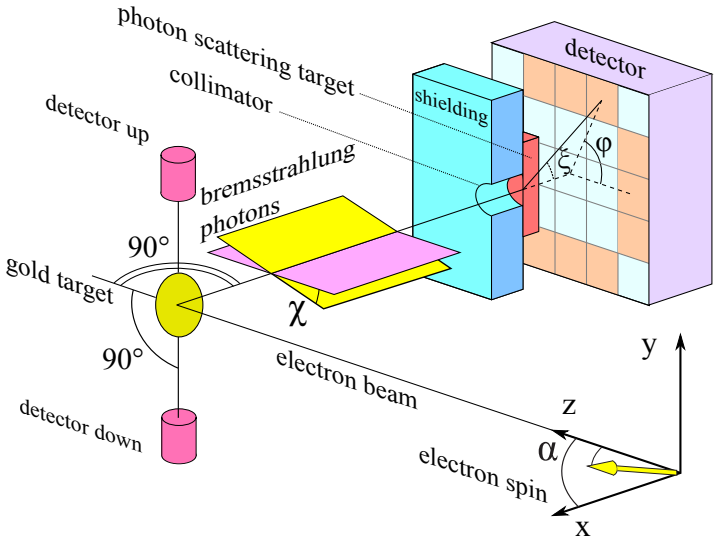

Figure 3.13: Geometry of experimental arrangement [57]. The shielding and the scattering plate are shown in section. Electrons are polarized within the xz plane, polarization angle α is defined with respect to the z axis. Bremsstrahlung polarization plane (yellow) is tilted at angle χ with respect to the reaction plane (pink). Angle ξ is the polar photon scattering angle and φ is the azimuthal scattering angle with respect to the reaction plane. Two scintillator detectors measure the photon emission asymmetry in yz plane.

higher energies.

Recently R. Märtin *et al.* studied the polarization of bremsstrahlung produced by transversely polarized 100 keV electrons [21]. Both the degree and the angle of bremsstrahlung polarization were measured as the function of the photon energy. This allowed for the determination of Stokes parameters $P_1(1,0,0)$ and $P_2(1,0,0)$, which corresponded to the coefficients C_{13} and C_{11} in terminology of Tseng and Pratt. The emitted x rays were detected with a position sensitive Si(Li) Compton polarimeter placed at 130° with respect to the electron beam propagation direction. The experiment revealed the increased tilt angle of the bremsstrahlung polarization plane as compared to the studies performed by Tashenov [57]. The stronger rotation of the photon polarization was due to the different observation angle, which in this energy range corresponds to the electron scattering angle, since electrons emit bremsstrahlung predominantly in the

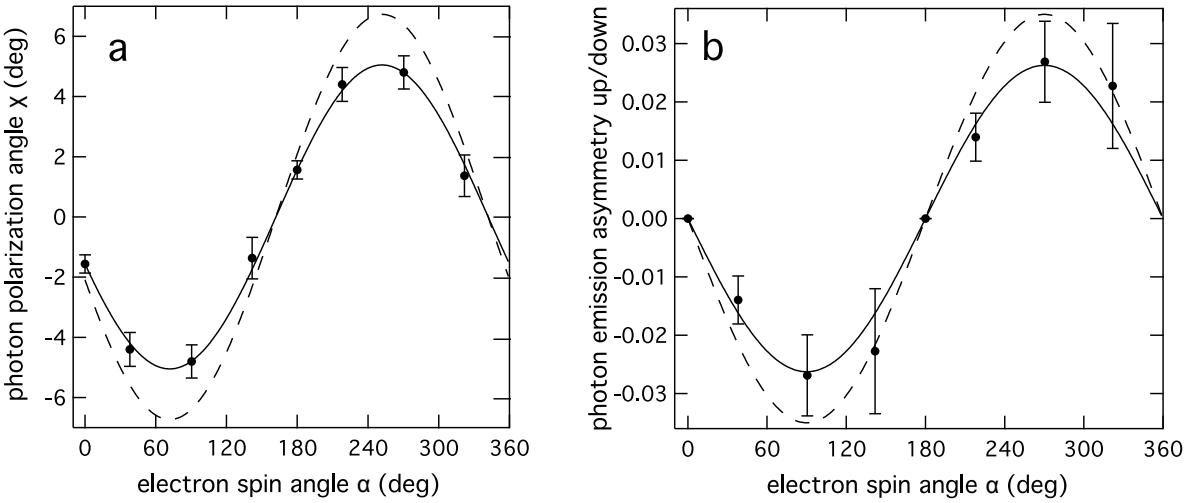

Figure 3.14: Measured tilt angle of bremsstrahlung polarization (a) and up-down photon emission asymmetry (b) as functions of the angle of electron beam polarization [57]. Solid lines denote theoretical predictions for 75% electron beam polarization and dashed lines represent those for 100% polarized beam [24].

forward direction. Therefore, the measured photons were produced by the electrons that reached closer distances to the nucleus, where the Coulomb field is stronger and the effect of the spin-orbit interaction is more pronounced. The experimental results for both the degree and the angle of the bremsstrahlung polarization are presented in Fig. 3.15.

Experiments on measurement the polarization correlations including the observation of outgoing electrons have never been performed. However, the setup for such an experiment is currently being developed by our group.

3.3 Further bremsstrahlung processes

3.3.1 Electron - electron bremsstrahlung

The electron-electron bremsstrahlung is a process of a photon emission under the collision of two electrons. Unlike the ordinary bremsstrahlung where the target nucleus can

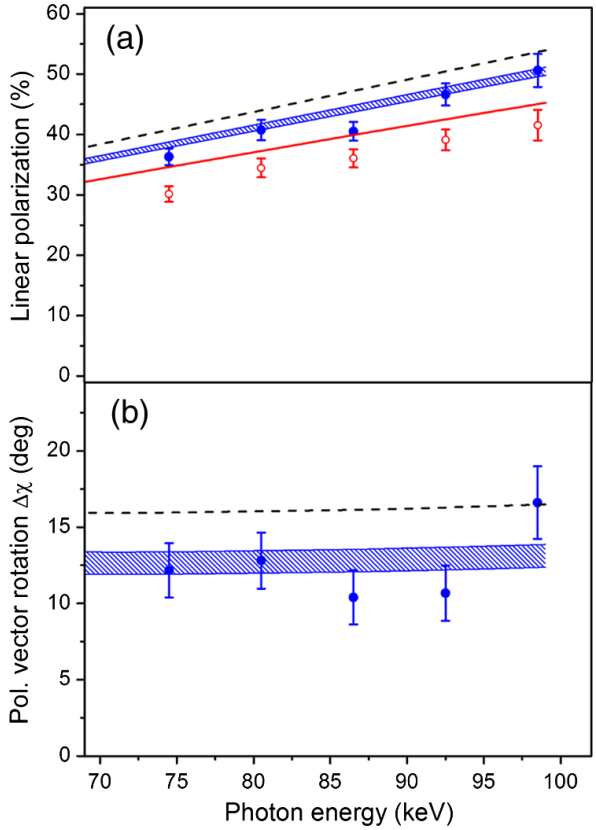

Figure 3.15: (a) Degree of bremsstrahlung polarization produced by transversely polarized (blue) and unpolarized (red) electrons in comparison to theory (shaded area, red and dashed lines) [21]. (b) Tilt angle of bremsstrahlung polarization with respect to the reaction plane. The degree of beam polarization was measured to be $76\% \pm 5\%$. Dashed lines stand for the theoretical calculations for completely polarized electron beam.

be represented by a central Coulomb potential, in the e-e case the recoiling electron has a significant influence on the process and can no longer be considered as an external field. The kinematics of the e-e bremsstrahlung is shown in Fig. 3.16.

In the description of the e-e bremsstrahlung the initial electron momenta are represented as four dimensional vectors $\underline{p_1} = (\epsilon_1, \boldsymbol{p_1})$ and $\underline{p_2} = (\epsilon_2, \boldsymbol{p_2})$. The emitted photon is characterized by the vector $\underline{k} = (k, \boldsymbol{k})$ and the outgoing electrons have the four-momenta $\underline{p_1'} = (\epsilon_1', \boldsymbol{p_1'})$ and $\underline{p_2'} = (\epsilon_2', \boldsymbol{p_2'})$. According to the momentum conservation

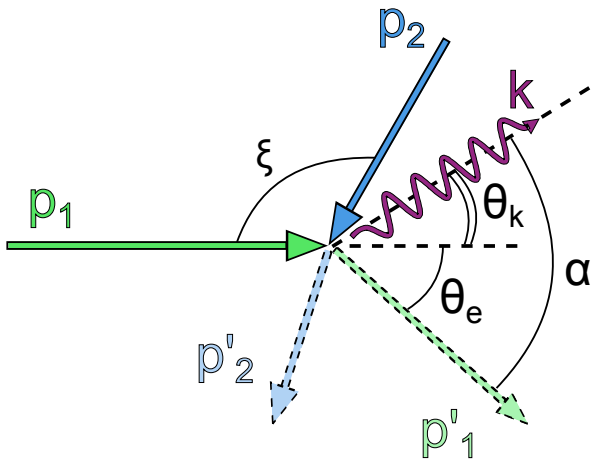

Figure 3.16: Geometry of the electron-electron bremsstrahlung. $\boldsymbol{p_1}$ and $\boldsymbol{p_2}$ denote the initial electron momenta and $\boldsymbol{k}$ stands for the momentum of emitted photon.

law, the following statement can be written:

$$\underline{p_1} + \underline{p_2} = \underline{k} + \underline{p_1'} + \underline{p_2'}. \tag{3.42}$$

Considering the e-e bremsstrahlung in a laboratory frame (the rest frame of the second electron before the collision), where the upcoming electron moves along the z axis and the photon is emitted in the xz plane, the relation for the maximum photon energy for the fixed direction of outgoing electron can be derived [100]:

$$k_{max} = \frac{\epsilon_1 - 1}{\epsilon_1 - p_1 \cos\theta_k + 1} \tag{3.43}$$

It is visible from the Eq. 3.43, that unlike the electron-nucleus bremsstrahlung, the photon energy is dependent on the emission angle. The most energetic photons are emitted at the forward angles. In the non-relativistic regime the spectrum cut-off appears at approximately half of the kinetic energy of the incoming electron, whereas in the relativistic case an electron can transfer nearly all its energy to the emitted x ray [58].

In the electron-matter interaction e-e bremsstrahlung originates from the collisions

of the incoming and bound electrons. However, its contribution to the total x-ray emission is rather small, since the cross section of e-e bremsstrahlung is proportional to the target atomic number Z, while in the electron-nucleus interaction it is proportional to Z^2. If consider the target electron unbound and at rest (laboratory frame), the e-e bremsstrahlung cross section can be expressed as [100]:

$$\frac{d^3\sigma}{dk\, d\Omega_k\, d\Omega_{p_1'}} = \frac{\alpha r_0^2}{\pi^2}\frac{k}{p_1 R}\sum_{i=1}^{2} p_{1i}^2\, A\, p_{1i}', \tag{3.44}$$

where p_{1i} stand for the momenta of outgoing electrons for the fixed photon emission direction $\boldsymbol{k}$, A is the square of matrix element integrated over spins of incoming and outgoing electrons and the term R has the form:

$$R = \sqrt{((\epsilon_1+1)(1-k)+kp_1\,\cos\theta_k)^2 + (p_1\,\cos\theta_e - k\,\cos\alpha)^2 - (\epsilon_1 - k + 1)^2}. \tag{3.45}$$

The Eq. 3.44 is valid only for the cases of free electrons. The correction factors for bremsstrahlung from bound target electrons have been derived in a number of works [101, 102]. The relation for angular distribution can be obtained by integrating the Eq. 3.44 over photon energy k.

Experimental studies of e-e bremsstrahlung based on the coincidental detection of the emitted photons with the outgoing electrons of a fixed energy and direction were performed in [103–105]. In such measurements the photons from e-e bremsstrahlung have less energy that the ones from electron-nucleus bremsstrahlung and, therefore, they are easily distinguishable, as seen in Fig. 3.17a. It occurs due to the non-zero recoil energy of the target electron. In Fig. 3.17b the measured angular distribution is shown [104].

The four lobes in angular distribution can be understood from the fact, that the electric dipole moment of the electron-electron system is zero, and therefore e-e bremsstrahlung radiation consists predominantly of quadrupole radiation.

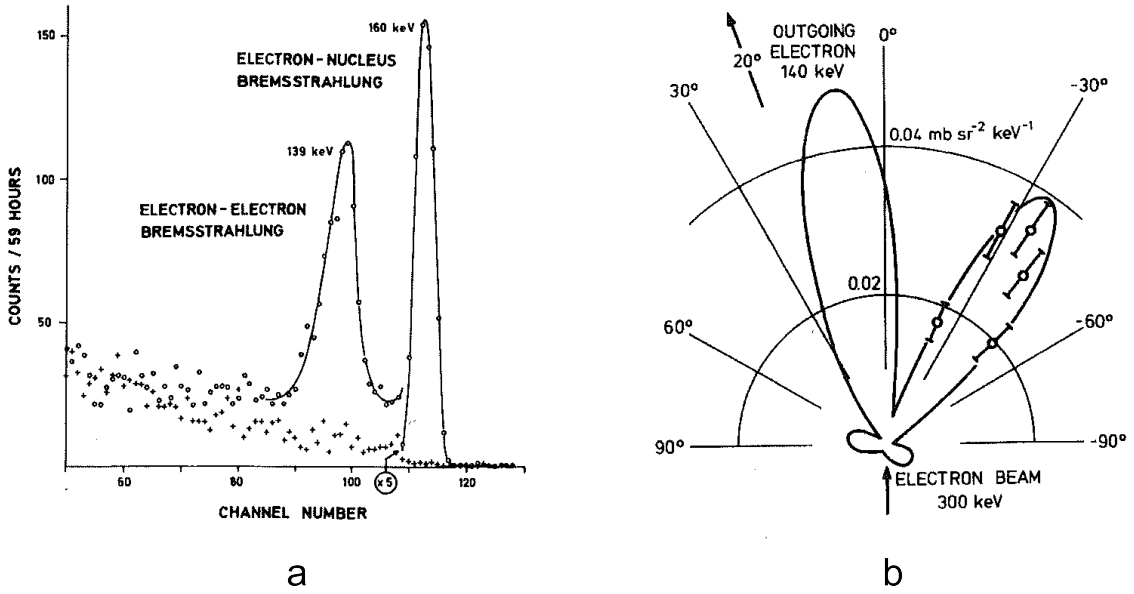

Figure 3.17: Measured at $\theta_k = -35°$ coincident spectrum (a) and the angular distribution (b) of e-e bremsstrahlung from the collision of the 300 kev electron beam with the thin carbon target (Z = 6) [104]. Emitted photons were detected in coincidence with outgoing electrons with the energy $\epsilon_1' =$ 140 keV and scattering angle $\theta_e = 20°$. Crosses in (a) denote random coincidences and the solid line in (b) gives theoretical predictions by Mack [106].

3.3.2 Polarization bremsstrahlung

Polarization bremsstrahlung (PB) arises due to the excitation (polarization) of a target atom by the incident charged particle. The radiation results from a change in the electric dipole moment of the system caused by the upcoming charge (see Fig. 3.18). The ability of a light particle to ionize the target atom is in general similar to the heavy one. This makes the intensity of polarization bremsstrahlung almost independent of the incident projectile mass, whereas the ordinary bremsstrahlung cross section is inversely proportional to it. The x-ray emission intensity in PB is determined mainly by the dynamical polarizability of a target, and an upcoming particle can be simply considered as a moving source of the Coulomb field exciting the target electrons [58, 107].

The phenomenon of polarization bremsstrahlung was first introduced in 1970s when

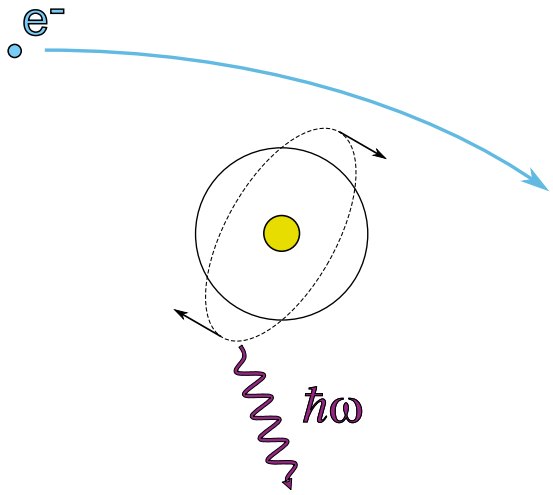

Figure 3.18: Scheme of the polarization bremsstrahlung process. Incoming electron causes the polarization of the target, which returns to the initial state by a photon emission.

it was demonstrated that a dynamic response of the target should be taken into account when calculating the total bremsstrahlung spectrum [108, 109]. It indicates the many-body nature of the PB which makes the process more complicated for theoretical analysis.

Two main theoretical approaches have been used in the PB description. The first formalism is based on the Born approximation [110, 111]. It gives reasonable predictions for both relativistic and non-relativistic energy regions. A more accurate method utilizes the distorted partial wave approximation [112, 113]. The total bremsstrahlung rate $d\sigma_{tot} = d\sigma_{ordin} + d\sigma_{polariz}$ can be estimated within the so called "stripping" approximation, which is based on the assumption that with the increase of the photon energy the reduced intensity of the ordinary bremsstrahlung is compensated by the additional polarization radiation [114, 115]. Fig. 3.19a illustrates the theoretical predictions for bremsstrahlung cross sections obtained with the upper-mentioned approximations [116].

Experimentally PB was observed in two cases where its intensity dominates over the ordinary bremsstrahlung. The first case corresponds to the photon energy region near the ionization potentials of atomic subshells [118] and the second case is heavy particle

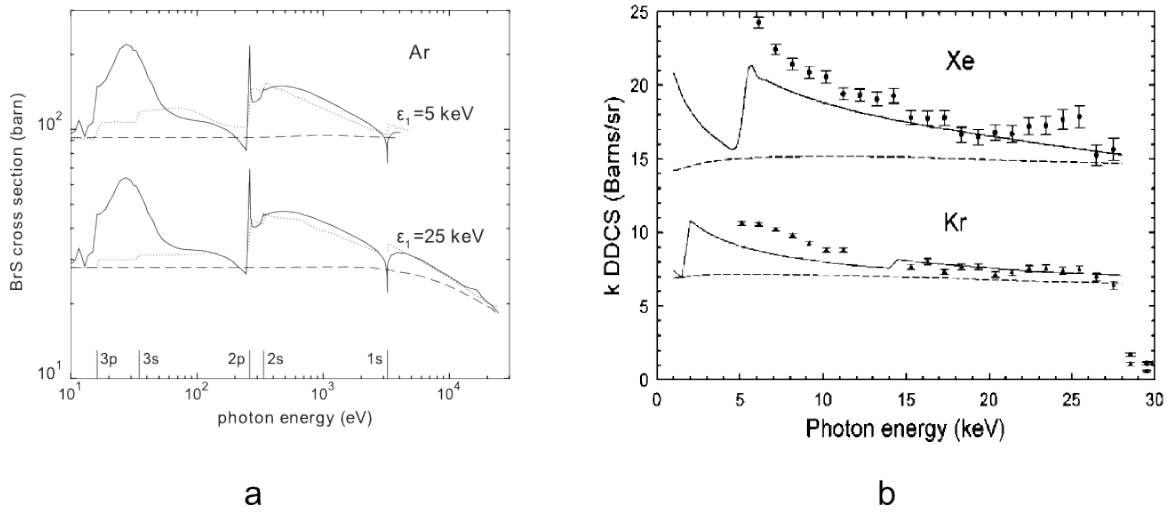

Figure 3.19: (a) Bremsstrahlung spectra calculated for the collision of 5 keV and 25 keV electrons with an Ar atom [116]. Dashed line represents the ordinary bremsstrahlung cross section. Solid and dotted lines describe the total cross section obtained with the distorted partial wave approximation and stripping approximation respectively. Vertical lines denote the ionization potentials of Ar subshells. (b) Product of the photon energy and the bremsstrahlung double-differential cross section for Xe and Kr [117]. The incident electron energy E_e = 28 keV. Solid line is the total cross section in stripping approximation. Dashed line stands for the ordinary bremsstrahlung cross section.

- atom collision, where the ordinary bremsstrahlung is suppressed by the large mass of the incident projectile [119]. Recent experiments on collisions of relativistic electrons with gaseous targets revealed strong discrepancies from ordinary bremsstrahlung theory predictions throughout the spectra (see Fig. 3.19b), which was interpreted as an evidence of the PB contribution [117]. However, even the calculations that include PB don't match with the experimental results perfectly. Several subsequent attempts to improve the agreement between theory and experiment have failed [120, 121].

Chapter 4

The experimental environment

The experiment was performed at the Mainzer Microtron MAMI in the Institut für Kernphysik of Johannes Gutenberg-Universität Mainz, Germany. This facility provides an electron beam with possible energy range from 100 keV to 1.6 GeV.

The MAMI microtron cascade consists of four stages: three racetrack microtrons (RTM) [122] and a harmonic double sided microtron (HDSM) [123], all of them using normal conducting radio-frequency-technology. A 3.5 MeV linear accelerator is used as an injector. The 3.5 MeV electron beam is sufficiently relativistic for injecting into the first RTM. The beam consists of a sequence of electron pulses with 2.45 GHz frequency. Such repetition rate is indistinguishable for most of the particle detectors as their signal bandwidth is smaller.

4.1 Linear accelerator

The linear accelerator Linac consists of three radio frequency sections. In Fig. 4.2 the schematic image of the Linac is presented. In standard operation it produces the 3.5 MeV electrons with a beam current up to 100 μA. The first two RF sections accelerate electrons to 2 MeV. By altering the RF phase in the third section it is possible

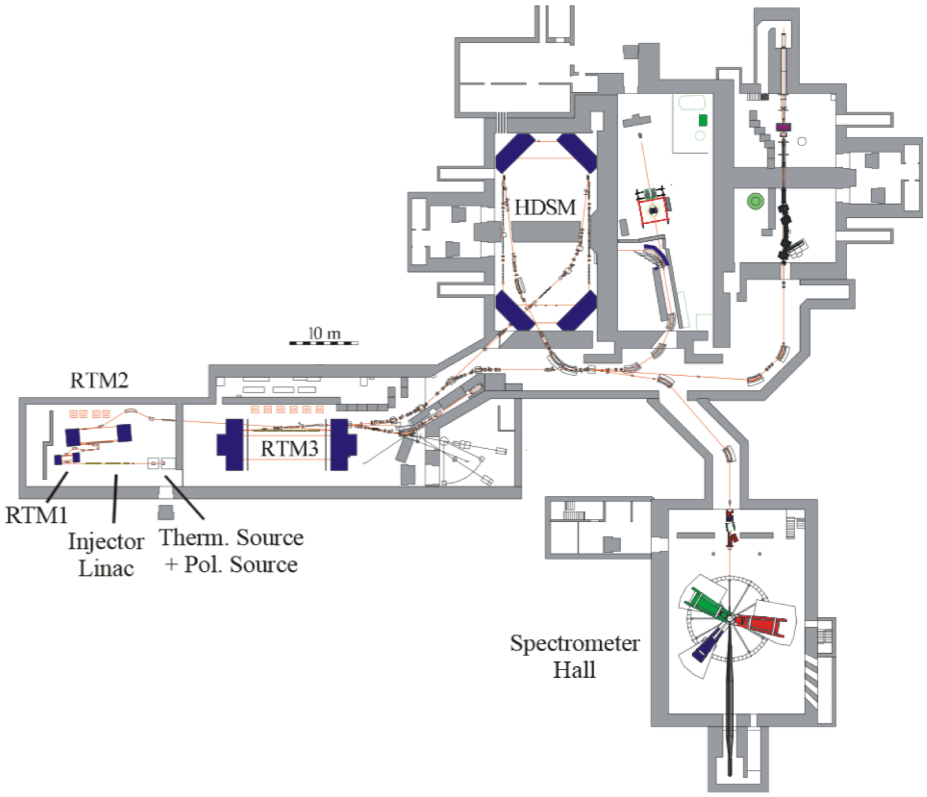

Figure 4.1: Layout of the MAMI facility [124]. The linear accelerator Linac, three racetrack microtrons (RTM), a harmonic double sided microtron (HDSM) and a spectrometer hall.

to reduce or reverse the electron acceleration. Thus, the Linac can provide an electron beam with the energy range between 960 keV and 3.5 MeV. The focusing lenses (not shown in the scheme) consist of solenoids, arranged in counterpouled pairs in order to avoid the rotation of the electron polarization. The standard electron beam diameter is in the range of 1 mm.

The longitudinally polarized 100 keV electron beam is produced by illuminating a GaAsP superlattice strained-layer photo-cathode [126] with circularly polarized laser light with a wavelength of $\lambda = 780\ nm$ [127]. By reversing the laser light polarization with a Pockels cell it is possible to flip the electron spin by 180°. The further electron spin rotation can be implemented with the help of the system based on a

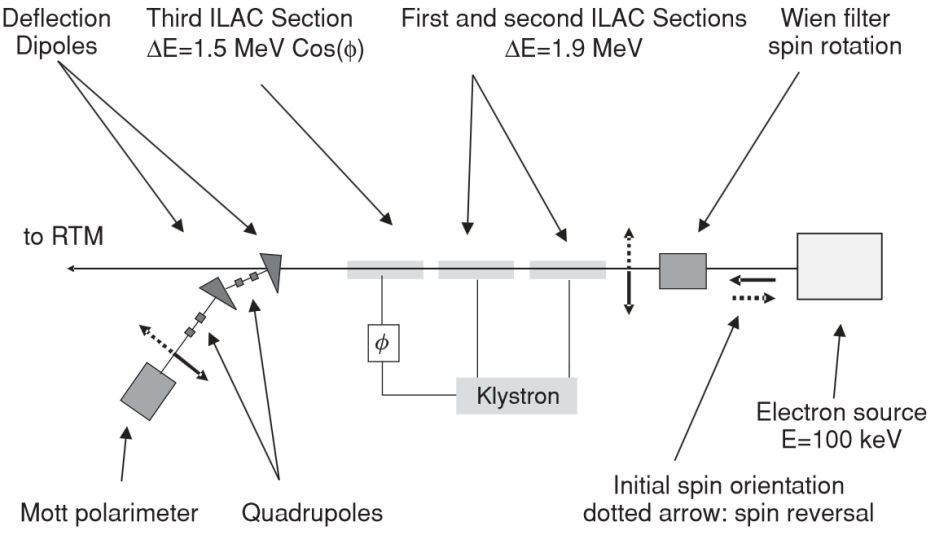

Figure 4.2: The linear acceleration stage of the MAMI facility [125]. A Wien filter, located in front of the Linac, provides the electron spin rotation. For the polarization diagnostics electrons get deflected from the beam to the Mott polarimeter.

Wien filter [128]. The rotation of an electron spin is necessary for the beam polarization diagnostics performed with a Mott polarimeter, since this measurement requires a transversal polarization of the electron beam (see Section 4.2). The first stage of the beam line is shown in Fig. 4.2.

The Wien filter consists of homogeneous electric ($\boldsymbol{E}$) and magnetic ($\boldsymbol{B}$) fields that are orthogonal to one another and to the electron momentum (see Fig. 4.3). An electron moving in the electric field $\boldsymbol{E}$ feels a force $\boldsymbol{F} = e\boldsymbol{E}$. Similarly, moving in the magnetic field $\boldsymbol{B}$ it feels the force $\boldsymbol{F} = e\boldsymbol{v}\boldsymbol{B}$. Thus, in order to avoid the deflection of an electron beam the equilibrium condition has to be fulfilled:

$$\frac{\boldsymbol{E}}{\boldsymbol{B}} = \boldsymbol{v} \tag{4.1}$$

According to the Thomas-Bargmann-Michel-Telegdi equation the electron spin ro-

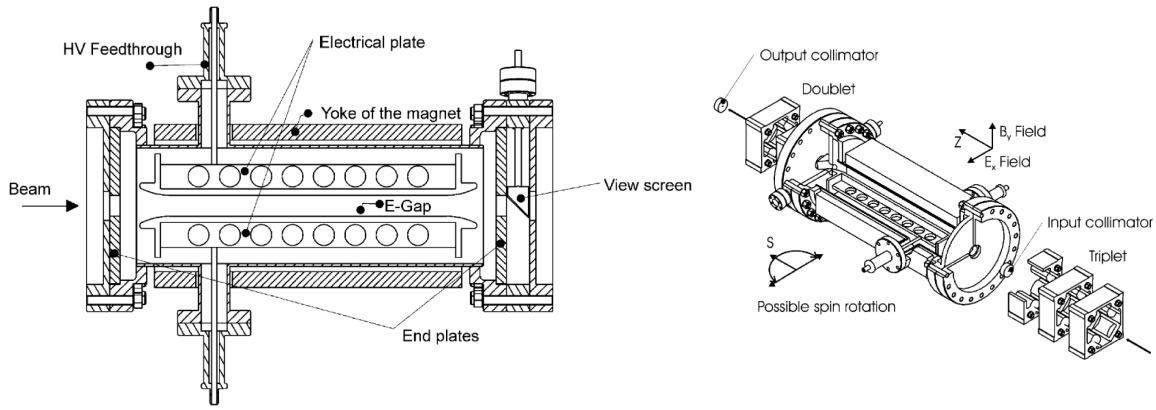

Figure 4.3: Cross section of the Wien filter [128].

tates in the magnetic field and the plane of rotation is perpendicular to $\boldsymbol{B}$:

$$B = \frac{mc\gamma^2\beta\vartheta}{eL}, \tag{4.2}$$

where L is the effective field length and ϑ is the spin rotation angle. In our case to rotate the spin by 90° in the horizontal plane (see Fig. 4.3) the following field parameters are required:

$B_y = 6.563 \times 10^{-3}$ T

$E_x = 1.0788$ MV/m.

The rotation of the spin by $\vartheta = 90°$ causes the negligible (between 0.5% and 3%) beam losses. For the different settings of the spin rotation angle a certain change of the electron beam space ellipse was observed [125]. However, the change of the electron beam profile does not affect the main beam parameters. Additionally, the distortion of the electron beam space ellipse can be compensated by adjusting the quadrupoles shown in Fig. 4.3.

4.2 Mott polarimeter

The Mott polarimeter is used to analyze the degree of the electron beam polarization after the first acceleration stage (see Fig 4.2) [125]. For the polarization measurement the electrons are deflected from the beam line by a magnet system consisting of two 15° bending dipoles and a set of focusing quadrupoles. The Mott scattering asymmetry is measured using a number of gold targets of different thicknesses from 0.1 to 15 μm. Interpolating the measured data to zero target thickness allows to suppress the effects of multiple scatterings. Two plastic scintillator register the backscattered electrons at the angles $\theta = \pm 164°$ with respect to the beam propagation direction. Fig. 4.4 shows the geometry of the Mott polarimeter.

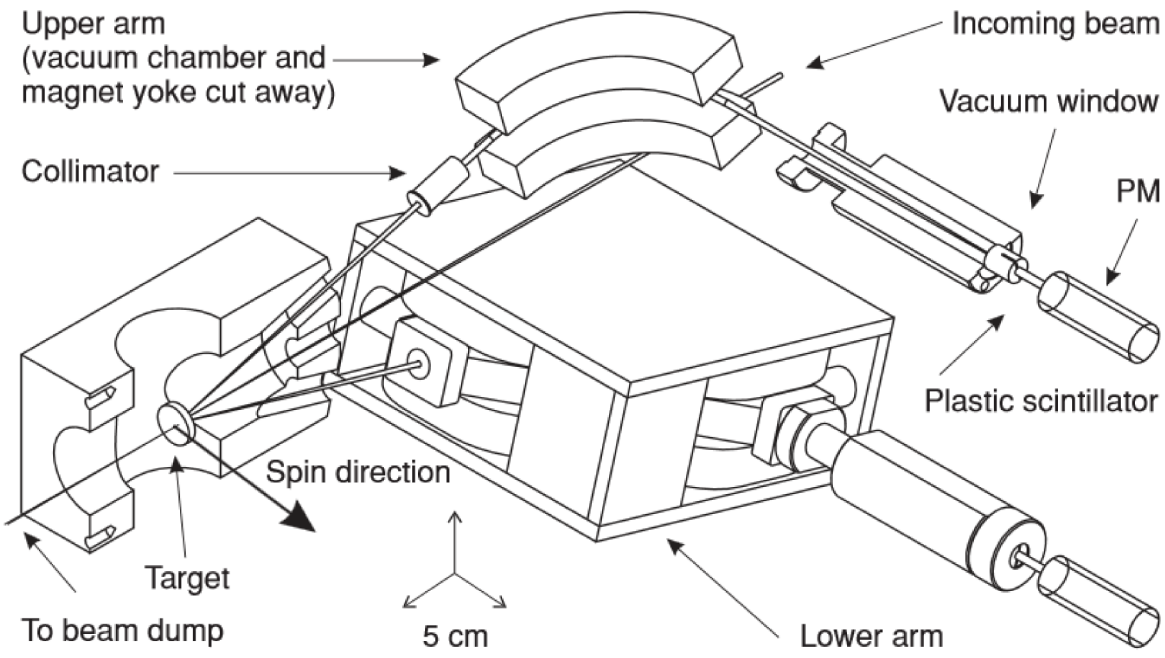

Figure 4.4: View of the Mott polarimeter [125]. Electrons scattered on a gold target at angles $\theta = \pm 164°$ are guided towards the scintillator detectors by two identical double magnet systems. The upper magnet is shown in section for a better visibility.

Mott scattering is sensitive only to the spin component normal to the scattering

plane. Due to technical reasons it is simpler to rotate the electron spin within the horizontal plane, therefore the Mott asymmetry is measured in the vertical plane. The detectors do not directly observe the scattering target. The backscattered electrons pass through the 4 mm aluminum collimators and then are guided through the double focusing spectrometer magnets. Such geometry allows to shield the detectors from the unwanted x rays, produced by electrons that are scattered to the chamber walls as well as from the background from the beam dump.

The scattering asymmetry is defined as:

$$A_{exp} = \frac{R_1 - R_2}{R_1 + R_2}, \tag{4.3}$$

where R_1 and R_2 are the count rates in top and bottom detectors. For the more precise determination of the beam polarization the measurement is performed for two electron spin orientations ($\vartheta = \pm 90^\circ$ with respect to the electron momentum). The spin flips repeatedly every second and after each flip the count rate in both detectors is measured. The experimental asymmetry is then calculated as:

$$A_{exp} = \frac{1 - \sqrt{Q}}{1 + \sqrt{Q}}, \tag{4.4}$$

where $Q = (R_1^+ R_2^-)/(R_1^- R_2^+)$ (see ref. [129] for details). Indexes "+" and "-" denote two electron spin orientations. Such count rate normalization allows to suppress the systematic effects caused by the possible geometrical misalignment of the detectors, as well as by the differences in detection efficiencies.

The degree of electron beam polarization S is correlated to the measured asymmetry A_{exp} as:

$$S = \frac{A_{exp}}{S_{eff}}, \tag{4.5}$$

where S_{eff} is the effective value of Sherman function (effective analyzing power), which depends on the scattering angle θ, beam energy E and on the Z of the scattering

material. The results of theoretical calculations of Sherman function for gold scattering target (Z = 79) are shown in Fig. 4.5.

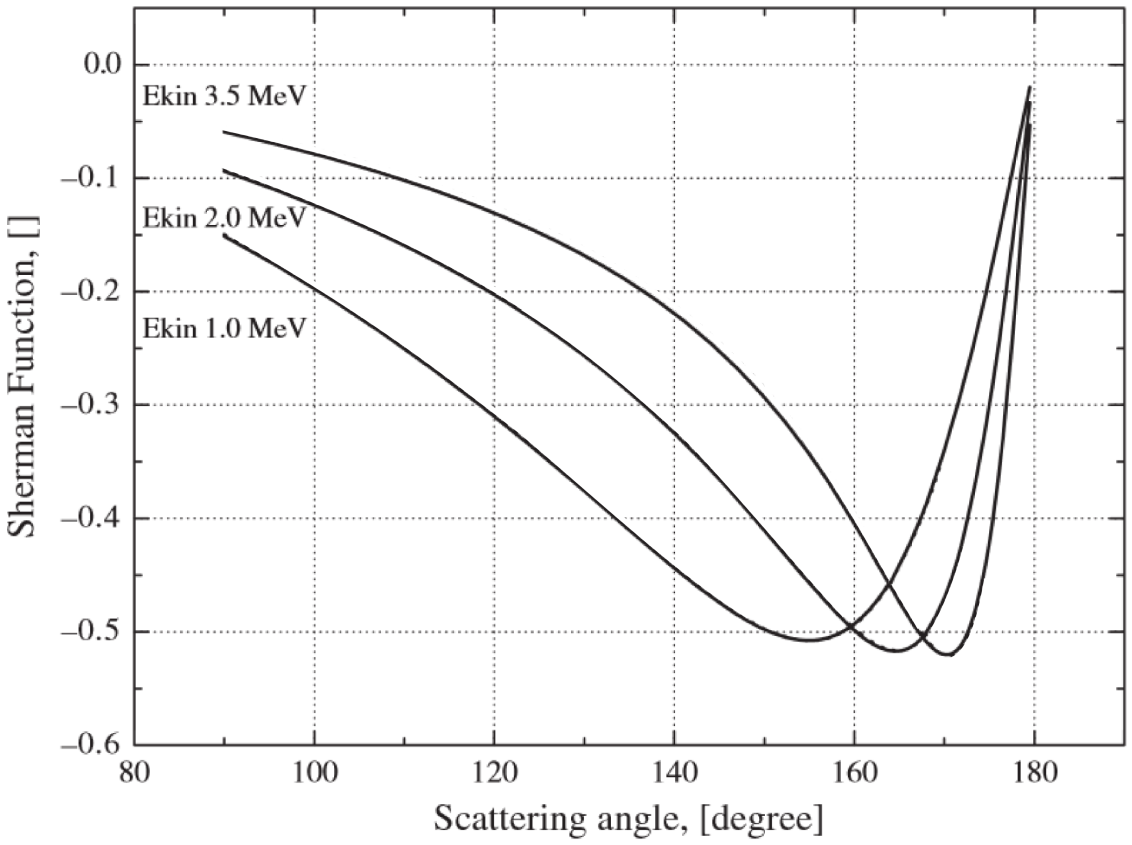

Figure 4.5: Dependence of the Sherman function on beam energy E_{kin} and scattering angle θ [125].

The Mott polarimeter operating at Mainzer Microtron is capable of determining the degree of electron beam polarization with precision of ∼1% for almost all achievable beam intensities. Unlike most polarimeters which typically designed for keV energy range, it is able to work with energies up to several MeV without compromising the accuracy. This unique ability makes it perfectly suitable for the MAMI facility.

4.3 Measurement of the bremsstrahlung polarization

The experimental study for the linear polarization of bremsstrahlung was performed in March 2013 at the Mainzer Microtron MAMI in the Institut für Kernphysik of Johannes Gutenberg-Universität Mainz, Germany. Polarized electrons were produced by illuminating a GaAsP superlattice strained-layer photo-cathode with circularly polarized laser light. The electron beam was accelerated to 2.15 MeV and its degree of polarization was measured to be $S = 0.800 \pm 0.05$ using a Mott scattering polarimeter. The bremsstrahlung polarization was measured for the longitudinally and transversely polarized electrons. The rotation of electron spin within the horizontal plane was performed by using the Wien filter. For each electron beam polarization two measurements with the opposite orientations of the electron spin were taken (collinear and anti-collinear to the electron beam in case of the longitudinal polarization and right and left to the electron beam in case of the transversal). The spin flip was produced by changing the helicity of circular polarization of the laser light and did not affect any other experimental parameters, such as the electron beam energy, current, trajectory or degree of polarization. The bremsstrahlung photons were produced in collisions of electrons with a 500 nm gold foil target. We chose gold because of its high atomic number (Z = 79) which provides the high photon emission intensity. For this reason it has been widely used in both theoretical and experimental bremsstrahlung studies including the recent measurements of the polarization correlations [20, 21, 57]. The geometry of the measurement is shown in Fig. 4.6. To register the emitted photons the position sensitive high purity planar germanium detector was used. The detector was shielded from the unwanted x rays by 10 cm lead walls. A round opening in the shielding collimated the bremsstrahlung photons emitted in the at the angle of $90^\circ \pm 5^\circ$ with respect to the electron beam propagation direction. Before entering the detector

the photons left the vacuum system through the stainless steel vacuum flange. Electrons that elastically scattered in the gold target and hit the vacuum flange produced the background bremsstrahlung. The 5 mm thick beryllium plate (Z = 4) inserted in a cavity drilled in the stainless steel allowed to reduce such background by a factor of 43. A 2 cm layer of lead between the target and the detector allowed to cut out the low energy photons and limited the count rate.

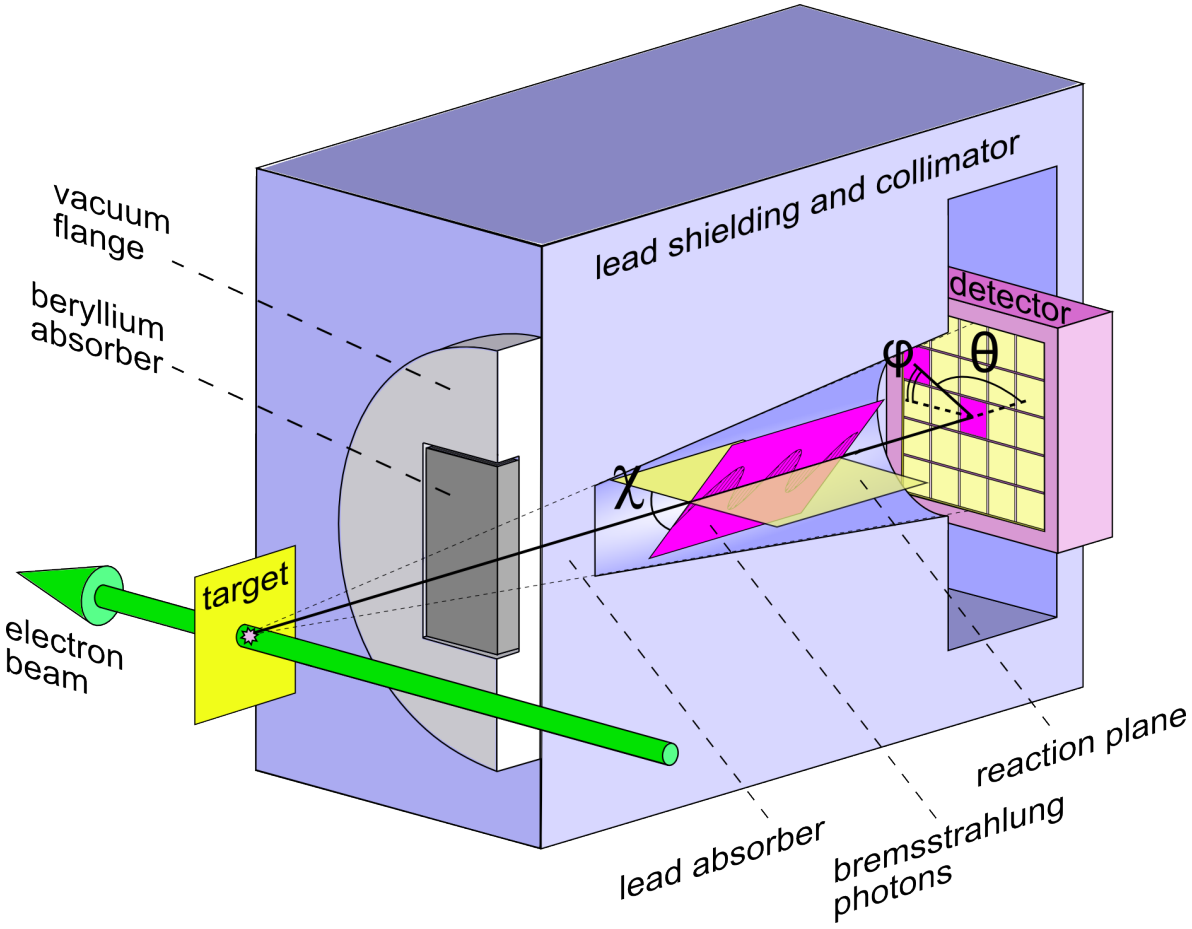

Figure 4.6: The scheme of the experiment. The reaction plane (yellow) is defined by the incoming electron and the emitted photon directions. The bremsstrahlung polarization plane (red) is tilted by an angle χ with respect to the reaction plane. The azimuthal photon scattering angle is denoted by φ and the polar angle - by θ. The vacuum flange, beryllium plate and lead shielding are shown in section for a better visibility.

The detector was placed at 26.7 cm from the target perpendicular to the collimated photon beam and its center was aligned with the photon beam axis. The germanium crystal was 5x5x2 cm in size and its front side (cathode) was electrically segmented into 5x5 matrix of square pixels (see Fig. 4.7). The back side of crystal had a not segmented lithium drifted anode. Each segment was equipped with an individual charge sensitive

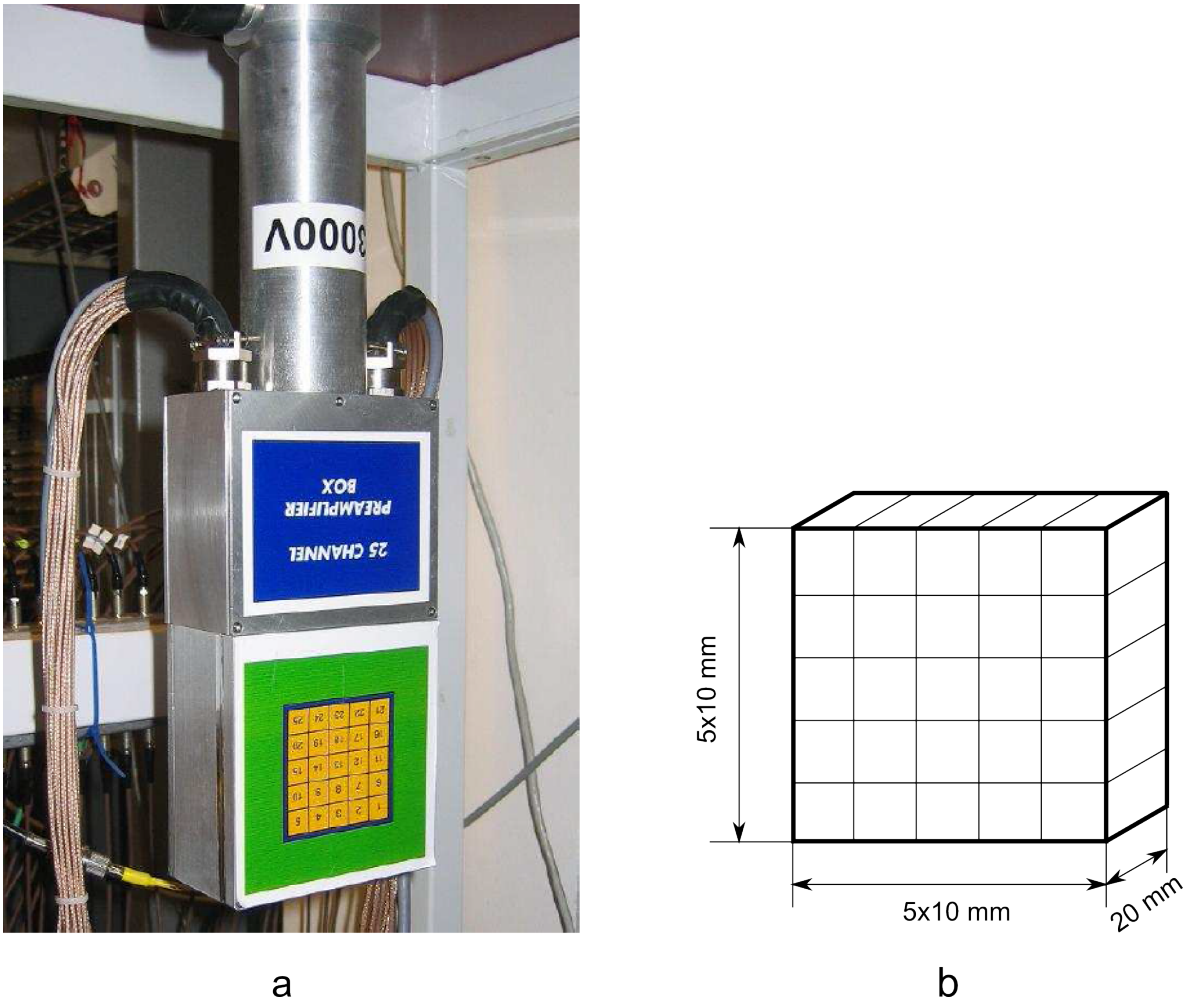

Figure 4.7: The planar pixelated HPGe detector. (a) - the box with preamplifiers is attached to the detector housing; (b) - schematic view of the detector crystal segmentation. The size of a single pixel is 1x1x2 cm.

preamplifier and a 100 MHz sampling analog-to-digital converter. The digitized signals

were processed with a moving window deconvolution algorithm to extract the x-ray energies and the arrival times. The achieved energy resolution was 4 keV at 2 MeV and the timing resolution was 100 ns.

Linear polarization of bremsstrahlung was measured with the Compton polarimetry technique. It is based on the sensitivity of the angular distribution of the Compton scattered photons to their initial polarization through the Klein-Nishina formula (2.6) (see Chapter 2.8 for details). For the analysis we selected the events, where the incoming photons were Compton scattered in one detector pixel and then photoabsorbed in another. In this case the first segment measures the energy of the Compton-recoiled electron E_e and the second segment registers the scattered x ray $\hbar\omega'$. These energy depositions were detected in time-coincidences and their sum was equal to the energy of the incoming x ray: $E_e + \hbar\omega' = \hbar\omega$. Thus, knowing the energies of interactions and their positions the whole Compton event could be reconstructed.

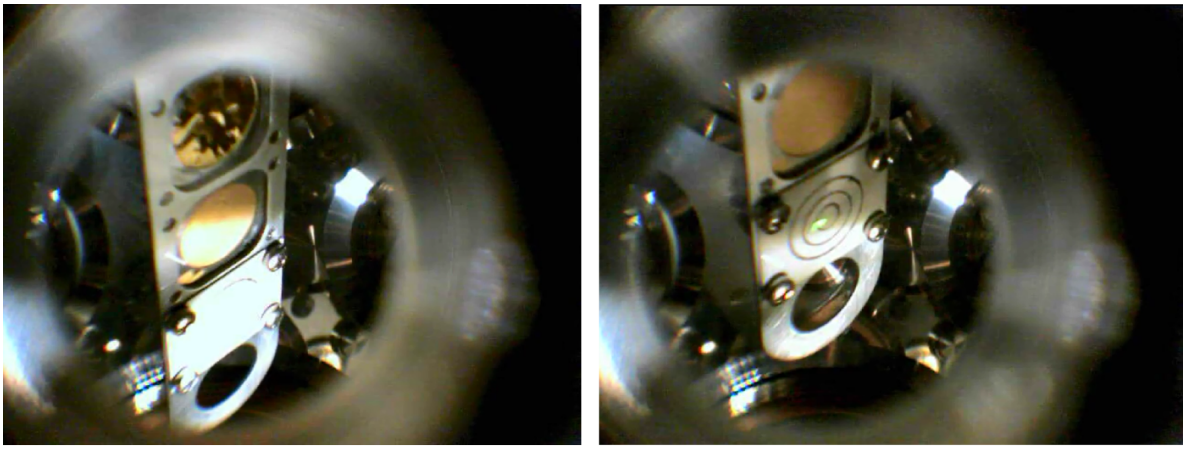

Figure 4.8: View of the target holder in the vacuum chamber. The image is taken by a web camera attached to one of the chamber windows; a - from top to bottom: 2 μm, 500 nm, scintillator plate, 14 mm whole; b - electron beam profile on the scintillator plate.

The target holder had three slots for different targets and a round 14 mm hole to check the spreading of an electron beam (see Fig. 4.8). It could be moved by a

manipulator. On the first two slots we installed two gold foil targets of 500 nm and 2 μm thick. The latter was a spare one in case the thinner targets got broken or damaged during the experiment. To observe the beam profile on the third slot the scintillator plate was installed (see Fig. 4.8b). For the more thorough diagnostics of the electron beam spreading the 14 mm diameter round hole was used. This test was based on comparing the count rates in the detector when shooting the beam through the 14 mm hole and when the target holder was completely removed from the beam line. The difference in count rates denoted that the beam was not focused enough and needed further adjustment.

Chapter 5

Data analysis

5.1 Pulse shape analysis and Compton imaging

Experiments involving hard x rays are always characterized by the large intensity of the high energy background. However, due to geometrical reasons it is not always possible to arrange a massive shielding of the detector. In this section we demonstrate the algorithm of background suppression using Compton imaging. The precision of this method is mostly defined by the positional resolution of the detector. For our experiment we used a segmented detector with a pixel size of 1×1×2 cm, which was by far not sufficient to effectively apply Compton imaging. With the help of the pulse shape analysis algorithm, developed by A. Khaplanov specifically for our detector, we could significantly increase the spatial resolution. The detailed description of PSA is presented in Section 2.6.

In Fig. 5.1 the signal pattern of the 25 detector pixels for a typical data event is presented. The two highlighted segments contain the charge collection pulses which correspond to energy depositions. A number of induced transient pulses is present in several neighboring pixels. Note that amplitudes of the induced signals are much smaller compared to the charge collection pulses, and therefore were enlarged for a better visibility. The 25 signals from one event were collected in one vector $\bar{S}$ and

fitted with the linear combination (2.10) of the basis pulses simulated for the number of grid points throughout the detector. As a result we got the 3D coordinates for both interactions with the precision of 3 mm.

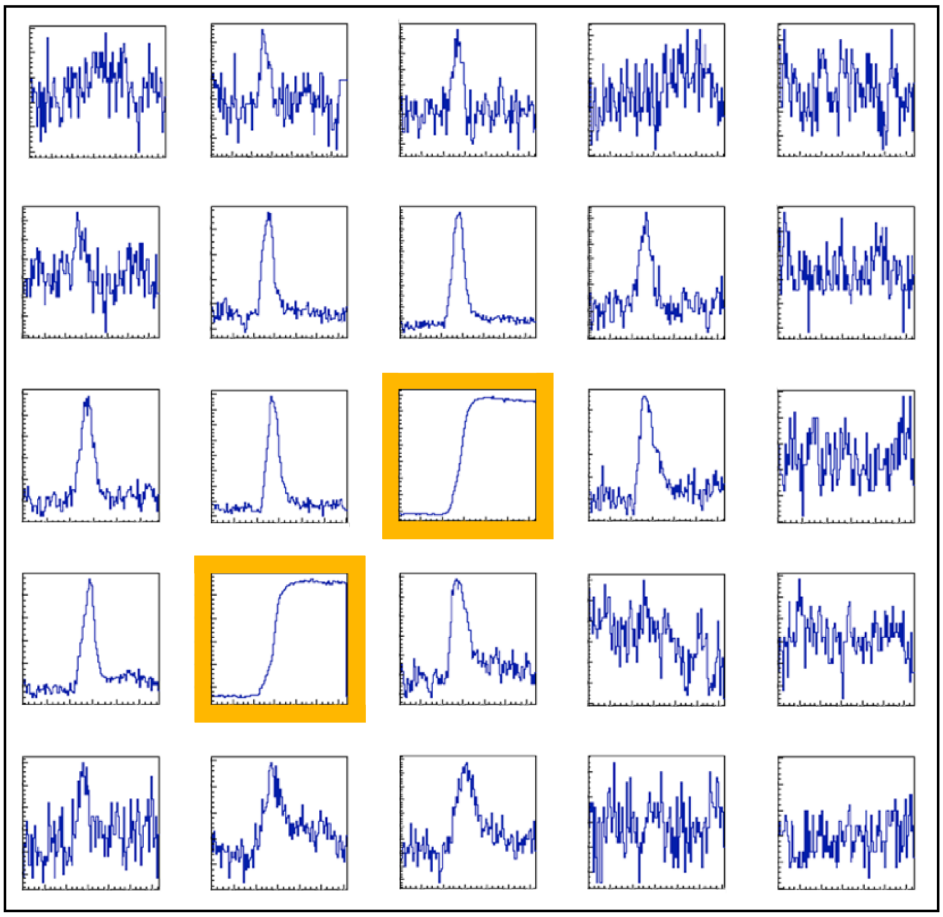

Figure 5.1: Typical signal pattern for a single data event. Two highlighted pulses correspond to the direct energy depositions. The amplitudes of the transient pulses in the remaining segments are enlarged for a better visibility.

All events were treated as a Compton scattering interaction in one segment and the photoabsorbtion in another. We selected the events with the calculated polar scattering angle of $40° < \theta < 85°$. Most of the registered events fell in this interval. Here, a photon transfers most of its energy to the Compton electron and therefore in the image reconstruction the larger of the two energy depositions corresponded to the scattering

point. Knowing the exact positions of interactions the cone of possible directions of incoming photon can be reconstructed (see Fig. 5.2a).

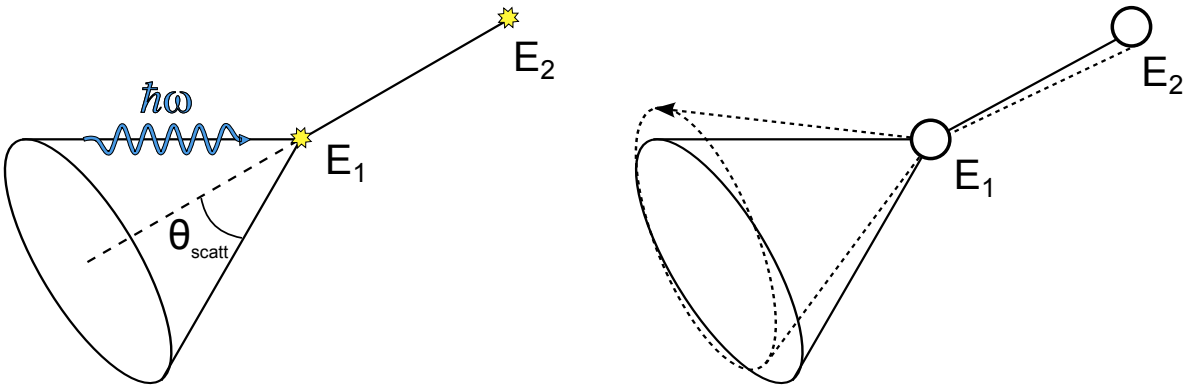

Figure 5.2: The uncertainty of the cone reconstruction due to the finite position resolution.

The polar scattering angle θ_{scatt} was obtained from the energies of the interactions:

$$\cos\theta_{scatt} = 1 - \frac{(\hbar\omega - \hbar\omega')}{\hbar\omega\,\hbar\omega'}mc^2 = 1 - \frac{E_1}{(E_1+E_2)E_2}mc^2. \tag{5.1}$$

The error of 3 mm in determining the absolute location of interaction caused the uncertainty in defining the cone axis, as shown in Fig. 5.2. For the image reconstruction we used the spherical coordinate system with the origin in the middle of the central pixel's surface and z axis pointing inside the detector. The coordinates φ and θ of the possible incoming photon directions were plotted while taking into account the uncertainty in the cone reconstruction. Therefore, instead of an ellipse (as in Fig. 2.16) the back-projection of a cone takes a form of a ring (see Fig. 5.3). The statistical weight of a ring is reversely proportional to the error in defining the cone axis, i.e., the events with the larger distance between the interactions E_1 and E_2 make a larger contribution to a single area unit.

To demonstrate the background suppression algorithm we considered the photon energy of $1.6\ MeV < \hbar\omega < 2.15\ MeV$ since within our experiment we were interested in the tip region of the bremsstrahlung spectrum. In Fig. 5.4 the the example of the

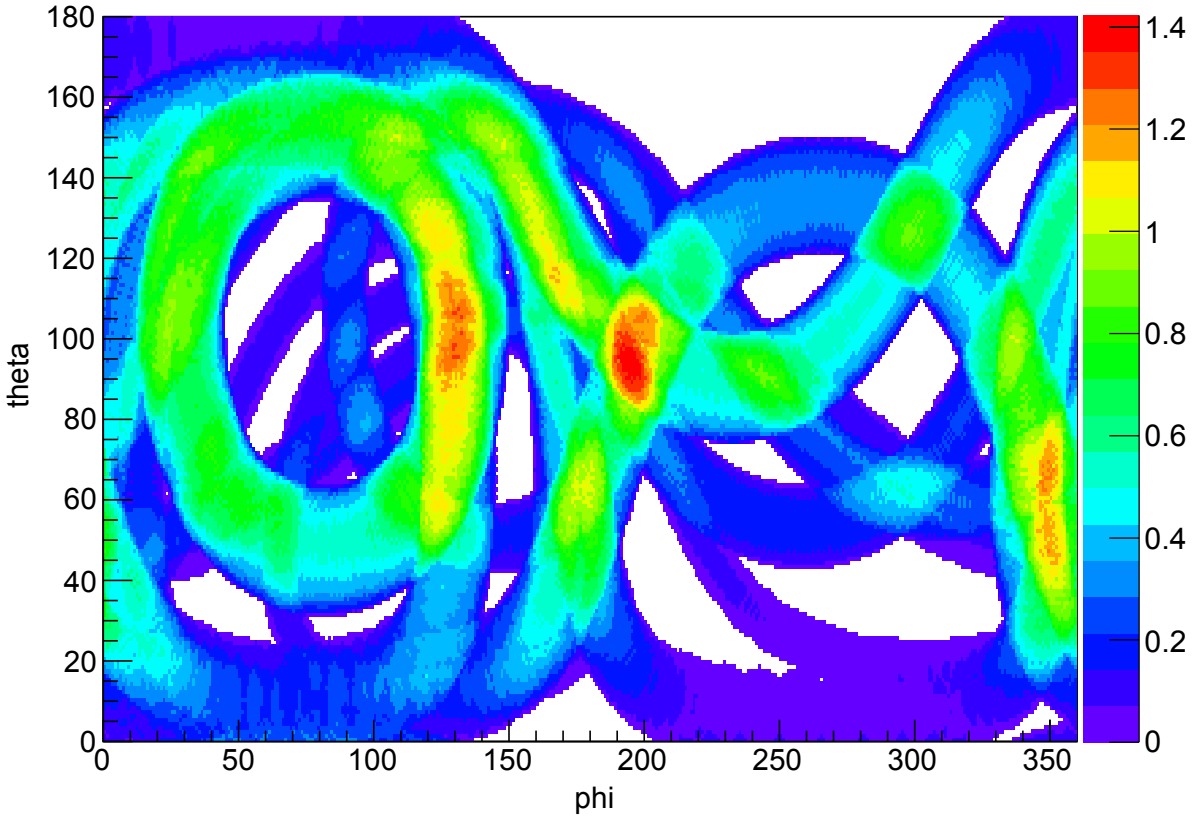

Figure 5.3: Depending on the scattering angle the cone's back-projections have a shape of a ring or a sine. The events with the smaller error in defining the cone axis correspond to the narrower rings.

reconstructed image is shown. The location of the target can be determined by the fitting of the φ and θ distributions with a Gaussian function. We achieved the angular resolution of 10° analyzing the events where the distance between Compton scattering and photoabsorption was larger than 40 mm. Further increase of the minimal distance led to the significant drop of statistics and didn't improve the angular resolution. The spherical coordinates of the target were determined to be (180° ± 10°, 90° ± 10°). Therefore by filtering out the cones which didn't intersect with this area a significant background suppression can be achieved (see Fig. 5.5). This imaging method was used in astrophysics. The COMPTEL telescope on board of CGRO mission used the principles of Compton imaging [130]. A new Compton telescope is planned to be put

on orbit on board of the ASTRO-H satellite.

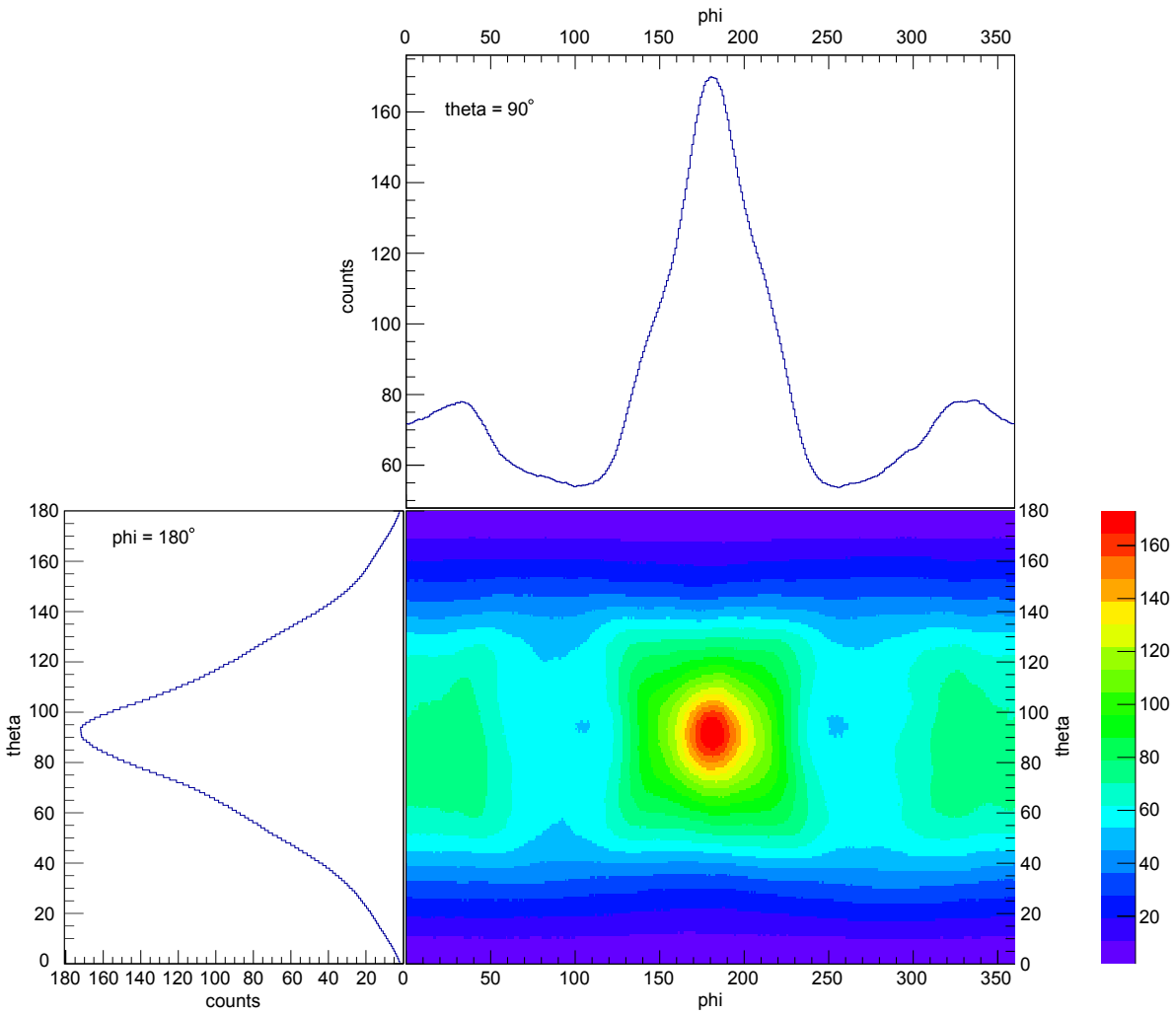

Figure 5.4: Image reconstruction using spherical coordinates of cones back-projections. Photon energy 1.6 $MeV < \hbar\omega < 2.15\ MeV$, distance between energy depositions E_1 and E_2 d = 10 mm. The projections of phi and theta are taken at $\theta = 90°$ and $\varphi = 180°$ respectively.

5.2 Bremsstrahlung polarization

A typical measured spectrum is shown in Fig. 5.6. The low energy photons were suppressed by 2 cm of lead placed between the target and the detector. For the polarization

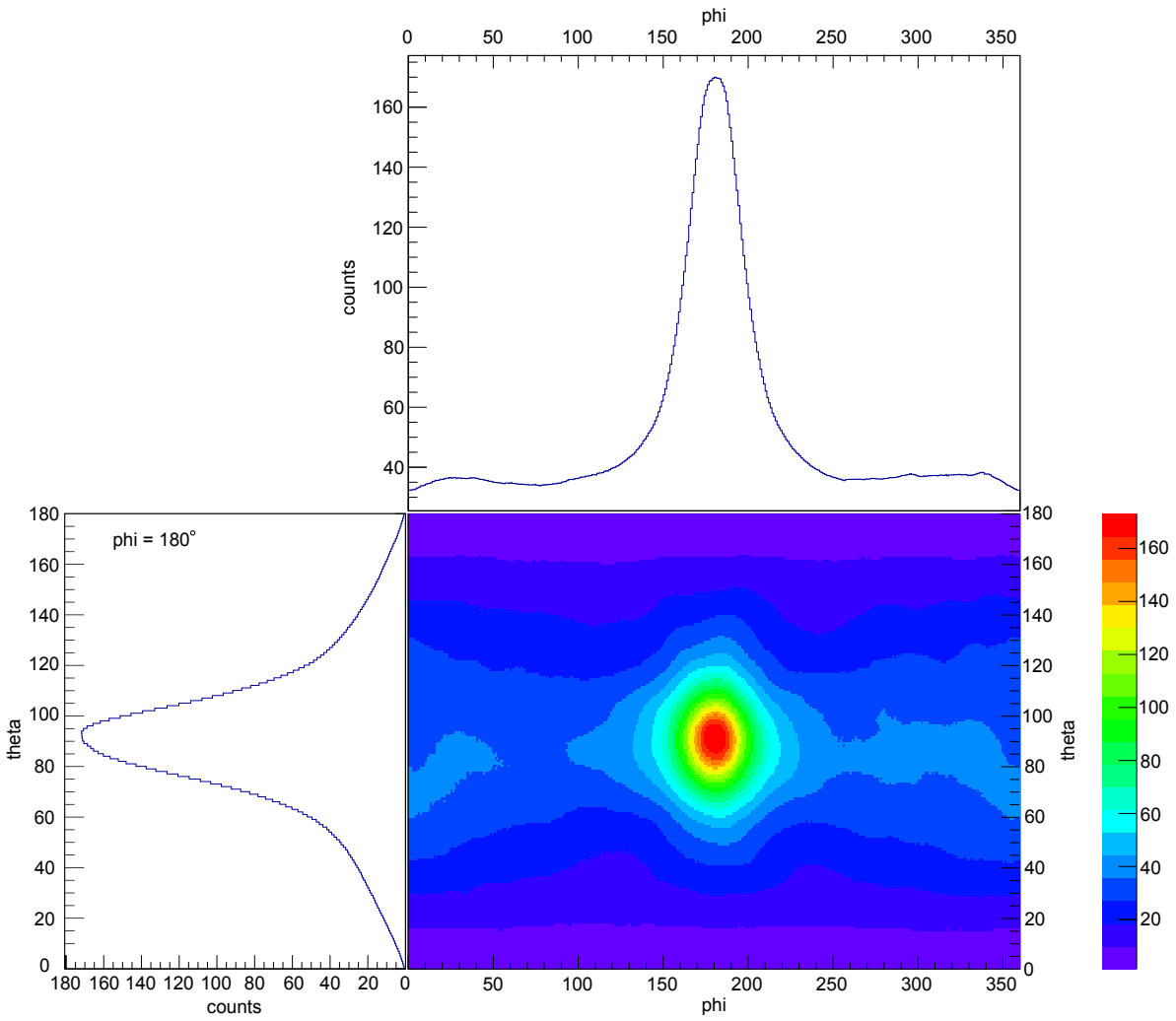

Figure 5.5: Image reconstruction using spherical coordinates of cones back-projections after filtering out the background. Photon energy 1600 $keV < \hbar\omega < 2150$ keV, distance between energy depositions E_1 and E_2 d = 10 mm. The projections of phi and theta are taken at $\theta = 90°$ and $\varphi = 180°$ respectively.

analysis we chose the tip energy region of 1.6 MeV $< \hbar\omega <$ 2.15 MeV. We estimate the background level in this interval to be less than 6%. Most of the unwanted x rays originated from the beryllium plate mounted on a vacuum flange. The emitted background radiation was estimated in the following way. As the electrons penetrate the plate, the penetration depth provides the effective thickness of beryllium as a bremsstrahlung target. The background level was obtained by the summation of the bremsstrahlung

spectra calculated for each such layer. The effective electron energy was obtained using the continuous slowing down approximation as a function of the penetration depth [131].

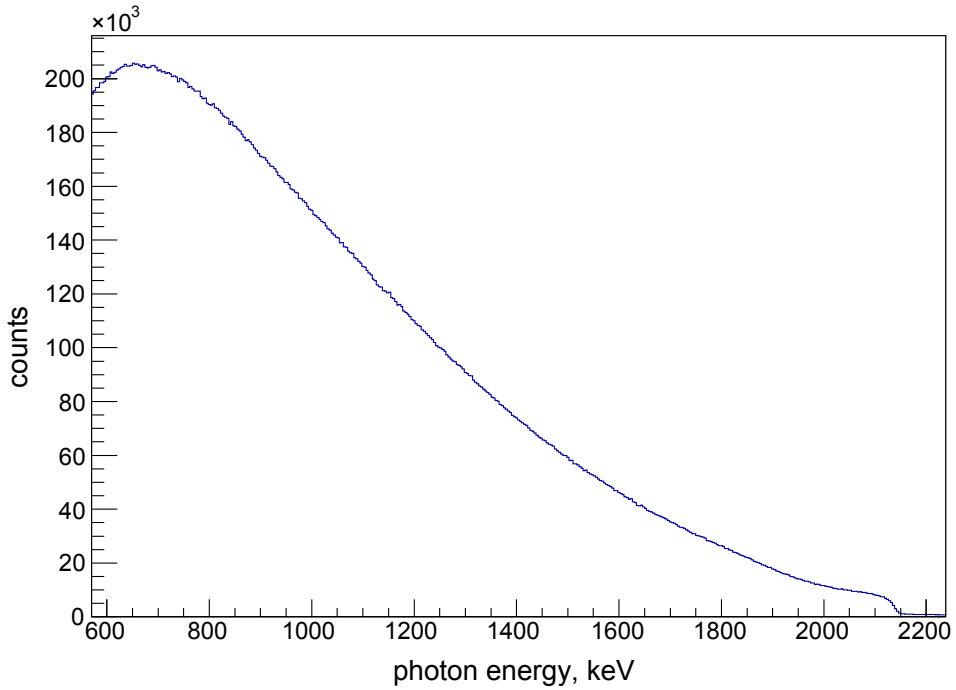

Figure 5.6: Typical bremsstrahlung spectrum measured at anode. Lower energy photons are absorbed by 2 cm led layer.

When a photon is scattered in one detector segment and then photoabsorbed in another, the real time difference between the energy depositions is less than 1 ns. Therefore, with the time resolution of 100 ns provided by our detector, the time order of these interactions was not resolved.

Eq. 5.1 is only valid for the events, where the photon was Compton scattered and then photoabsorbed. In the events where two Compton scatterings took place in two separate segments and the second scattered x ray escaped the detector, the condition $\hbar\omega = E_e + \hbar\omega'$ is not fulfilled and, therefore, the angle θ derived from Eq. 5.1 should give a wrong result. To suppress such events, we limited the interval of the polar scattering angles to $40° < \theta < 85°$. Since in the energy range of 1.6 MeV $< \hbar\omega <$ 2.15 MeV the x

rays scatter predominantly in the forward direction, most of the full energy deposition events fell into this interval. Moreover within these energy and scattering angle intervals the energy of the Compton electron E_e is greater than the energy of the outgoing photon $\hbar\omega'$. Therefore the interaction with greater energy was considered to be the Compton scattering point while the lower energy depositions - to be the photoabsorption.

To analyze the azimuthal distribution of the Compton scattered bremsstrahlung x rays the azimuthal scattering angle φ was defined by the detector's segmentation. To balance the high statistics and the good definition of the angle φ, the events, in which the triggered segments were separated by one segment, were selected for the analysis. The square symmetry of the detector strongly modified the azimuthal scattering angular distribution. A non-uniform illumination of the detector, caused by the finite range of the bremsstrahlung emission angles and the collimation of the detector, further distorted this distribution. In order to compensate for these effects, several normalizations were performed. The number of the events of Compton scattering from any segment i to another segment j, $X[i,j]$, was normalized on the total amount of Compton scattering events in this segment: $I[i,j] = X[i,j]/\sum_j X[i,j]$. Since several combinations of the segments corresponded to the same azimuthal scattering angle φ (see Fig. 5.7a), the weighted averaged scattering intensity $I(\varphi)$ was obtained from the set of the corresponding normalized scattering intensities $I[i,j]$.

To compensate for the solid angle differences between various combinations of the segments, the intensity ratio normalization $J(\varphi) = I(\varphi + 90°)/I(\varphi)$ that exploited the square symmetry of the detector, was implemented [132]. In other words if a photon scatters from a certain pixel i to a pixel j (having a scattering angle φ), there is always a third pixel k having the same relative geometry ($i \to j = i \to k$) but the scattering angle $\varphi + 90°$, as shown in Fig. 5.7b. The raw intensity of scattered photons as well as the one after performing the mentioned normalizations are presented in Fig. 5.8.

The bremsstrahlung linear polarization was measured for the longitudinally and

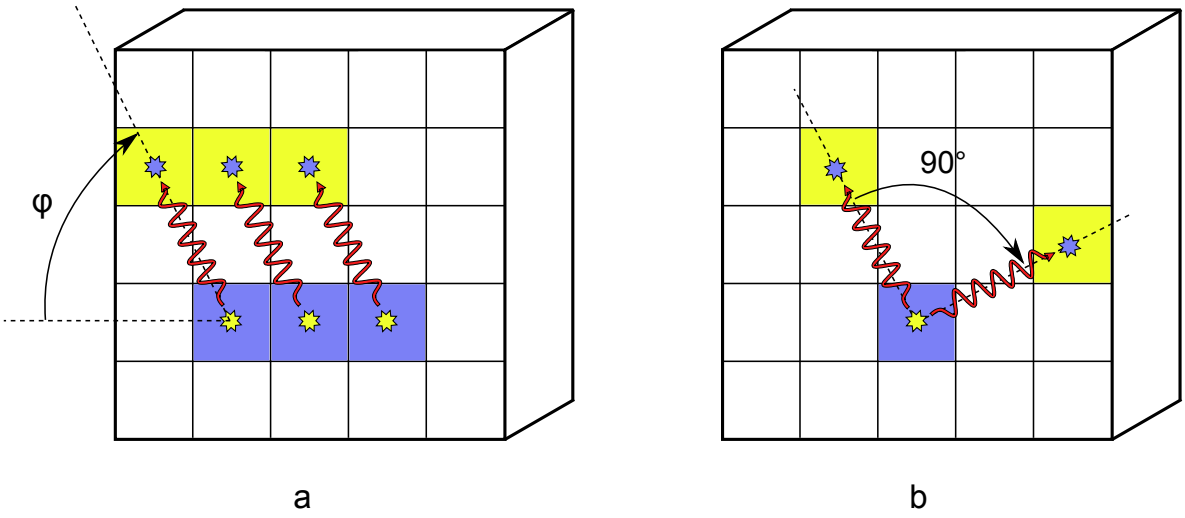

Figure 5.7: (a) Several pixel pairs corresponding to the same azimuthal scattering angle φ. (b) The principle used for the normalization $J(\varphi) = I(\varphi + 90°)/I(\varphi)$. Two scattering directions differ by 90° but the segments have the identical relative geometry.

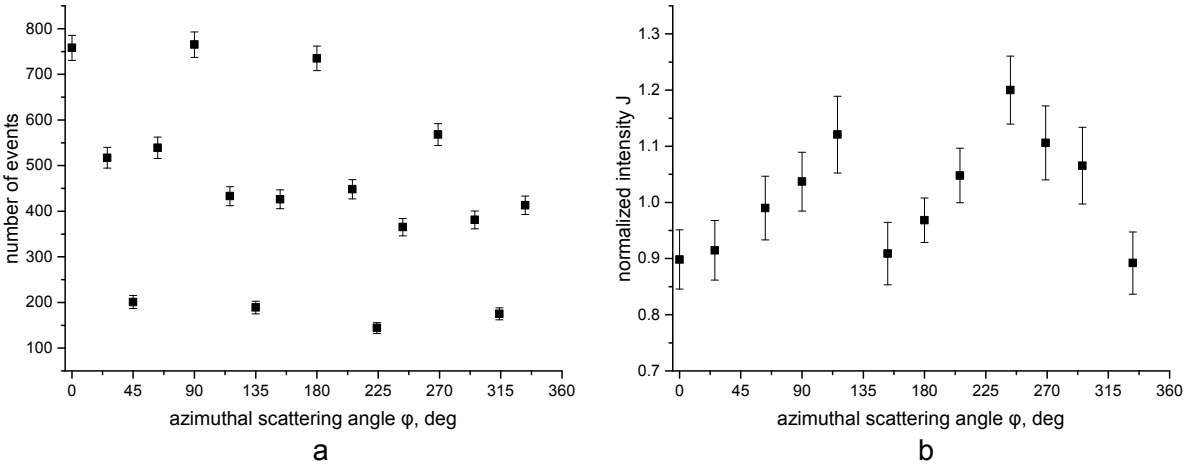

Figure 5.8: Measured scattered photon angular distributions. (a) Raw distribution. (b) Distribution after implementation of normalizations.

transversely polarized electrons. Withing these two measurements the azimuthal angular distributions of the scattered photons were obtained for two opposite electron spin orientations (collinear and anti-collinear to the electron beam in case of the longitudinal polarization and right and left to the electron beam in case of the transversal). The

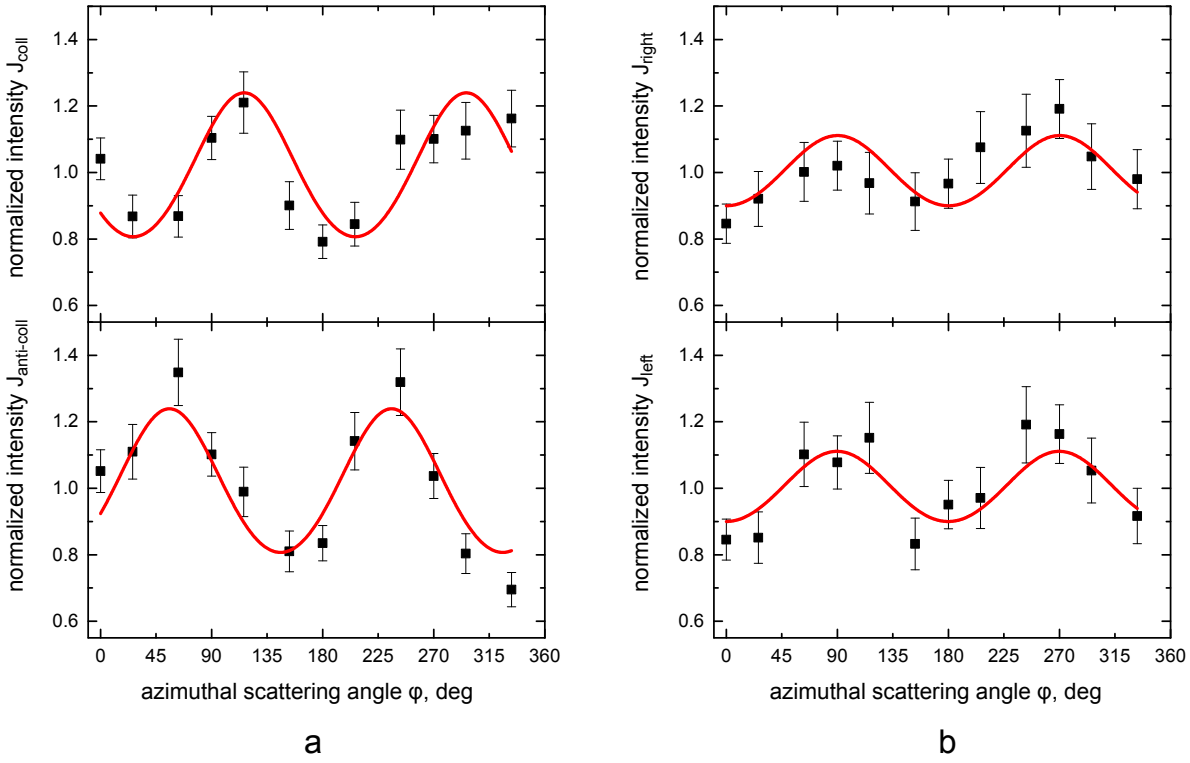

Figure 5.9: Normalized scattered photon angular distributions for the longitudinal (a) and transversal (b) electron beam polarizations.

mirror symmetry with respect to the plane, defined by the incoming electron and the emitted x ray propagation directions, requires that these two scattering distributions must have equal modulations and be tilted by the same angles χ into the opposite directions [20, 132] with respect to the reaction plane. Thus, to extract χ we fitted both of these distributions simultaneously using the formula, derived from Eq. 2.6:

$$F(\varphi, \chi, M) = \frac{1 - M\cos 2(\varphi \pm \chi + 90^\circ)}{1 - M\cos 2(\varphi \pm \chi)}, \tag{5.2}$$

while treating the modulation M and the phase χ as free parameters. Here $+\chi$ or $-\chi$ were used for the opposite spin orientations. The fitting curves for both longitudinal and transversal electron polarizations are presented in Fig. 5.9. The modulation M is proportional to the degree of linear polarization. Since within this experiment the degree of polarization does not reveal interesting physics, it was not analyzed.

Chapter 6

Results and discussion

For both transversal and longitudinal polarizations of the electron beam we observed the rotation of the bremsstrahlung polarization plane with respect to the reaction plane. The tilt angle χ was extracted from the fitting 5.2 of the scattered photon angular distributions in three energy intervals at the tip of the spectrum: 1.6 MeV - 1.8 MeV, 1.8 MeV - 2 MeV and 2 MeV - 2.15 MeV. This allowed us to study the correlation between the bremsstrahlung linear polarization and the photon energy while keeping the good statistics in each interval. The extracted tilt angles of bremsstrahlung polarization are presented in Fig. 6.1.

The change of the bremsstrahlung linear polarization as a function of the electron spin orientation is described by a set of coefficients $P_{1,2}(x, y, z)$. Where P_1 and P_2 are the first and second Stokes parameters and (x, y, z) are the components of the spin-polarization vector. These coefficients can be written in terminology of Tseng and Pratt as: $C_{03} = P_1(0, 0, 0)$, $C_{31} = P_2(0, 0, 1)$ and $C_{11} = -P_2(1, 0, 0)$ (see Table 3.1 in Section 3.1.4). Here the z axis coincides with the electron beam propagation direction and (x, z) is the reaction plane. The polarization tilt angles χ_z and χ_x of bremsstrahlung produced by the longitudinally and transversely polarized electron beams respectively

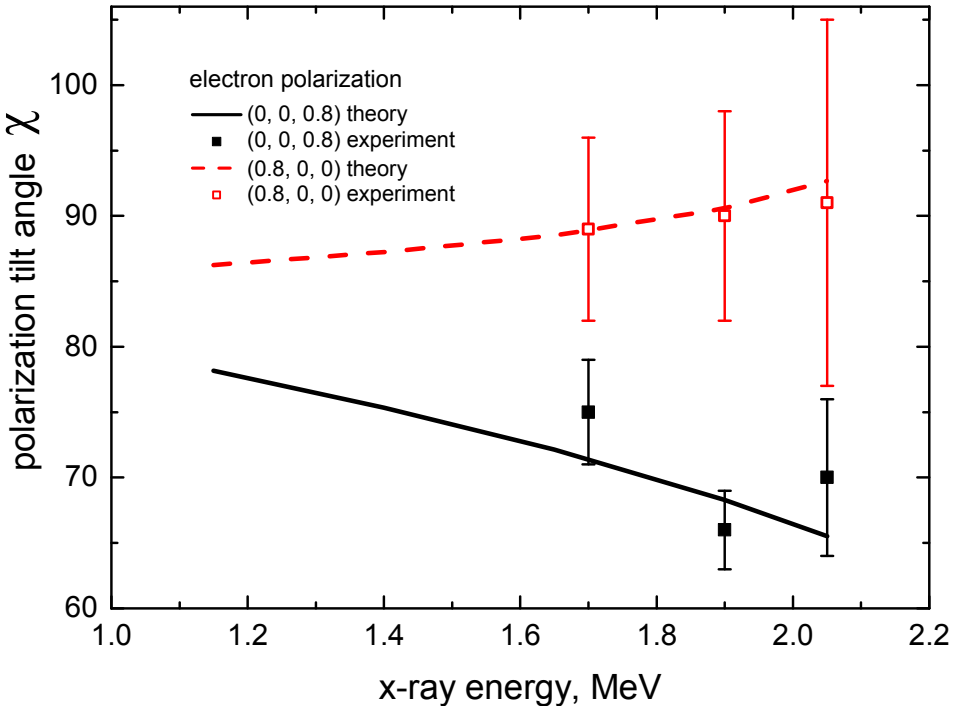

Figure 6.1: Tilt angles of bremsstrahlung linear polarization for the longitudinally and transversely polarized electron beam. Dashed and solid curves represent the fully relativistic theoretical calculations recently performed by V. Yerokhin [24, 133].

can be expressed as [57]:

$$\tan 2\chi_z = S\frac{P_2(0,0,1)}{P_1(0,0,0)}, \quad \tan 2\chi_x = S\frac{P_2(0,0,1)}{P_1(0,0,0)} \tag{6.1}$$

The observed rotation of the bremsstrahlung linear polarization indicates the significant role of electron spin in the dynamics of Coulomb scattering. We explain the correlation between the electron spin and the linear polarization of the emitted photon in terms of the classical electrodynamics. Although the description of bremsstrahlung in the MeV region must take quantum mechanics into account, calculations within the classical approximation help revealing the underlying physics of this phenomenon. Moreover, it gives the correct order of magnitude of the polarization tilt angle [57, 134].

Generally a non-relativistic electron is traveling in a central Coulomb potential along

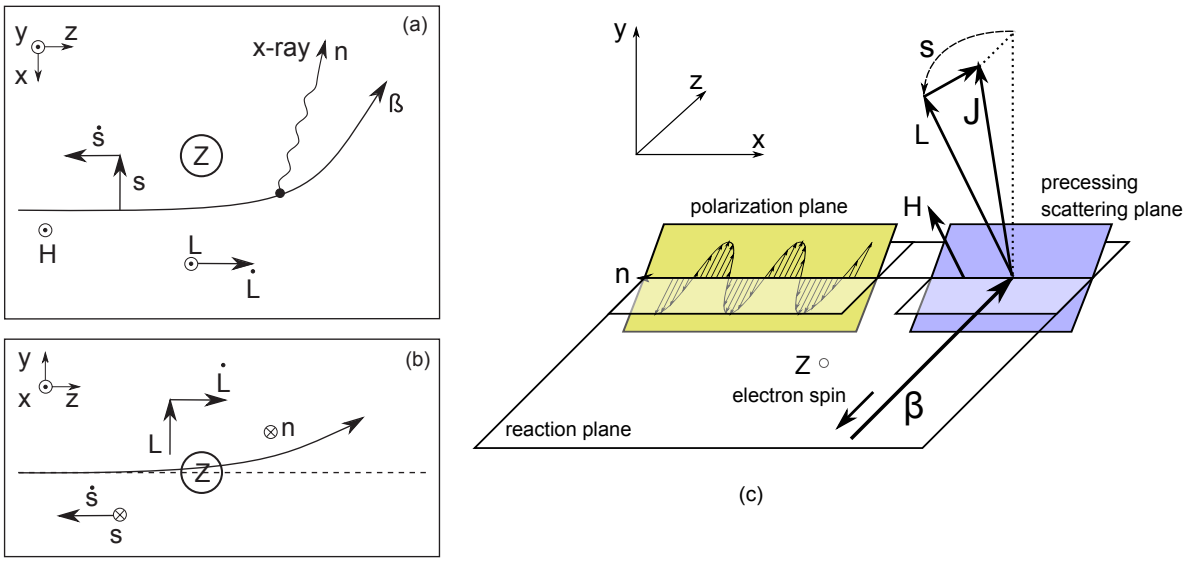

Figure 6.2: Classical explanation of the tilt of the electron scattering plane in projections along the Y (a) and X (b) axes. The magnetic field H is induced by the moving nucleus. The direction of the spin precession in this field and the induced orbital momentum precession is denoted by $\dot{S}$ and $\dot{L}$ respectively.

the curve, defined by its conserved orbital angular momentum $\boldsymbol{L} = \boldsymbol{r} \times \boldsymbol{\beta}$. At relativistic energies the influence of a spin becomes clearly pronounced. In the electron's rest frame the upcoming target nucleus induces the magnetic field. The spin of the electron precesses in this field [135]. In a uniform magnetic field approximation the spin rotation can be described by the Thomas-Bargmann-Michel-Telegdi equation [136]:

$$\dot{\boldsymbol{S}} = \boldsymbol{S} \times [\boldsymbol{E} \times \boldsymbol{\beta}] \frac{e}{mc} \left(g - 2 + \frac{1}{\gamma + 1} \right), \tag{6.2}$$

where $\boldsymbol{E}$ is the Coulomb field of the nucleus, $\boldsymbol{\beta} = v_e/c$ is the electron velocity, $g = 2.00116$ is the electron gyromagnetic ratio. Since the total angular momentum $\boldsymbol{J} = \boldsymbol{S} + \boldsymbol{L}$ has to be conserved, the orbital momentum precesses together with the spin $\dot{\boldsymbol{L}} = -\dot{\boldsymbol{S}}$. This causes the tilt of the electron scattering plane, and therefore, electron trajectory becomes three-dimensional [137, 138]. Figure 6.2 illustrates the geometry of the process.

The closer is electron trajectory to the nucleus, the stronger is the precession of the spin. Therefore, the intensity of the spin rotation is also dependent on the scattering angle. The electron scattering can be expressed via the Lorentz force [57]:

$$\dot{\boldsymbol{\beta}} = \boldsymbol{\beta} \times [\boldsymbol{E} \times \boldsymbol{\beta}] \frac{e}{mc} \frac{\gamma}{\gamma^2 - 1}. \tag{6.3}$$

Introducing the rotation speed of the electron spin $\boldsymbol{\Omega_s}$ and electron momentum $\boldsymbol{\Omega_\beta}$, equations 6.2 and 6.3 can be expressed as $\dot{\boldsymbol{S}} = \boldsymbol{S} \times \boldsymbol{\Omega_s}$ and $\dot{\boldsymbol{\beta}} = \boldsymbol{\beta} \times \boldsymbol{\Omega_\beta}$. Dividing Eq. 6.2 on Eq. 6.3 we get:

$$\boldsymbol{\Omega_s} = \frac{\Big((g-2)(\gamma+1)+1\Big)(\gamma-1)}{\gamma} \boldsymbol{\Omega_\beta}. \tag{6.4}$$

For the electron energy of 2.15 MeV ($\gamma = 5.2$) we obtain $\boldsymbol{\Omega_s} = 0.82\boldsymbol{\Omega_\beta}$. Since the photon emission is peaked along the instantaneous electron direction, we assume that the electron scattering angle matches the angle between the photon momentum and the electron beam. Therefore the detection angle of 90° corresponds to the spin tilt of 75°. We see that the classical model predicts the correct order of magnitude of the tilt angle of the bremsstrahlung linear polarization.

Within the classical approximation we interpret our measurement as an observation the electron trajectory in Coulomb scattering being not confined to a single plane. The trajectory is strongly affected by the spin-orbit interaction. This effect cannot be observed in a typical scattering experiment. Bremsstrahlung linear polarization is therefore a unique tool for probing the electron dynamics during the Coulomb scattering [9, 20, 57].

The difference between the tilt angles of bremsstrahlung polarization produced by longitudinally and transversely polarized electrons can be understood in a following way. In case of the transversal spin orientation the direction of the orbital momentum precession $\dot{\boldsymbol{L}}$ is perpendicular to the photon emission direction $\boldsymbol{n}$ (see Fig. 6.3a) and the tilt of the scattering plane directly corresponds to the tilt of the measured

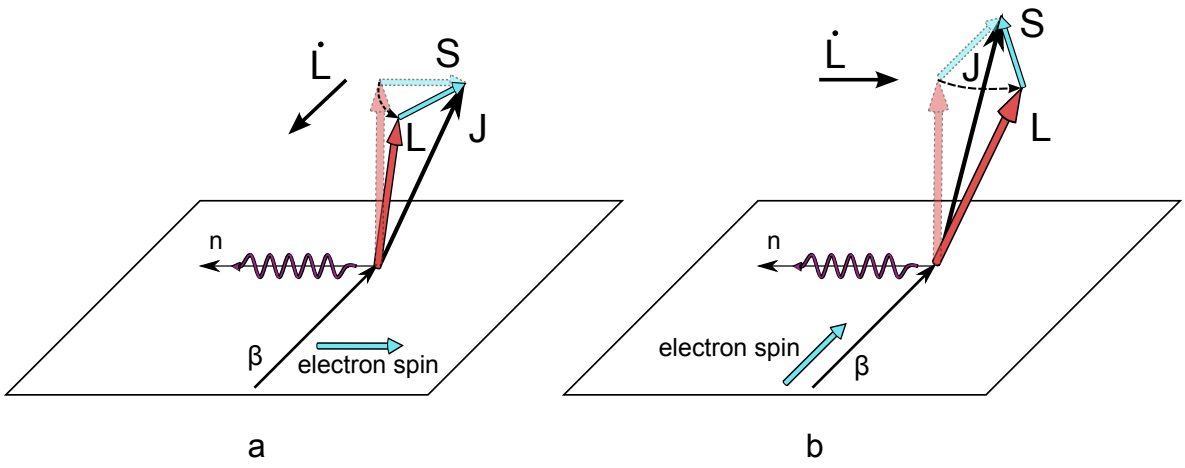

Figure 6.3: Precession of the orbital angular momentum $\boldsymbol{L}$ in the case of transversal (a) and longitudinal (b) electron spin orientation.

bremsstrahlung polarization. In case of the longitudinally polarized electron beam, however, $\dot{\boldsymbol{L}}$ is parallel to $\boldsymbol{n}$ (see Fig. 6.3b) and thus the rotation of the orbital momentum has a much smaller effect on the bremsstrahlung linear polarization. This explains why the measured tilt angle is smaller in the case of the longitudinal electron beam polarization.

The observed correlation between the bremsstrahlung linear polarization and electron spin orientation is dramatically enhanced as compared to the previous studies performed at 100 keV [57]. In particular the tilt angle of photon polarization produced by longitudinally polarized electrons increases from 2.1° to 70° (see Fig. 6.1). However at higher electron energies this effect is predicted to decrease [22, 23]. Therefore our experiment indicates an important benchmark for bremsstrahlung theories at the electron energies corresponding to the maximum of the polarization correlation [139]. Furthermore, it was predicted that, similar to Coulomb scattering, bremsstrahlung should become sensitive to the finite size of the nucleus as well as to its spin [140, 141]. Also in this energy range quantum electrodynamics (QED) should induce radiative corrections to the angular distribution of the emitted x rays at the level of a few percent [142, 143].

Therefore bremsstrahlung polarization may be sensitive to the QED corrections too. So far these effects were not included into calculations of bremsstrahlung from polarized electrons. The experimental precision approaches the level where such effects may become distinguishable.

Chapter 7

Summary and Outlook

In this work linear polarization of bremsstrahlung x rays produced in the collisions of polarized electrons with gold atoms at the energy of 2.15 MeV has been studied. Our measurement provides one of the most detailed probes of the electron spin dynamics in a strong Coulomb field. The experiment was performed at the Mainzer Microtron MAMI in the Institut für Kernphysik of Johannes Gutenberg-Universität Mainz, Germany. The scheme of the experiment is presented in Fig. 7.1a. Bremsstrahlung photons emitted at $90^\circ \pm 5^\circ$ with respect to the electron beam propagation direction were registered by a planar position sensitive high-purity germanium detector. The front side of the germanium crystal had a 5×5 square pixel segmentation. The measurement was performed for the electron spin orientations collinear and anti-collinear to the electron beam propagation direction (longitudinal beam polarization) and collinear and anti-collinear to x axis (transversal beam polarization). The bremsstrahlung linear polarization was studied by means of Compton polarimetry.

Compton-scattered x rays and the recoiled electrons were detected in time-coincidences in separate detector pixels. This allowed to sample the azimuthal angular distribution of the scattered x rays. However, strong angular dependence of bremsstrahlung emission resulted in a non-uniform detector illumination, which together with detector's square geometry significantly distorted the measured angular distributions. A number

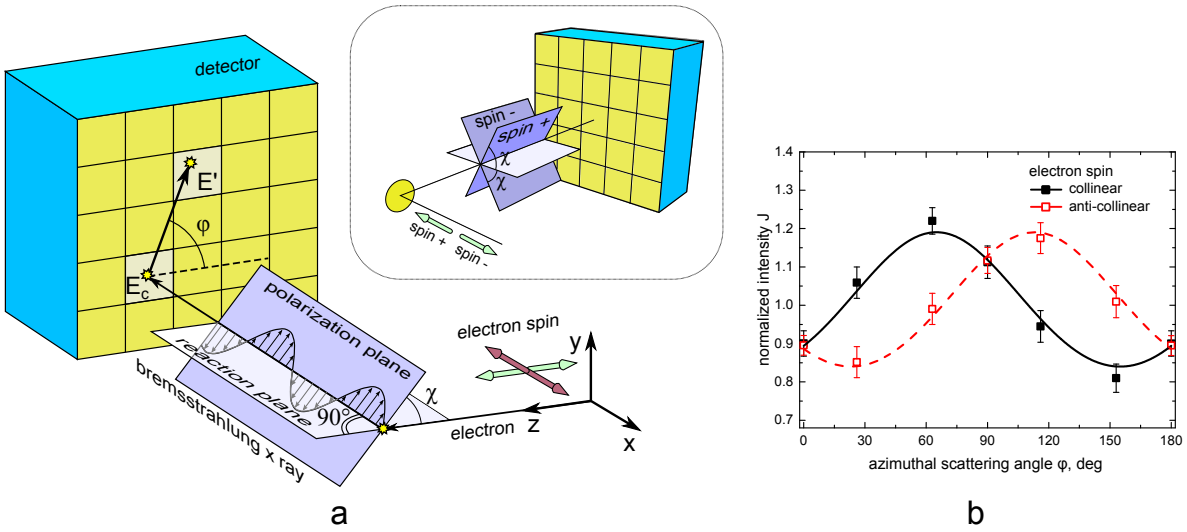

Figure 7.1: (a) Scheme of the setup for the bremsstrahlung polarization measurement. The inset shows the rotation of the polarization plane as the function of the initial electron spin orientation. (b) Typical normalized angular distributions of scattered bremsstrahlung photons produced by electrons with the opposite spin orientation. The phase shift between two curves indicates the rotation of the bremsstrahlung polarization plane.

of normalizations were applied in order to compensate for these effects and interpret the experimental data. This allowed for an extraction of bremsstrahlung polarization angle χ with the precision of around 10%. The errors are mainly caused by the statistical uncertainty. Fig. 7.1b shows the normalized angular distributions of the scattered photons produced by electrons with the spin orientation collinear and anti-collinear to the electron beam propagation direction.

The experiment demonstrates a dominant role of the electron spin in the dynamics of electron motion in the Coulomb field of a nucleus and in the process of atomic-field bremsstrahlung. Depending on the spin orientation the polarization plane of emitted x rays rotated with respect to the reaction plane (xz plane in Fig. 7.1a) by as much as 70° in case of the longitudinally polarized electrons and 85° in case of the transversal beam polarization. This is a dramatically enhanced effect as compared to the previous studies performed at 100 keV [20, 21, 57], where the observed rotation of the polarization plane

was of the order of several degrees.

We explain the observed phenomena in terms of a simplified classical model, which indicates that at relativistic energies under the influence of a spin-orbit interaction, the electron trajectory during Coulomb scattering on a nucleus is not confined to a single plane. This effect is present at close distance to the nucleus where the Coulomb force is extremely strong. It is not observable in a typical scattering experiment which controls only the incoming and scattered electron propagation direction

The obtained results agree well with fully relativistic calculations based on the partial-wave representation of the Dirac wave functions in an external atomic field [24]. However, further increase of the collision energy makes this theoretical approach extremely resource-consuming. At ultra relativistic energies, typically higher than 5 MeV, bremsstrahlung could so far only be described within the Sommerfeld-Maue approximation [141]. Thus, our measurement represents an important benchmark for the bremsstrahlung theory in the energy range where obtaining reliable predictions is difficult.

Bremsstrahlung at the short-wavelength limit can be considered as a time reversal of photoeffect [5, 6]. Therefore our measurement can be interpreted as a time-reverse production of longitudinally and transversely polarized electrons by illuminating the neutral atoms by linearly polarized photons [144]. This phenomenon has never been experimentally observed.

More accurate studies of bremsstrahlung polarization correlations at relativistic energies can reveal the presence of QED effects [143]. Finite size of a nucleus can also influence the bremsstrahlung polarization [141]. Existing calculations of bremsstrahlung produced by polarized electrons do not take these effects into account.

Of particular interest is the measurement of the correlation between bremsstrahlung linear polarization and the initial electron spin orientation in a coincident experiment, i.e., when the emitted photon is detected in coincidence with the deflected electron.

Strong dependence of bremsstrahlung polarization on the scattered electron direction was predicted in a number of theoretical investigations [68, 69]. Such experiment would indicate an important step towards the kinematically complete measurement of electron-nucleus bremsstrahlung where the polarization properties of all the involved particles are controlled.

Detailed understanding of bremsstrahlung polarization correlations is required for the application of the newly proposed method of a circular γ-ray polarimetry [145]. It is based on the transfer of the photon spin to the recoiled electron in Compton scattering. Measurement of the angular distribution and polarization of bremsstrahlung, produced by these electrons gives access to the circular polarization of the incoming photons. Such a technique combines well with the concept of Compton telescope. Thus, it should allow circular polarization measurements of multiple sources. No such technique is currently available. Its implementation should for the first time allow circular polarimetry of cosmic γ rays.

The sensitivity of bremsstrahlung to longitudinal and transversal electron spin components can be applied for the electron beam polarimetry. The principal setup should consist of a photon polarimeter placed within the (x, z) plane as in Fig. 7.1 and additionally two detectors placed within the (y, z) plane to register the up-down x-ray emission asymmetry [146]. The vertical component y of electron spin can be potentially obtained from the degree of bremsstrahlung polarization. Alternatively it can be accessed from the left-right photon emission asymmetry measured by the additional pair of detectors placed within the (x, z) plane. This method allows for simultaneous measurement of all three components of electron beam polarization, which is an advantage as compared to the Mott scattering technique. It should be suitable for the energy range from around 50 keV up to several tens of MeV.

Measurement of the bremsstrahlung linear polarization as described in this work, can be also utilized for plasma diagnostics. Hot anisotropic plasmas, present in such

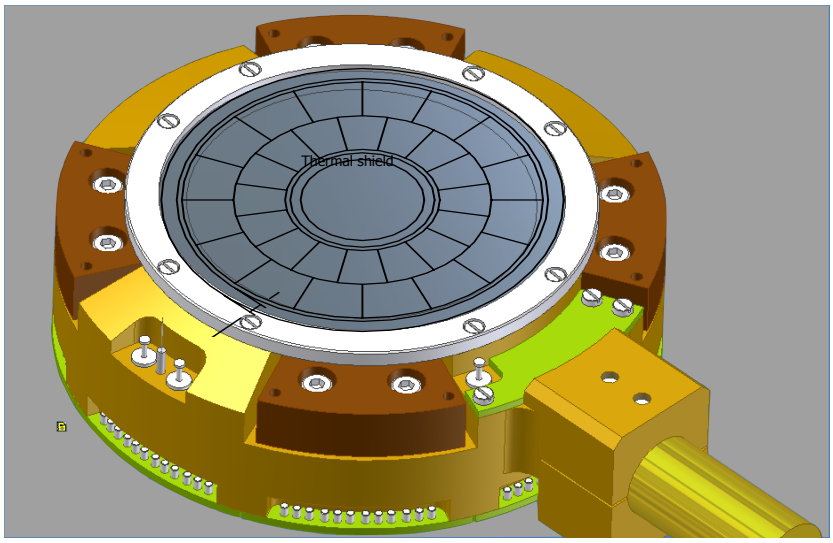

Figure 7.2: Scheme of a novel HPGe Compton polarimeter which is being developed by our group.

astrophysical objects as black hole jets and solar flares, are the intense sources of x-ray radiation. General approach to the anisotropy diagnostics is based on measuring the x-ray lines linear polarization. However, application of this method is often complicated due to the low intensity and generally small degree of polarization of x-ray lines. The more intense continuum part of the spectrum is dominated by bremsstrahlung from hot electrons. Recent measurement of polarization of x rays emitted by a 15 keV ECR plasma revealed the non-uniform distribution of hot electrons in the plasma volume [147].

Currently a new positional sensitive HPGe detector is being developed by our group. The round segmentation symmetry eliminates the geometrical effects that modulate the angular distribution of scattered photons, which makes the detector's geometry perfectly suitable for x-ray polarimetry. The principal scheme of segmentation is shown in Fig. 7.2.

Acknowledgements

Probably there are no such words that can fully express the depth of my gratitude to my parents - Igor Oleksandrovich and Juliia Jurjevna Kovtun. Your incredible optimism and unbreakable spirit were inspiring and encouraging me through all these years.

I would like to say my very special thanks to my supervisor Priv.-Doz. Dr. Stanislav Tashenov. I think you are the brightest example of what a modern scientist should be. Without your comprehensive knowledge in countless branches of physics, IT, engineering... (honestly, this list does not have an end), unbelievable patience and sense of purpose it would be absolutely impossible for me to complete this work.

I thank my colleagues and office mates Chintan Shah, Dr. Pedro Amaro, Holger Jörg, Allison Pinto, Dr. Oliver Matula, Dr. Thorsten Jahrsetz, Dr. Anton Artemyev, Dr. Vanessa Simon, and Dr. Zhimin Hu for a wonderful friendly atmosphere present in all our discussions of physics, music, languages and tons of other topics. I deeply appreciate the help of the collaborators from Mainz Microtron: Dr. Valery Tioukine whose ingenious engineering solutions and ideas contributed a lot to the successful finish of our experiment; Prof. Dr. Kurt Aulenbacher whose valuable discussions helped me significantly during my time in Mainz. I would like to express my sincere thanks to Priv.-Doz. Dr. Andrey Surzhykov who shared his bottomless knowledge in theoretical atomic physics with me and also helped to improve this manuscript. I must also acknowledge Prof. Dr. Siegbert Hagmann and Dr. Pierre-Michel Hillenbrand for giving me a unique opportunity to take part in the experiment in GSI and broaden my

knowledge in atomic physics.

I cannot imagine my time in Heidelberg without my dear friends: Vlad Hahn, Dr. Armen Hayrapetyan, Alina Schwetz, Artem and Anna Blednovy, Deniz Ergene, Deniz Senyilmaz, Karolina Ceglowska, Henrik Nersisyan, Vahe Gevorgyan, Kamola Gulamova, Rike Beyersdorf and especially Oleksandra Opochenska. I sincerely hope we will stay close no matter what happens in the future.

Great appreciation goes to my good old friends in Ukraine: Rodion Skidanov, Nikita and Natasha Kuklich, Zhora Vdovichenko, Anton Samohin, Natasha Schtyk, Kirill Bystrov, Nick Budov, Anton Vyugin, Yulia Kislaya, Lelya Devyatko, Robert Markov. Unfortunately I had to escape from you and we cannot spend so much time together like we used to, but for real friends distance does not exist and you will always stay in my heart.

I gratefully acknowledge Prof. Vadim Pavlovich Matsokin and Dr. Inessa Vasilyevna Vorobyova for being my first physics supervisors.

I would like to thank my family: Yuriy, Tatiana, Ilya for supporting and believing in me through my entire life.

Last but not least I would like to express my sincere gratitude to the members of my examination committee: Priv.-Doz. Dr. Stanislav Tashenov, Prof. Dr. Norbert Herrmann, Priv.-Doz. Dr. Zoltan Harman, and Prof. Dr. Lothar Schad for showing interest in my research.

I sincerely apologize if I accidentally did not mention somebody. I wish I could list much more names but unfortunately I have to stop here as I am running out of free space.

Sincerely yours,
Oleksiy Kovtun

Bibliography

[1] A. Sommerfeld, Annalen der Physik **403**, 257 (1931).

[2] F. Lei, A. Dean, and G. Hills, Space Science Reviews **82**, 309 (1997).

[3] H. R. Griem, A. C. Kolb, and W. R. Faust, Phys. Rev. Lett. **2**, 281 (1959).

[4] U. Zastrau, C. Fortmann, R. R. Fäustlin, L. F. Cao, T. Döppner, *et al.*, Phys. Rev. E **78**, 066406 (2008).

[5] K. W. McVoy and U. Fano, Phys. Rev. **116**, 1168 (1959).

[6] R. H. Pratt, Phys. Rev. **120**, 1717 (1960).

[7] I. J. Feng, I. B. Goldberg, Y. S. Kim, and R. H. Pratt, Phys. Rev. A **28**, 609 (1983).

[8] M. Nofal, S. Hagmann, T. Stöhlker, D. H. Jakubassa-Amundsen, C. Kozhuharov, *et al.*, Phys. Rev. Lett. **99**, 163201 (2007).

[9] J. Jackson, Classical Electrodynamics, 2nd ed, Wiley, New York (1975).

[10] K. W. McVoy, Phys. Rev. **106**, 828 (1957).

[11] E. Haug, Phys. Rev. **188**, 63 (1969).

[12] N. Sherman, Phys. Rev. **103**, 1601 (1956).

[13] J. W. Motz, H. Olsen, and H. W. Koch, Rev. Mod. Phys. **36**, 881 (1964).

[14] E. S. Sobolak and P. Stehle, Phys. Rev. **129**, 403 (1963).

[15] E. Haug, Zeitschrift für Physik D Atoms, Molecules and Clusters **37**, 9 (1996).

[16] K. Güthner, Zeitschrift für Physik **182**, 278 (1965).

[17] H. Schaefer, W. von Drachenfels, and W. Paul, Zeitschrift für Physik A Atoms and Nuclei **305**, 213 (1982).

[18] H. K. Tseng and R. H. Pratt, Phys. Rev. A **7**, 1502 (1973).

[19] H. K. Tseng, R. H. Pratt, and C. M. Lee, Phys. Rev. A **19**, 187 (1979).

[20] S. Tashenov, T. Bäck, R. Barday, B. Cederwall, J. Enders, *et al.*, Phys. Rev. Lett. **107**, 173201 (2011).

[21] R. Märtin, G. Weber, R. Barday, Y. Fritzsche, U. Spillmann, *et al.*, Phys. Rev. Lett. **108**, 264801 (2012).

[22] D. H. Jakubassa-Amundsen, Phys. Rev. A **82**, 042714 (2010).

[23] D. Jakubassa-Amundsen and A. Surzhykov, The European Physical Journal D **62**, 177 (2011).

[24] V. A. Yerokhin and A. Surzhykov, Phys. Rev. A **82**, 062702 (2010).

[25] E. Silver, M. Weisskopf, H. Kestenbaum, K. Long, R. Novick, and R. Wolff, Astrophysical Journal, Part 1 **232** (1979).

[26] P. Kaaret, R. Novick, C. Martin, P. Shaw, J. Fleischman, *et al.*, IAU Colloquim No 123: "Observatories in Earth Orbit and Beyond" (1990).

[27] S. Tashenov, A. Khaplanov, B. Cederwall, and K.-U. Schässburger, Nuclear Instruments and Methods in Physics Research Section A **600**, 599 (2009).

[28] R. Bellazzini, L. Baldini, A. Brez, E. Costa, L. Latronico, *et al.*, Nuclear Instruments and Methods in Physics Research Section A **510**, 176 (2003).

[29] XCOM: Photon Cross Sections Database (2007), `http://physics.nist.gov/PhysRefData/Xcom/Text/XCOM.html`.

[30] K. Siegbahn, Alpha-, Beta- and Gamma-Ray Spectroscopy, Vol.2, Amsterdam (1968).

[31] O. Klein and Y. Nishina, Zeitschrift für Physik **52**, 853 (1929).

[32] J. Jauch and F. Rohrlich, The Theory of Photons and Electrons, 1st ed, Springler-Verlag, New York , 233 (1975).

[33] NIST Tables of X-Ray Mass Attenuation Coefficients and Mass Energy-Absorption Coefficients (2004), `http://www.nist.gov/pml/data/xraycoef/`.

[34] L. Mihailescu, W. Gast, R. Lieder, H. Brands, and H. Jäger, Nuclear Instruments and Methods in Physics Research Section A **447**, 350 (2000).

[35] B. Bruyneel, P. Reiter, and G. Pascovici, Nuclear Instruments and Methods in Physics Research Section A **569**, 764 (2006).

[36] W. R. Leo, Techniques for Nuclear and Particle Physics Experiments, Springer, Heidelberg (1994).

[37] H. Spieler, Semiconductor Detector Systems, Oxford University Press (2005).

[38] J. Eberth and J. Simpson, Progress in Particle and Nuclear Physics **60**, 283 (2008).

[39] G. Knoll, Radiation Detection and Measurement, Wiley, New York (2002).

[40] T. Stöhlker, D. Banas, H. Beyer, A. Gumberidze, C. Kozhuharov, *et al.*, Nuclear Instruments and Methods in Physics Research Section B **205**, 210 (2003).

[41] P. Reiter, J. Eberth, H. Faust, S. Franchoo, J. Gerl, *et al.*, Nuclear Physics A **701**, 209 (2002).

[42] C. E. Svensson, P. Amaudruz, C. Andreoiu, A. Andreyev, R. A. E. Austin, *et al.*, Journal of Physics G: Nuclear and Particle Physics **31**, S1663 (2005).

[43] J. Simpson, Journal of Physics G: Nuclear and Particle Physics **31**, S1801 (2005).

[44] HISPEC/DESPEC executive summary (2006), `http://personal.ph.surrey.ac.uk/~phs1zp/exec.summary.jan06.doc`.

[45] C. Beausang, Nuclear Instruments and Methods in Physics Research Section B **204**, 666 (2003).

[46] K. Vetter, A. Kuhn, M. Deleplanque, I. Lee, F. Stephens, *et al.*, Nuclear Instruments and Methods in Physics Research Section A **452**, 223 (2000).

[47] A. Khaplanov, Doctoral Thesis, Royal Institute of Technology, Stockholm, Sweden (2010).

[48] A. Khaplanov, J. Pettersson, and B. Cederwall, Nuclear Instruments and Methods in Physics Research Section A **580**, 1075 (2007).

[49] S. Boggs, W. Coburn, D. Smith, J. Bowen, P. Jean, *et al.*, New Astronomy Reviews **48**, 251 (2004).

[50] T. Niedermayr, K. Vetter, L. Mihailescu, G. Schmid, D. Beckedahl, J. Blair, and J. Kammeraad, Nuclear Instruments and Methods in Physics Research Section A **553**, 501 (2005).

[51] F. Metzger and M. Deutsch, Phys. Rev. **78**, 551 (1950).

[52] A. Ferguson, Nuclear Instruments and Methods **162**, 565 (1979).

[53] S. Ohya, H. Miura, K. Nishimura, N. Mutsuro, and T. Aoki, Nuclear Instruments and Methods in Physics Research Section A **276**, 223 (1989).

[54] P. Kirkpatrick and L. Wiedmann, Phys. Rev. **67**, 321 (1945).

[55] H. W. Koch and J. W. Motz, Rev. Mod. Phys. **31**, 920 (1959).

[56] H. K. Tseng and R. H. Pratt, Phys. Rev. Lett. **33**, 516 (1974).

[57] S. Tashenov, T. Bäck, R. Barday, B. Cederwall, J. Enders, *et al.*, Phys. Rev. A **87**, 022707 (2013).

[58] W. Nakel and E. Haug, World Scientific Lecture Notes in Physics (2004).

[59] H. A. Bethe and W. Heitler, Proc. Roy. Soc. **A126**, 83 (1934).

[60] G. Elwert, Ann. Physik (Leipzig) **34**, 178 (1939).

[61] H. Olsen, Phys. Rev. **99**, 1335 (1955).

[62] L. I. Schiff, Phys. Rev. **83**, 252 (1951).

[63] H. Olsen, L. C. Maximon, and H. Wergeland, Phys. Rev. **106**, 27 (1957).

[64] H. K. Tseng and R. H. Pratt, Phys. Rev. A **3**, 100 (1971).

[65] C. M. Lee, R. H. Pratt, and H. K. Tseng, Phys. Rev. A **16**, 2169 (1977).

[66] C. D. Shaffer, X.-M. Tong, and R. H. Pratt, Phys. Rev. A **53**, 4158 (1996).

[67] S. Keller and R. Dreizler, J. Phys. B: At. Mol. Opt. Phys. **30**, 3257 (1997).

[68] H. K. Tseng, J. Phys. B: At. Mol. Opt. Phys. **35**, 1129 (2002).

[69] R. A. Müller, V. A. Yerokhin, and A. Surzhykov, Phys. Rev. A **90**, 032707 (2014).

[70] R. L. Gluckstern and M. H. Hull, Phys. Rev. **90**, 1030 (1953).

[71] K. W. McVoy, Phys. Rev. **111**, 1333 (1958).

[72] C. Fronsdal and H. Überall, Phys. Rev. **111**, 580 (1958).

[73] M. Goldhaber, L. Grodzins, and A. W. Sunyar, "Evidence for circular polarization of bremsstrahlung produced by beta rays," (1957).

[74] A. Claesson, Arkiv Fysik **12**, 569 (1957).

[75] V. Balashov, A. Grum-Grzhimailo, and N. Kabachnik, Polarization and Correlation Phenomena in Atomic Collisions, Kluwer Academic/Plenum, New York (2000).

[76] W. H. McMaster, American Journal of Physics **22**, 351 (1954).

[77] R. H. Pratt and I. J. Feng, in Atomic Inner-Shell Physics, ed. by B. Crasemann, Plenum Publishing Corporation , 533 (1985).

[78] J. Eichler and T. Stöhlker, Physics Reports **439**, 1 (2007).

[79] J. W. Motz and R. C. Placious, Phys. Rev. **109**, 235 (1958).

[80] J. W. Motz, Phys. Rev. **100**, 1560 (1955).

[81] A. Aehlig and M. Scheer, Zeitschrift für Physik **250**, 235 (1972).

[82] H.-H. Behncke and W. Nakel, Physics Letters A **47**, 149 (1974).

[83] E. Smick and P. Kirkpatrick, Phys. Rev. **60**, 220 (1941).

[84] H. Amrehn and H. Kulenkampff, Zeitschrift für Physik **140**, 452 (1955).

[85] C. D. Curtis, Phys. Rev. **89**, 123 (1953).

[86] P. C. Fisher, Phys. Rev. **92**, 420 (1953).

[87] N. Starfelt and H. W. Koch, Phys. Rev. **102**, 1598 (1956).

[88] W. Nakel, Physics Letters **22**, 614 (1966).

[89] W. Nakel, Physics Letters A **25**, 569 (1967).

[90] G. Elwert and E. Haug, Phys. Rev. **183**, 90 (1969).

[91] A. Aehlig, Zeitschrift für Physik A Atoms and Nuclei **294**, 291 (1980).

[92] E. Mergl and W. Nakel, Zeitschrift für Physik D Atoms, Molecules and Clusters **17**, 271 (1990).

[93] E. Mergl, H.-T. Prinz, C. D. Schröter, and W. Nakel, Phys. Rev. Lett. **69**, 901 (1992).

[94] J. W. Motz, Phys. Rev. **104**, 557 (1956).

[95] J. W. Motz and R. C. Placious, Phys. Rev. **112**, 1039 (1958).

[96] R. W. Kuckuck and P. J. Ebert, Phys. Rev. A **7**, 456 (1973).

[97] W. Lichtenberg, A. Przybylski, and M. Scheer, Phys. Rev. A **11**, 480 (1975).

[98] H. H. Behncke and W. Nakel, Phys. Rev. A **17**, 1679 (1978).

[99] W. Bleier and W. Nakel, Phys. Rev. A **30**, 607 (1984).

[100] E. Haug, Radiation Physics and Chemistry **75**, 1330 (2006).

[101] F. Tessier and I. Kawrakow, Nuclear Instruments and Methods in Physics Research Section B **266**, 625 (2008).

[102] E. Hauga, The European Physical Journal D **49**, 193 (2008).

[103] W. Nakel and E. Pankau, Physics Letters A **38**, 307 (1972).

[104] W. Nakel and E. Pankau, Zeitschrift für Physik A Atoms and Nuclei **274**, 319 (1975).

[105] M. Komma and W. Nakel, Journal of Physics B: Atomic and Molecular Physics **15**, 1433 (1982).

[106] D. Mack and H. Mitter, Physics Letters A **44**, 71 (1973).

[107] M. Y. Amusia, Phys. Rep. **162** (1987).

[108] V. M. Buimistrov and L. I. Trakhtenberg, Zh. Eksp. Teor. Fiz. **69** (1975), [Sov. Phys. JETP **42**, 54 (1975)].

[109] M. Y. Amusia, A. S. Baltenkov, and V. B. Gilerson, Sov. Phys. - Tech. Phys. Lett. **3** (1977).

[110] A. V. Korol, A. G. Lyalin, and A. V. Solovy'ov, Journal of Physics B: Atomic, Molecular and Optical Physics **30**, L115 (1997).

[111] A. Korol, A. Lyalin, O. Obolenskii, and A. Solov'yov, Journal of Experimental and Theoretical Physics **87**, 251 (1998).

[112] A. V. Korol, O. I. Obolensky, A. V. Solov'yov, and I. A. Solovjev, Journal of Physics B: Atomic, Molecular and Optical Physics **34**, 1589 (2001).

[113] A. V. Korol, A. G. Lyalin, O. I. Obolensky, A. V. Solovyov, and I. A. Solovjev, Zh. Eksp. Teor. Fiz. **121** (2002), [JETP **94** (2002) 704].

[114] M. Y. Amusia, N. B. Avdonina, L. V. Chernysheva, and M. Y. Kuchiev, J. Phys. B: At. Mol. Opt. Phys. **18** (1985).

[115] A. V. Korol, A. G. Lyalin, A. Solovyov, N. Avdonina, and R. Pratt, J. Phys. B: At. Mol. Phys. **35** (2002).

[116] A. Korol and A. Solovyov, Radiation Physics and Chemistry **75**, 1266 (2006).

[117] S. Portillo and C. A. Quarles, Phys. Rev. Lett. **91**, 173201 (2003).

[118] E. T. Verkhovtseva, E. V. Gnatchenko, and P. S. Pogrebnjak, Journal of Physics B: Atomic and Molecular Physics **16**, L613 (1983).

[119] K. Ozawa, J. H. Chang, Y. Yamamoto, S. Morita, and K. Ishii, Phys. Rev. A **33**, 3018 (1986).

[120] O. Obolensky and R. Pratt, Radiation Physics and Chemistry **75**, 2239 (2006).

[121] R. Haygood, S. Williams, and C. Quarles, Radiation Physics and Chemistry **75**, 1688 (2006).

[122] H. Herminghaus, A. Feder, K. Kaiser, W. Manz, and H. Schmitt, Nuclear Instruments and Methods **138**, 1 (1976).

[123] K.-H. Kaiser, K. Aulenbacher, O. Chubarov, M. Dehn, H. Euteneuer, *et al.*, Nuclear Instruments and Methods in Physics Research Section A **593**, 159 (2008).

[124] R. Heine, K. Aulenbacher, O. Chubarov, M. Dehn, H. Euteneuer, *et al.*, Proc. of the iPAC 2010, Kyoto, Japan (2010).

[125] V. Tioukine, K. Aulenbacher, and E. Riehn, Review of Scientific Instruments **82**, 033303 (2011).

[126] T. Maruyama, D.-A. Luh, A. Brachmann, J. E. Clendenin, E. L. Garwin, *et al.*, Applied Physics Letters **85**, 2640 (2004).

[127] K. Aulenbacher, C. Nachtigall, H. Andresen, J. Bermuth, T. Dombo, *et al.*, Nuclear Instruments and Methods in Physics Research Section A **391**, 498 (1997).

[128] V. Tioukine and K. Aulenbacher, Nuclear Instruments and Methods in Physics Research Section A **568**, 537 (2006).

[129] J. Kessler, Polarized Electrons Series on Atoms and Plasmas, 2nd ed, Springer, New York (1985).

[130] The Imaging Compton Telescope (COMPTEL) http://heasarc.gsfc.nasa.gov/docs/cgro/comptel/.

[131] ICRU Report No. 37 (unpublished) (1984).

[132] S. Tashenov, T. Stöhlker, D. Banaś, K. Beckert, P. Beller, *et al.*, Phys. Rev. Lett. **97**, 223202 (2006).

[133] V. Yerokhin, private communication .

[134] L. Kim and R. H. Pratt, Phys. Rev. A **36**, 45 (1987).

[135] L. H. Thomas, Nature (London) **117**, 514 (1926).

[136] V. Bargmann, L. Michel, and V. L. Telegdi, Phys. Rev. Lett. **2**, 435 (1959).

[137] F. Berezin and M. Marinov, Annals of Physics **104**, 336 (1977).

[138] V. Kozoriz and Y. Musin, Theoretical and Mathematical Physics **123**, 478 (2000).

[139] O. Kovtun, V. Tioukine, A. Surzhykov, V. Yerokhin, B. Cederwall, A. Khaplanov, and S. Tashenov, submitted, under review .

[140] U. Fano, K. W. McVoy, and J. R. Albers, Phys. Rev. **116**, 1159 (1959).

[141] D. Jakubassa-Amundsen, Physics Letters A **377**, 1885 (2013).

[142] J. McEnnan and M. Gavrila, Phys. Rev. A **15**, 1557 (1977).

[143] D. J. Botto and M. Gavrila, Phys. Rev. A **26**, 237 (1982).

[144] R. H. Pratt, R. D. Levee, R. L. Pexton, and W. Aron, Phys. Rev. **134**, A916 (1964).

[145] S. Tashenov, Nuclear Instruments and Methods in Physics Research Section A **640**, 164 (2011).

[146] S. Tashenov, T. Bäck, R. Barday, B. Cederwall, J. Enders, *et al.*, Journal of Physics: Conference Series **488**, 012057 (2014).

[147] S. Tashenov, C. Szabo-Foerster, P. Indelicato, and A. Gumberidze, to be published .